Engineering Design of a Modular Hydrogen Production System

MSc Thesis

Camiel Grevet

Engineering Design of a Modular Hydrogen Production System

by

Camiel Grevet

To obtain the degree of Master of Science at the Delft University of Technology;
to be defended publicly on August 28, 2023 at 14:00.

Student number:	4277910		
Project duration:	November, 2022 - August, 2023		
Thesis committee:	Prof. Dr. T. J. H. Vlugt	TU Delft	chair
	Dr. O. Moultos	TU Delft	supervisor
	Dr. A. Rahbari	XINTC	supervisor
	Prof. Dr. K. Hooman	TU Delft	member

This thesis is confidential and cannot be made public until August 28, 2025.

Abstract

The utilization of water electrolysis for hydrogen production is expected to increase significantly in the upcoming decades. Modular system design offers great advantages for emerging markets, whilst providing the necessary flexibility in capacity that intermittent renewable energy sources require. Literature research reveals little information regarding modular water electrolysis systems. However, their availability on the consumer market proves that there is demand for such systems. To facilitate the emerging hydrogen market, a modular engineering design approach is used to develop a containerized alkaline water electrolysis system. This containerized system achieves a high degree of modularity by utilizing multiple modular sections. Each section functions as a stand-alone hydrogen production station, containing all necessary components required for safe hydrogen production. These components include heat exchangers, gas-liquid separators, modular alkaline electrolyzers, and a novel component called flow panels. In conjunction with the Dutch company XINTC, the design of the modular sections and their components is presented. Significant capital expenditure reduction is achieved by operating at atmospheric pressure, allowing for cost-efficient material selection and their corresponding manufacturing methods; both of which are discussed. Thermal, hydrodynamic, and particle dynamic models from literature are presented and evaluated. The proposed hydrogen separator is expected to achieve a separation efficiency of over 99.8%. A thermal system analysis concludes that the system is capable of operating at maximum capacity for ambient temperatures of up to 35 °C. Additionally, a hydrodynamic system analysis shows that the pressure drop inside the system is dominated by that of the heat exchanger, and is in conformity with the Pressure Equipment Directive.

Preface

Dedicated to all who have provided support during my academic endevours, for there are too many names to name. May God bless you all. Here is to patience, persistence, and resolve.

– *Camiel Grevet,*
Delft, August 2023

Contents

Chapter 1

Introduction

The growth in both world population and global economic development brings with it an ever-increasing demand for energy. For the past centuries, the utilization of fossil fuels has allowed humankind to leapfrog their technological advancements. It is no coincidence that the steam turbine is the face of the industrial revolution. The on-demand availability of fossil fuels, along with their high energy density, make them unrivalled within the transport and thermal energy sectors. However, the adverse effects of CO_2 associated with fossil fuel consumption became apparent in the twentieth century, with the term global warming used as early as 1975 [1]. Decreasing CO_2 emissions whilst still meeting the ever-growing energy demand of the modern world has proven to be challenging, especially in growing economies [2]. The Net Zero Emissions (NZE) by 2050 Scenario [3], is a normative scenario proposed by the International Energy Agency (IEA). The NZE scenario presents a pathway to achieve net zero CO_2 emissions in the global energy sector by 2050 [3]. It is consistent with limiting the global temperature rise to well below 2 °C above pre-industrial levels, as agreed upon by 196 Parties in the Paris Agreement [4].

Renewable energy sources (RES) play a key role in reaching NZE, and as such have gained popularity over the past decades [3, 5]. Per definition, renewable energy (RE) is energy that can be collected from renewable resources, e.g., solar irradiation and tidal variation. The impact of RES on the largest energy sectors is relatively small, even though an increase in globally installed RE capacity is recorded almost yearly [5]. The most prominent RES are hydropower, solar photovoltaic (PV), and wind power. There seem to be two key properties hindering the widespread use of these RES. First, their intermittent nature results in an unbalance between the supply and demand of energy [6]. Second, RES that facilitate the production of electricity are at a disadvantage in fossil fuel dominated sectors. In order to overcome this unbalance, a power storage medium is deemed necessary. A suitable energy carrier for power facilitated by RES is hydrogen [7, 3, 5, 8, 9]. Hydrogen production through water electrolysis is capable of utilizing intermittent RES that facilitate the production of electricity [10]. In this process, electricity is used to split water into hydrogen and oxygen molecules. Hydrogen as an energy carrier can be used as a fuel directly, or converted back to electricity through fuel cell technology. It is also possible to synthesize light hydrocarbons such as methanol or ethanol with hydrogen and CO or CO_2, which in turn can be used as fuel [11]. It is anticipated that the hydrogen market will increase significantly from now until 2050 [7]. In order to facilitate the emerging hydrogen market, a modular engineering design approach to hydrogen production is presented in this report.

1.1 Renewable Energy

In 2021, more than 314 GW of RE power capacity was installed globally [5]. RES that facilitate the production of electricity totalled a global capacity of more than 3100 GW in 2021 [5]. Hydropower contributed the most, followed by solar PV, and wind power. Figure 1.1 shows the distribution of

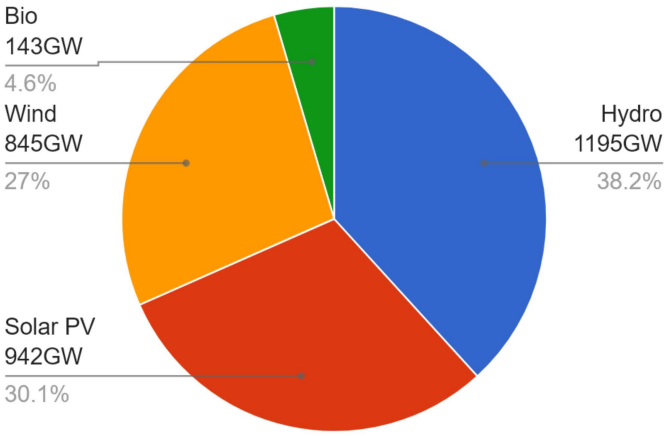

Figure 1.1: Breakdown of major global power facilitating RES in 2021. Based on data from the IEA [5].

power generation of the major RES deployed globally. Geothermal energy seems to be the only significant RES that facilitates the production of heat. 508 GW of geothermal energy was used for direct heating in 2021 [5]. RES have much lower energy flux (energy output per ground area), when compared to fossil fuels [12]. This means that RE production is less economically feasible than fossil-fueled power plants when ground area is contested, such as in large cities.

1.1.1 The Global Energy Market

The global energy market consists of three main sectors, namely the power, transport and thermal sector. A breakdown of global energy consumption per sector in 2019, along with the contribution of RE in each sector is shown in Figure 1.2. It is observed that the global energy market has been largely built around the utilization of fossil fuels.

1.1.1.1 The Power Sector

It is unsurprising that the power sector has the largest RE contribution, as the vast majority of RE facilitates the production of electricity. Power consumption in the industry represents around 10% of global energy consumption, and more than half of total global power consumption [5]. Fossil fuels are prominent in this sector because industrial productions prefer a steady source of power that is flexible enough to adjust production rates according to demand. It is possible to power a large grid system by incorporating a diverse RES network [13]. However, a large buffer in the form of energy storage media would be necessary to bridge the gap between supply and demand [6].

1.1.1.2 The Transport Sector

The transport sector has the lowest share of renewable energy. Almost three-quarters of the energy demand of this sector comes from road transport [5]. Although the sales of electric vehicles (EV) are on the rise, internal combustion engines dominate the market [5]. High energy density energy sources that are quickly rechargeable are preferred in this sector. Fossil fuels offer both these qualities, as do biofuels. Because of this, biofuels are the most prominent RES used in the transport sector [5]. An energy carrier that mimics fossil fuels seems necessary for RES to penetrate the transport sector. Improving battery technology could contribute to faster charging and an increased range of EVs. Hydrogen can (partially) fuel internal combustion engines, as well as power EVs through fuel cell technology [9, 14].

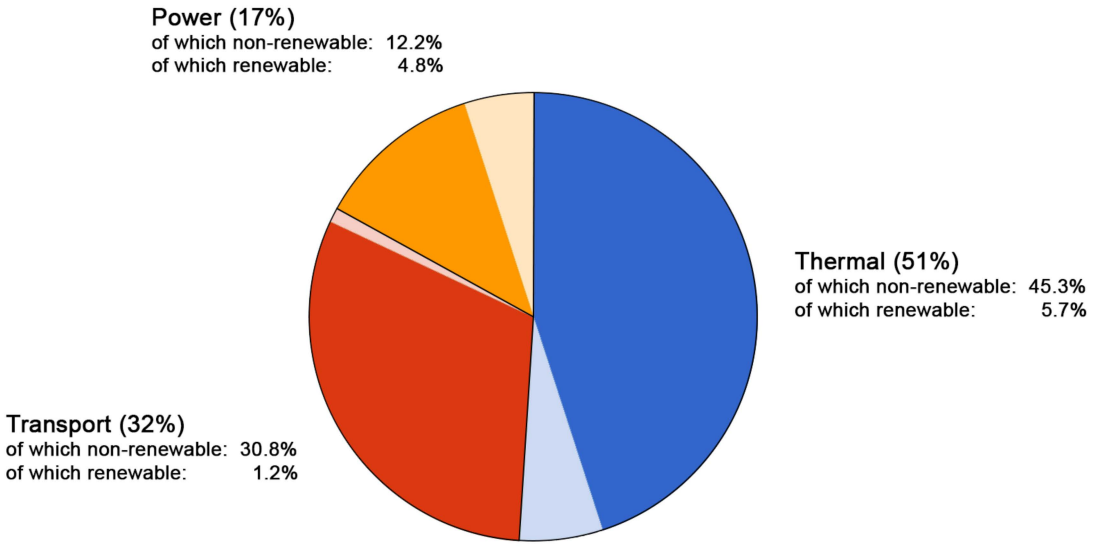

Figure 1.2: Graph of global energy consumption in 2021, and their respective fractions of renewable sourced energy shown in lighter colours. Based on data from the IEA [5].

1.1.1.3 The Thermal Sector

Unlike power, heat is rarely sold off-site [15]. This offers a challenge to local heat generation through renewable means (e.g., geothermal or solar-thermal energy). Geophysical constraints, intermittent availability, and technical limitations of thermal storage techniques are withholding the integration of renewable heat sources in the thermal sector [16]. The dispersed nature of the heat market further complicates the problem. Over a third of global thermal energy consumption is from industry [5]. Through proper planning, it is possible to locate industrial plants near renewable heat sources, but this provides little to no advantage to existing industrial plants. The use of electric storage heaters seems promising in allowing electricity facilitated by RES to penetrate the thermal sector [17]. Hydrogen as a fuel seems promising for the thermal sector, as it is a transportable energy carrier.

1.1.2 The Storage Problem

A lack of energy storage media is perceived in each of the aforementioned energy sectors. The majority of energy storage devices currently deployed are either pumped hydro storage (93%), or electrochemical storage devices (5%) [18]. Both of these methods are centralized power-to-power methods that do not allow for efficient energy transportation off-site. Electrochemical energy storage seems to yield the highest technological potential when both supply and demand of RES are centralized [18]. A centralized power-to-power storage method seems unsuitable when geophysical constraints are hindering the utilization of renewable electricity in the global energy sector. The dispersed nature of the global energy market implies that transportability is a crucial property of an energy storage medium, as it facilitates the decentralized utilization of RES. Although there does not seem to be a single most efficient energy storage technology for all purposes, hydrogen can be used for both centralized and decentralized energy storage for all global energy sectors.

1.2 Hydrogen

Hydrogen is the lightest element known. Hydrogen gas (H_2) is not commonly present in nature and is thus not considered an energy source, but an energy carrier. It is colourless, odourless, tasteless, and highly flammable. As a fuel, hydrogen offers high energy content per mass unit, but its energy density is relatively low [19]. Global hydrogen consumption totalled 90 Mt in 2020, of which 80% was produced from fossil fuels. The majority of the remaining hydrogen production is residual gas produced in refineries and the petrochemical industry. In 2020, less than 1% of hydrogen was produced through water electrolysis [7].

1.2.1 The Role of Hydrogen in the Net Zero Emissions Scenario

In the NZE scenario, hydrogen and hydrogen-based fuels account for 10% of total global energy consumption by 2050 [3]. Clean hydrogen production can help to avoid up to 60 Gt of CO_2 emission between 2021 and 2050. This results in a contribution of 6%, to the total emission reductions by mitigation measures presented in the NZE scenario [7]. To achieve this, the IEA suggests that the annual global hydrogen production should reach 200 Mt by 2030, of which 70% is to be produced through low-carbon technologies (water electrolysis or fossil fuels with carbon capture, utilization, and storage (CCUS)) [7]. It goes on to suggest that by 2050, hydrogen should be almost exclusively produced through low-carbon technologies, and reach a global annual production of over 500 Mt. An overview of the total necessary annual hydrogen production, and technologies used, can be seen in Figure 1.3. Compared to hydrogen production in 2020, the NZE scenario implies the following:

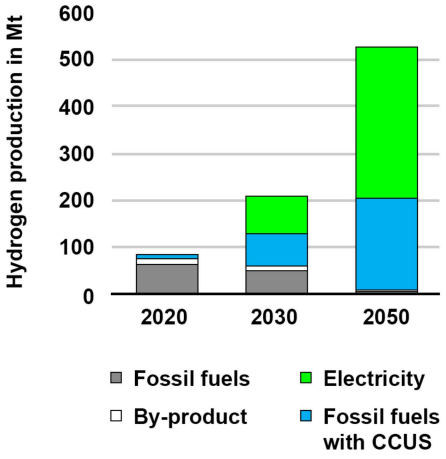

Figure 1.3: Annual hydrogen production capacity and methods based on the NZE scenario [7]

- hydrogen production capacity should increase over twofold by 2030 and over eightfold by 2050;
- installed water electrolysis capacity utilizing RE should increase three thousandfold by 2030, and twelve thousandfold by 2050; and
- captured CO_2 in hydrogen production through utilizing fossil fuels with CCUS should increase fivefold by 2030, and over thirteenfold by 2050 [3].

1.3 The XINTC System

XINTC [20] is a Dutch company that develops, produces, and markets modular alkaline electrolyzer systems. Their inspiration comes from a hydrogen production market gap in the NZE plans. This market gap is observed between the residential market, and the the steam methane reforming market (150 kW - 50 MW) [7]. In response, XINTC is developing a middle-range hydrogen production system. A containerized approach allows for plug-and-play, decentralized operation; making it ideal for direct coupling with RES, such as solar PV and wind power. Production capacity can range from very low up to the multi-megawatt scale, due to high system modularity. Capacity can be expanded through said modular approach, enabling the end user to evolve along with the RE market. The XINTC system operates at atmospheric pressure, resulting in significant capital expenditure reduction. This reduction has two main causes. First, safety requirements for hydrogen systems are more lenient at atmospheric pressure. Second, the strength requirements of materials

reduce significantly when compared to operations at higher pressures. Due to the corrosive nature of alkaline electrolyte, stainless steel is the industry standard for electrolyzer systems [21]. The absence of pressure-induced stresses allows for the usage of plastics. Plastics are a cheap manufacturing material that can offer great chemical resistance. They also enable manufacturing methods that are otherwise unavailable for conventional metallic electrolyzer systems [22].

The XINTC system consists of a service station and a production station. Figure 1.4 shows an illustration of the XINTC system. The service station is deployed in a 20 ft container and houses all necessary electronics for coupling, as well as the user interface. Power is transferred from the service station to the production station. The production station is housed in a 40 ft container and houses the electrolyte storage, a water purification system (reverse osmosis), and modular hydrogen production sections. Each section is again a modular system and contains all necessary components for stand-alone operation. Multiple sections are deployed per container, resulting in a high degree of modularity. An illustration of the modular section concept is shown in Figure 1.5. Each section has four major components. First, the alkaline electrolyzers that enable hydrogen production. Second, heat exchangers to counteract the heat generated by the electrolyzers during commission. Third, a novel component named a flow panel that accommodates the fluid flow of the system. Last, two gas-liquid separators to separate hydrogen and oxygen products from the electrolyte.

Figure 1.4: Concept of XINTC's containerized hydrogen production system. Service station displayed on the left-hand side; consisting of a 20 ft container that houses coupling electronics and the user interface. The production station is displayed on the right-hand side; consisting of a 40 ft container that houses a water purification system, and the hydrogen-producing modular section.

1.4 Research Objectives

This work focuses on the engineering design of the XINTC modular sections. The electrolyzer module and its properties lay at the core of the XINTC system design. For instance, system fluid flow rates, maximum service temperature, and heat exchanger requirements all stem from the properties of the electrolyzer modules. The section should be designed in a way that enables optimal utilization of the modules, whilst ensuring safe operations. At the time of writing, the electrolyzer modules have already been fully developed. The general design, sizing, material selection, heat transfer, and hydrodynamics of all other main system components are to be researched and evaluated. Afterwards, a system analysis is to be performed, ensuring that the section components function adequately in conjunction with one another. Several restrictions are introduced by the characteristics of the XINTC concept. First, the containerized system approach introduced spatial limitations that result in significant engineering challenges (e.g., limiting heat exchanger surface area). Second, the decentralized and plug-and-play nature of the system necessitates the system to be air-cooled. Third, the corrosive nature of the alkaline electrolyte inhibits the use of various materials and manufacturing methods (e.g., welding due to the risk of imperfections resulting in leakage). Finally, the use of plastic materials should be evaluated and applied whenever deemed fit. Plastics have a relatively low maximum service temperature, introducing an upper limit to

Figure 1.5: Illustration of the modular section in the XINTC system. Each section functions as a stand-alone unit, and allows for convenient system capacity alteration. Each section includes electrolyzer modules, heat exchangers, gas-liquid separators, and a flow panel.

the system [23]. As plastics typically provide less structural strength than metallic materials, pressure drop within the system should be analyzed and confirmed to not challenge the strength limitation of the system components. The system should operate at atmospheric pressure, and a maximum allowable overpressure of 500 mbar is considered, in accordance with the Pressure Equipment Directive (PED) [24].

1.5 Thesis Outline

To achieve the suggested research objectives, this work is divided into five parts. In Chapter 2, a literature review is conducted wherein the basic principle of water electrolysis and modular system design is presented, and the flow panel concept is investigated. In Chapter 3, the general design, sizing, material selection, heat transfer, and hydrodynamics of all major system components are presented. Whenever deemed necessary, analytical models are proposed, and their results are quantified. In Chapter 4, an evaluation of the performance of the section as a whole will be presented. Concluding remarks and recommendations regarding future work will be provided in Chapter 5. Additional information accumulated during the literature review is presented in the Appendix section of this work, since it is not deemed essential information for the reader. It is explicitly mentioned when an Appendix is consulted, and it should be reviewed by the reader at will. Information presented in the Appendices includes electrolyte properties in Appendix A, relations for heat convection in Appendix B, hydrodynamic relations in Appendix C, and plastics and their applicable manufacturing methods in Appendix D.

Chapter 2

Literature review

2.1 Water Electrolysis

Water electrolysis is the electrochemical process of separating water into hydrogen and oxygen. The device wherein electrolysis occurs is called an electrolyzer. Within electrolyzers, ions are conducted through the means of an alkaline or acidic electrolyte [19]. The overall reaction that takes place inside an electrolyzer is given by:

$$H_2O \rightarrow H_2 + \frac{1}{2}O_2 \tag{R2.1}$$

A brief summary of the thermodynamics surrounding electrolysis, and the properties of the most prominent electrolyzer technologies will be discussed in this section.

2.1.1 Thermodynamics

The energy required for electrolysis is determined by its change in enthalpy ΔH [25]. Part of ΔH is supplied by heat Q, whilst the other part is supplied by a DC current (change in Gibbs free energy ΔG):

$$\Delta H = \Delta G + Q \tag{2.1}$$

This implies that the electrical energy required for the reaction is less at higher operating temperatures. The theoretical minimum cell voltage at which electrolysis occurs is called the reversible cell voltage U_{rev}:

$$U_{\text{rev}} = \frac{\Delta G}{zF} \tag{2.2}$$

where $F = 96485$ C/mol is Faraday's constant, and z the number of electrons transferred per reaction ($z = 2$ for water electrolysis). In most commercial electrolyzers, the thermal portion of Equation 2.1 is provided by electricity ($Q = 0$) [25]. In which case, the theoretical minimum cell voltage is referred to as the thermo-neutral voltage U_{tn}:

$$U_{\text{tn}} = \frac{\Delta H}{zF} \tag{2.3}$$

High-temperature electrolyzers typically operate near U_{tn}, as heat generated by irreversibilities is equalized by heat consumption of the reaction. Low-temperature electrolyzers do not utilize generated heat, resulting in them operating above U_{tn}, and requiring external cooling [10]. The total cell voltage U_{cell}, can be expressed as the sum of: U_{rev}; overvoltages induced by ohmic resistance U_{ohm}; activation overvoltages due to electrode kinematics U_{act}; and concentration overvoltages due to mass transport limitations U_{con} [25]:

$$U_{\text{cell}} = U_{\text{rev}} + U_{\text{ohm}} + U_{\text{act}} + U_{\text{con}} \tag{2.4}$$

The voltaic efficiency is defined as the ratio between the reference voltage, and the applied cell voltage:

$$\eta_{\mathrm{U}} \equiv \frac{U_{\mathrm{ref}}}{U_{\mathrm{cell}}} \tag{2.5}$$

where the reference voltage U_{ref}, refers to U_{tn}, or U_{rev}, depending on the electrolyzer system. The faradaic efficiency η_{F}, or current efficiency, is expressed as the ratio between current loss I_{loss}, and total cell current I_{cell} [26]:

$$\eta_{\mathrm{F}} = 1 - \frac{I_{\mathrm{loss}}}{I_{\mathrm{cell}}} \tag{2.6}$$

Total cell efficiency is then defined as the product of the voltage, and current efficiencies [26]:

$$\eta_{\mathrm{tot}} = \eta_{\mathrm{U}} \cdot \eta_{\mathrm{F}} \tag{2.7}$$

The rate of hydrogen production $\dot{n}_{\mathrm{H_2}}$ [mol/s], is derived from Faraday's law of electrolysis:

$$\dot{n}_{\mathrm{H_2}}^{\mathrm{cell}} = \eta_{\mathrm{F}} \frac{I_{\mathrm{cell}}}{zF} \tag{2.8}$$

where n_{cell} is the number of cells in the electrolyzer stack, and $M_{\mathrm{H_2}}$ [mol/m^3] is the molarity of hydrogen. The cell current I_{cell} [A] can be determined through the $I - U$ curve of the electrolyzer system [10].

2.1.2 Alkaline Electrolyzers

The alkaline electrolyzer (AEL) gets its name from the usage of an alkaline solution as an electrolyte. AELs are the most common, mature, and economical electrolyzer technology [25]. AELs are applied in both small and large-scale hydrogen production [27, 28]. A schematic representation of an AEL cel can be seen in Figure 2.1. The alkaline electrolyte allows for the usage of low-cost materials for the electrodes; in contrast to acidic electrolytes. The anode and cathode are typically made from nickel and catalyst-coated steel, respectively [27]. The electrolyte is typically a KOH solution with a concentration in the range of 25-30% [10]. Gaseous product is removed from the half-cells through either forced, or natural circulation of the electrolyte. A solid porous membrane is present between the electrodes to reduce gas-crossover rate between the two half-cells. The partial reactions at the cathode and anode are given by:

$$\text{Cathode:} \quad 2\mathrm{H_2O} + 2\mathrm{e^-} \rightarrow \mathrm{H_2} + 2\mathrm{OH^-} \tag{R2.2}$$

$$\text{Anode:} \quad 2\mathrm{OH^-} \rightarrow \frac{1}{2}\mathrm{O_2} + \mathrm{H_2O} + 2\mathrm{e^-} \tag{R2.3}$$

Water is consumed at the cathode side, and produced at the anode side. To prevent a dilution, and concentration buildup it is crucial that recirculated electrolyte is mixed before reentering the electrolyzer. However, the recirculated electrolyte streams also carry dissolved gaseous products, leading to an increase in impurity [29].

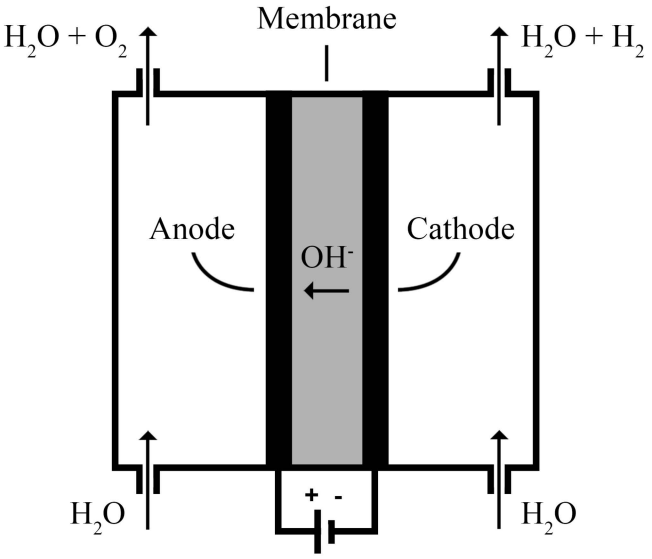

Figure 2.1: Schematic representation of an AEL cell. Aqueous KOH flows into the half-cells. Reaction (R2.2) takes place at the cathode, producing hydrogen gas and OH^-. OH^- formed at the cathode travels through the membrane to the anode. Reaction (R2.3) takes place at the anode, producing oxygen gas and liquid water. Hydrogen and oxygen produced leave their respective half-cells, along with the electrolyte circulation flow.

AELs have a lifetime of approximately 20-30 years [30]. Their specific energy demand ranges from 4.1-5.9 kWh/m^3 hydrogen produced, and higher heating value (HHV)efficiencies of 62-82% can be achieved [31, 30]. The purity of produced hydrogen and oxygen can reach 99.9% and 99.7%, respectively [32]. The typical operation of AELs is in the temperature and pressure range of 50-80 °C and 1-30 bar, respectively [30]. Higher temperature operation leads to more efficient hydrogen production. Higher pressure operation reduces energy demand in case of future compression [10, 27]. However, gas-crossover rate through the membrane increases with temperature and pressure and thus also impurities [29]. AELs operate at relatively low current densities (up to 0.4 A/cm^2), and system impurities increase as current density further decrease [30, 29].

2.1.3 Proton Exchange Membrane Electrolyzers

The proton exchange membrane electrolyzer (PEMEL) gets its name from the solid polymer membrane electrolyte. This, typically Nafion®, membrane is thin (<0.2 mm), and strongly acidic [25]. The two electrodes are directly mounted to the acidic membrane, necessitating the use of chemically resistant electrode materials. Typically, noble metals such as platinum and iridium are utilized [27]. The cost and availability of these rare earth metals form the largest drawback of PEMELs. Figure 2.2 shows a basic illustration of a PEMEL cell. The following reaction takes place in its half-cells:

$$\text{Cathode:} \quad 2H^+ + 2e^- \rightarrow H_2 \tag{R2.4}$$

$$\text{Anode:} \quad H_2O \rightarrow \frac{1}{2}O_2 + 2H^+ + 2e^- \tag{R2.5}$$

Water is consumed at the anode to form oxygen gas and H^+-ions, also referred to as protons. These protons travel through the membrane towards the cathode, where they form hydrogen gas. The membrane pores are significantly smaller than that of an AEL, since the membrane only has

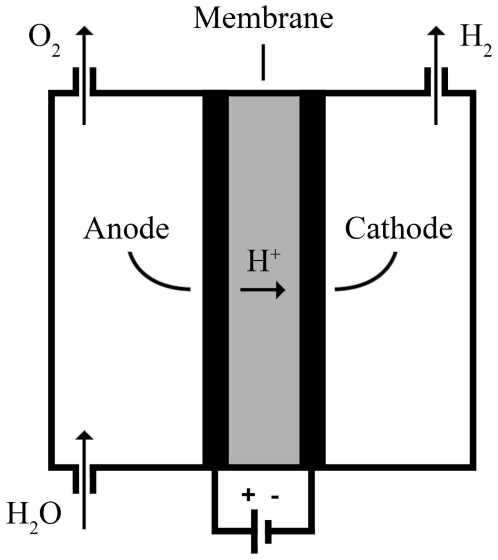

Figure 2.2: Schematic representation of a PEMEL cell. Water is consumed at the anode to form oxygen gas and protons. The protons formed travel through the acidic membrane towards the cathode, where they interact with one another to form hydrogen gas.

to facilitate the transport of protons. This results in a reduction in gas crossover [25]. The purity of produced hydrogen is typically above 99.99 % [33]. PEMELs are suitable for operation at very low current densities. As a result of their thin membrane, PEMELs react quickly to fluctuations in power supply, making them suitable to work in conjunction with intermittent RE sources [19]. PEMELs have a lifetime of approximately 10-20 years. They can operate at relatively high current densities (up to 2.0 A/cm^2). Specific energy demand is in the range of 4.2-5.6 kWh/m^3 hydrogen produced, and HHV efficiencies are in the range of 67-82% [31, 30].

2.1.4 Solid Oxide Electrolyzers

A solid oxide electrolyzer (SOEL), or steam electrolyzer, utilizes a solid electrolyte. SOELs operate at high temperatures (up to 1000 °C), allowing them to reach HHV efficiencies of over 100% [27, 34]. SOELs show great potential to be utilized in conjunction with stable heat-producing RES, such as geothermal energy [35]. However, stresses caused by changes in temperature induce micro-cracks in the solid oxide electrolyte, which significantly reduces their lifetime [27, 30]. Therefore, SOEL seems currently unsuitable to be coupled with intermittent RES that facilitate electricity.

2.2 Flow Panels

The concept of flow panels is unmentioned in literature, and is considered a novel concept. Redox flow battery technology utilizes a similar concept, where it is referred to as flow frames [36, 37]. In redox flow batteries, flow channels are embedded in the structural frame of cells. These flow frames distribute electrolyte flow across a large number of channels with very little leakage [37, 38]. This concept is very similar to the one suggested in this work. The literature on the application of flow frames in redox batteries is considered merely a proof of concept, due to the difference in size and application.

2.3 Modular System Design

Modular system design (MSD) is a design principle that revolves around increasing manageability by dividing a complex system into smaller segments called modules. Modular systems show high interdependence within modules, and independence across modules [39]. The degree to which modules interact more among themselves than with other modules is referred to as modularity [40]. Figure 2.3 shows examples of types of modular systems. Modularity can be beneficial in every step of a project's timeline. During development, MSD can reduce the timespan of the design process by allowing modules to be worked on in parallel [39, 41]. MSD also allows integration of off-the-shelf components (e.g., heat exchangers, separation units, etc.), to reduce engineering costs [42]. During fabrication, the ability to mass produce standardized units provides a scale advantage [43, 39]. In-house assembly of the modules leads to faster deployment and greater quality control [42]. Fabrication and assembly of modules can be performed during the permitting and site development phase of a project, resulting in time savings [42]. When modules are ready for deployment, time-to-market is shortened by enabling (partial) operation with a single module [44, 42]. During commission, modular systems provide flexibility in the form of convenient system expansion, adaptability to market conditions, easy reconfiguration, and simplified maintenance [41, 45, 44, 46]. The independence across modules also decreases system sensitivity to perturbations, as they are less likely to spread across modules [40]. However, MSD can lead to increased costs when poorly optimized and/or utilized [47]. In the case of the latter, the flexibility of modular systems can mitigate this problem through customization of modules [39].r

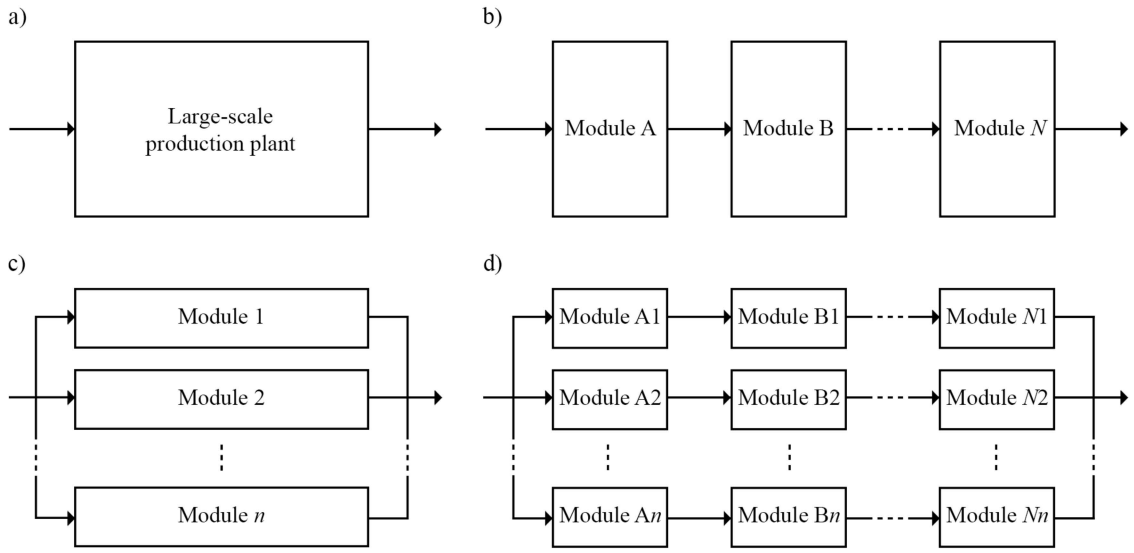

Figure 2.3: Basic representation of: a) standard large-scale system; b) modular system with N modules in series; c) modular system with n modules in parallel; d) combined series and parallel modular system.

2.3.1 The Economy of Numbers

Economy of numbers (EoN) is a concept revolving around increasing production capacity by increasing the number of production units. In the case of a modular system, increasing the number of modules to increase production capacity follows this concept. EoN allows for flexibility in production capacity by adding or removing deployed modules. It also reduces both initial capital investment and development time when compared to the concept of economy of scale (EoS) [44].

The EoS relies on increasing production capacities in order to decrease relative production costs. In 2011, Lier et al. [44] compared the net present value of a large-scale chemical production plant to a similar modular system comprising of 10 modules. They argue that modular systems start to generate revenue sooner, allowing them to reach a financial break-even point faster than large-scale facilities. In the case of linear market growth, a large-scale production system outperforms a modular system after a certain timespan, making them more profitable in the long term. In the case study presented by Lier et al. [44], this timespan was approximately 10 years. In the case of exponential or realistic market growth, the flexibility of modular systems allows them to consistently outperform large-scale production plants. They go on to suggest that increasing the total number of modules further reduces the time to break-even. Costs of modular systems are expected to decrease as more units are produced, as a result of an increase in development, manufacturing and installation experience [43, 44]. The lower initial investment costs, along with a shorter time to break-even, reduces the risks for investors [44]. This makes utilizing the EoN concept a suitable option for novel products, especially when entering emerging markets [42].

2.3.2 Modular Hydrogen Production Systems

Some examples of modular hydrogen production systems can be found in literature. Many studies explore the utilization of small modular nuclear reactors to facilitate hydrogen production [48, 49, 50, 51]. Martinez et al. [52], present a novel modular natural gas-assisted SOEL system. Huang et al. [11], address a modular design for a methanol synthesis system, utilizing RE. The most concrete examples of modular hydrogen production in literature come from photochemical hydrogen production units, which are inherently modular [53, 19].

Although not present in literature, modular hydrogen producing electrolyzer systems are commercially available. This implies that there is a market for modular hydrogen systems. Some examples are systems manufactured by Sunfire, Nel ASA and Enapter. Table 2.1 shows an overview of commercial modular hydrogen production systems. The Sunfire HyLink HL200 [54], is a container-based SOEL system, offering up to 5 modules with a maximum capacity of 150 kW each. For large-scale production, Sunfire offers the HyLink SOEC system [55], with modular units up to a maximum capacity of 2.7 MW. Sunfire also offers an AEL system [56], which contains modules with a capacity of 10 MW each. Nel ASA [28], produces both PEMEL and AEL systems. Their modular PEMEL systems range from 5 kW to 25 MW, and their modular AEL system ranges from 570 kW to 14 MW. Enapter [57], utilizes small electrolyzers in a highly modular system. Each EL 4.0 AEM electrolyzer module offers 3 kW of electrolyzer power. Up to 70 modules can be installed in a 20-foot container system, allowing for a scalable operation of up to 210 kW.

System	Manufacturer	Type	Max. capacity	Module capacity	Nr. of modules
HyLink HL200 [54]	Sunfire	SOEL	750 kW	150 kW	5
HyLink SOEC [55]	Sunfire	SOEL	2.7 MW	N/A	N/A
HyLink Alkaline [56]	Sunfire	AEL	N/A	10 MW	N/A
M-series [28]	Nel ASA	PEMEL	25 MW	N/A	N/A
A-series [28]	Nel ASA	AEL	14 MW	570 kW	25
EL 4.0 [57]	Enapter	AEL	210 kW	3 kW	70

Table 2.1: Overview of commercial modular hydrogen production systems and their properties.

Chapter 3

Main System Components

In this chapter, the general design, sizing, material selection, heat transfer, and hydrodynamics of the major system components are covered. Most of the aforementioned topics are relevant to all major system components. A schematic representation of the section and the alignment of each component is shown in Figure 3.1. Due to the highly flammable nature of hydrogen, a large ventilation airflow is introduced within each section to ensure safe system operations. A qualitative evaluation of the ventilation airflow will be presented in section 4.1. Since the airflow crosses all major components, the convective heat transfer that follows is investigated for each respective component. The methods applied to calculate the convective heat transfer within the system, are described in Appendix B. The container is considered a closed system, and therefore internal radiative heat transfer phenomena will not be considered.

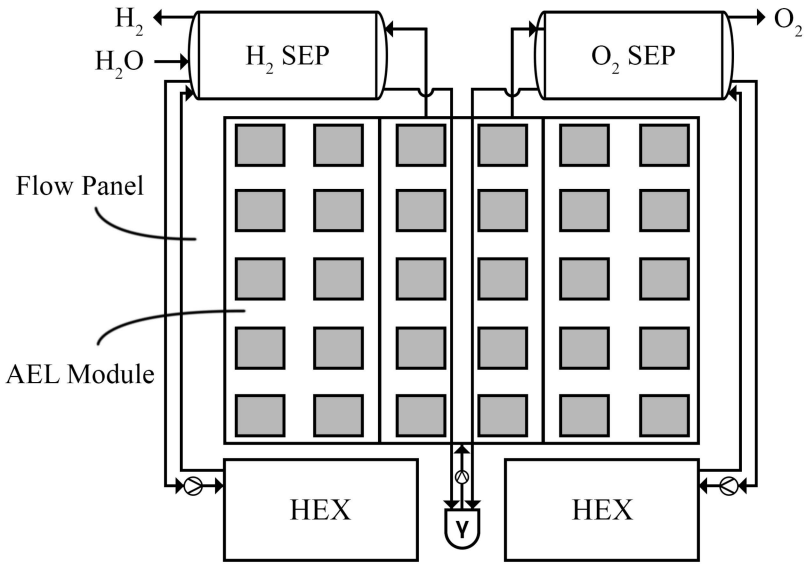

Figure 3.1: General overview of the XINTC system section; including component placement, and flow directions. The hydrogen and oxygen gas-liquid separators, denoted by H_2 SEP and O_2 SEP respectively, function as a buffer for the bulk liquid of the system. KOH electrolyte is circulated from the separators to the mixer, denoted by Y, and pump, to be distributed across the flow panels. The flow panels distribute the electrolyte across the AEL modules, illustrated by the grey squares. The gas-liquid product travels upwards toward its respective separator. The heat exchangers, denoted by HEX, collect and cool the liquid electrolyte present in the separators.

3.1 The Alkaline Electrolyzer Modules

Alkaline electrolysis is the preferred technology for the XINTC system, due to their durability and independence of rare earth materials. Each AEL module has a nominal capacity of 5.0-6.5 kW. Figure 3.2 shows a graphic illustration of the module design. All information regarding the AEL modules has been provided by XINTC. In this work, the design, sizing, and material selection of the AEL modules are omitted to respect confidentiality. Unclassified information that is of importance to this work is included when deemed necessary. At the time of writing, the hydrodynamic behaviour of the modules is unknown.

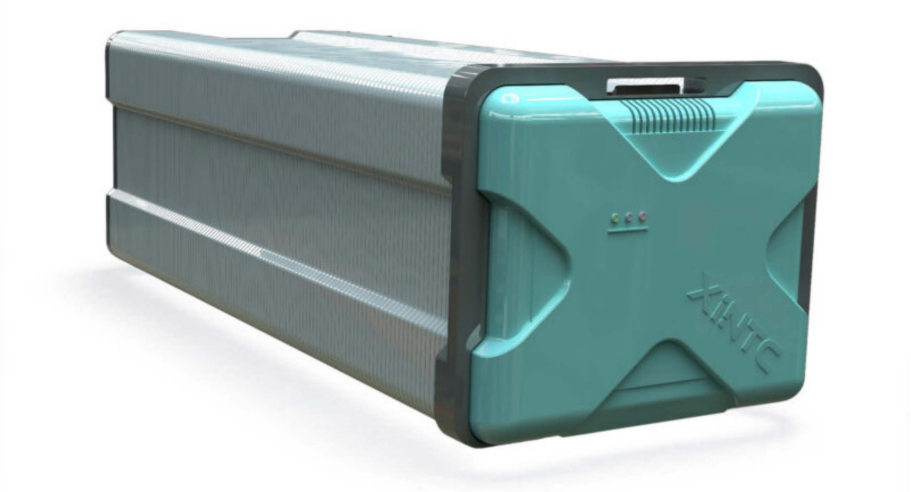

Figure 3.2: Graphic illustration of the XINTC EAL module.

3.1.1 Electrolyte Volumetric Flow Rate

Within the module cells, the electrolyte flow rate is positively correlated to heat dissipation [58]. However, the electrolyte flow rate is also positively correlated to the membrane gas-crossover rate [29, 59]. The volumetric flow rate of electrolyte within the module cells is thus limited by the maximum allowable gas-crossover through the cell membranes. Based on the work of Silvestros [29], the maximum volumetric flow rate within the module half-cells is set to $\dot{V}_{\text{hc}} = 50$ mL/min, limiting gas impurities to 0.5%. The total flow rate of electrolyte through a single module of n_{cell} number of cells, follows:

$$\dot{V}_{\text{EL}}^{\text{mod}} = 2\dot{V}_{\text{hc}} \cdot n_{\text{cell}} \tag{3.1}$$

where a factor 2 is introduced to account for each cell comprising of two half-cells.

3.1.2 Hydrogen Production

The molar hydrogen production rate of a module $\dot{n}_{\text{H}_2}$, is the product of the cell production rate, Equation (2.8), and n_{cell}. Respecting the stoichiometric relation of the overall reaction, Equation (R2.1), the molar production rate of oxygen in a module $\dot{n}_{\text{O}_2}$, is half of $\dot{n}_{\text{H}_2}$:

$$\dot{n}_{\text{H}_2} = \eta_{\text{F}} \frac{I_{\text{cell}} n_{\text{cell}}}{2F} \tag{3.2a}$$

$$\dot{n}_{\text{O}_2} = \eta_{\text{F}} \frac{I_{\text{cell}} n_{\text{cell}}}{4F} \tag{3.2b}$$

The mass flow rate of hydrogen and oxygen within a module ($\dot{m}_{H_2}$ and $\dot{m}_{O_2}$, respectively), are the product of their respective molar production rate, and molecular weight (M_{H_2} and M_{O_2}):

$$\dot{m}_{H_2} = M_{H_2}\dot{n}_{H_2} = M_{H_2}\left(\eta_F \frac{I_{cell} n_{cell}}{2F}\right) \tag{3.3a}$$

$$\dot{m}_{O_2} = M_{O_2}\dot{n}_{O_2} = M_{O_2}\left(\eta_F \frac{I_{cell} n_{cell}}{4F}\right) \tag{3.3b}$$

The volumetric flow rate of hydrogen and oxygen per module ($\dot{V}_{H_2}$ and $\dot{V}_{O_2}$, respectively), is the product of their respective mass flow rate, and density (ρ_{H_2} and ρ_{O_2}):

$$\dot{V}_{H_2} = \rho_{H_2}\dot{m}_{H_2} = \rho_{H_2}\left(M_{H_2}\eta_F \frac{I_{cell} n_{cell}}{2F}\right) \tag{3.4a}$$

$$\dot{V}_{O_2} = \rho_{O_2}\dot{m}_{O_2} = \rho_{O_2}\left(M_{O_2}\eta_F \frac{I_{cell} n_{cell}}{4F}\right) \tag{3.4b}$$

The Faradaic efficiency of the cells has been experimentally determined by XINTC, and will not be disclosed. It can, however, be stated that η_F can be expressed as solely a function of the cell current.

3.1.3 Heat Analysis

The large amount of heat generation within the modules offers one of the primary challenges for the section design. A qualitative evaluation of the heat generation within the stacks and their interaction with the ambient airflow is performed.

3.1.3.1 Heat generation in modules

Heat generation within the modules $\dot{Q}_{mod}$, occurs due to voltaic losses at the reaction-zone $\dot{Q}_U$, and current losses $\dot{Q}_I$:

$$\dot{Q}_{mod} = \dot{Q}_U + \dot{Q}_I \tag{3.5}$$

Current losses arise due to low resistance pathways within the module, called shunts. The current that travels across shunts is referred to as shunt current I_{shunt}. Figure 3.3 shows a schematic representation of the current flow directions within the module. The shunt current across the module is prominent at low current densities [58]. Faradaic efficiency η_F, of the module increases with current density, as in accordance with Equation (2.6). The heat generation because of the shunt current $\dot{Q}_I$ [W], is described as the product of I_{shunt}, and the applied module voltage U_{mod}:

$$\dot{Q}_I = U_{mod} I_{shunt} = U_{mod} I_{mod}\,(1 - \eta_F) \tag{3.6}$$

where

$$U_{mod} = n_{cell} U_{cell} \tag{3.7}$$

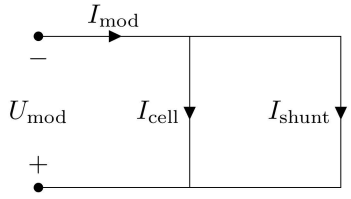

Figure 3.3: Schematic representation of current flow directions within the XINTC module. Here U_{mod} represents the applied module voltage; I_{mod} is the applied module current; I_{cell} is the portion of the current that reaches the cell reaction zone; I_{shunt} is the current loss due to shunts.

Voltaic losses arise due to a deviation between thermoneutral and applied cell voltage, as in accordance with η_{U}, Equation (2.5). The heat generation due to voltaic losses is described as the product of the current that makes it to the reaction zone, and the discrepancy between $n_{\mathrm{cell}} \cdot U_{\mathrm{tn}}$ and U_{mod}:

$$\dot{Q}_{\mathrm{U}} = (I_{\mathrm{mod}} - I_{\mathrm{shunt}})\,(U_{\mathrm{mod}} - U_{\mathrm{tn}} n_{\mathrm{cell}}) = I_{\mathrm{mod}} \eta_{\mathrm{F}} \cdot U_{\mathrm{mod}}\,(1 - \eta_{\mathrm{U}}) \tag{3.8}$$

The cell voltage as a function of I_{cell}, has been experimentally determined, and was provided by XINTC. Utilizing the relation between I_{cell} and U_{cell}, it is possible to determine the voltaic efficiency, and define an expression for the total efficiency for the modules η_{tot}:

$$\eta_{\mathrm{tot}} = \eta_{\mathrm{U}} \eta_{\mathrm{F}} \tag{3.9}$$

An expression for the total heat generation within a single module is presented by combining Equations (3.5) through (3.9):

$$\begin{aligned} \dot{Q}_{\mathrm{mod}} &= I_{\mathrm{mod}} \eta_{\mathrm{F}} \cdot U_{\mathrm{mod}}\,(1 - \eta_{\mathrm{U}}) + U_{\mathrm{mod}} I_{\mathrm{mod}}\,(1 - \eta_{\mathrm{F}}) \\ &= I_{\mathrm{mod}} U_{\mathrm{mod}} (\eta_{\mathrm{F}}(1 - \eta_{\mathrm{U}}) + 1 - \eta_{\mathrm{F}}) \\ &= U_{\mathrm{mod}} I_{\mathrm{mod}} (1 - \eta_{\mathrm{tot}}) \end{aligned} \tag{3.10}$$

The heat generation of an AEL module can be expressed as a function of solely I_{cell}, since U_{mod} is a function of I_{cell}. Figure 3.4 shows the relation between I_{cell}, and the total heat generated by all the modules of a section $\dot{Q}_{\mathrm{mod}}^{\mathrm{sec}}$.

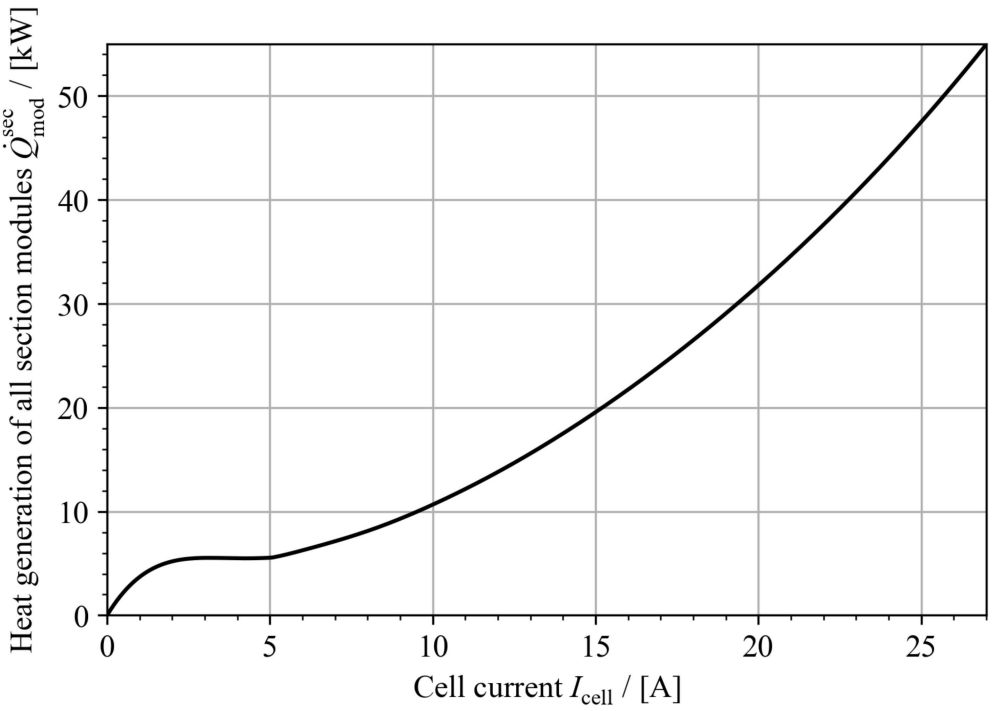

Figure 3.4: Relation between cell current I_{cell}, and the total heat generated by the modules of a section $\dot{Q}_{\mathrm{mod}}^{\mathrm{sec}}$. The behaviour for $I_{\mathrm{cell}} < 5$ is a result of the expression used for the voltaic efficiency η_{U}, based on the relation between I_{cell} and U_{mod}.

3.1.3.2 Convective Heat Transfer

The methods used to determine the convective heat transfer are covered in Appendix B. It is assumed that the modules behave as horizontal cylinders in an aligned tube bank configuration. The

methods described in B.4 are used to translate the average Nusselt number of a singular module to the average Nusselt number for modules in an aligned tube bank configuration.

Natural convection
The Rayleigh number Ra, is evaluated to determine the average Nusselt number for natural convection across a module $\overline{Nu}_{\text{nat}}^{\text{mod}}$. It is concluded that the airflow across the modules due to natural convection is always in the laminar regime ($Ra < 10^9$). As a result, $\overline{Nu}_{\text{nat}}^{\text{mod}}$ is calculated using Equation (B.6a).

Forced convection
The Reynolds number Re, is evaluated to determine the average Nusselt number for forced convection across a module $\overline{Nu}_{\text{forc}}^{\text{mod}}$. It is necessary to calculate the average air velocity around a module $\overline{v}_{\text{air}}^{\text{mod}}$, to determine Re. The volumetric flow rate of air $\dot{V}_{\text{air}}$, follows from the ventilation requirement. An expression for $\overline{v}_{\text{air}}^{\text{mod}}$ follows:

$$\overline{v}_{\text{air}}^{\text{mod}} = \dot{V}_{\text{air}}/(W_{\text{sec}}L_{\text{sec}} - n_{\text{col}}W_{\text{mod}}L_{\text{mod}}) \tag{3.11}$$

with section width W_{sec}, section length L_{sec}, module width W_{mod}, module length L_{mod}, and the number of AEL module columns n_{col}. It is concluded that airflow due to forced convection across the modules is in the turbulent regime when the minimum ventilation requirement is met ($Re > 10^4$). The value of $\overline{Nu}_{\text{forc}}^{\text{mod}}$ is calculated using Equation (B.12), along with the methods described in section B.4.

Dominant mode of convection
As described in Appendix B.3, the dominant mode of convection is determined by evaluating the value of the dimensionless property Gr/Re^2 [60]. Table B.1 describes the criteria for the forced, mixed, and natural convection regions. Figure 3.5 shows the relation between the volumetric flow rate of air $\dot{V}_{\text{air}}$ [m^3/h] and Gr/Re^2, at various temperature ranges ΔT. Cut-off values of $Gr/Re^2 = 2$ and $Gr/Re^2 = 0.3$, are considered for the natural and forced regions, respectively. ΔT represents the difference in operating temperature and ambient temperature. It is concluded that forced convection is the dominant mode of convective heat transfer for all operating conditions ($Gr/Re^2 \ll 1$).

Air-side Heat Transfer Coefficient
Making a conclusive statement regarding the convective heat transfer across the modules is impossible. The conductive heat transfer coefficient and internal convective heat transfer coefficient are required to determine the overall heat transfer coefficient. Only the air-side heat transfer coefficient can be determined with the information available at the point of writing. Figure 3.6 shows the air-side heat transfer coefficient $h_{\text{c}}^{\text{air}}$ [Wm^{-2}K^{-1}], for the modules in an aligned tube-bank configuration for $\Delta T = 20$ °C. It is observed that the heat transfer coefficient undergoes a sudden change at $\dot{V}_{\text{air}} \approx 400$ m^3/h, and $\dot{V}_{\text{air}} \approx 1000$ m^3/h. These changes are in accordance with the values of $\dot{V}_{\text{air}}$ at which the convective flow region changes, as is shown in Figure 3.5.

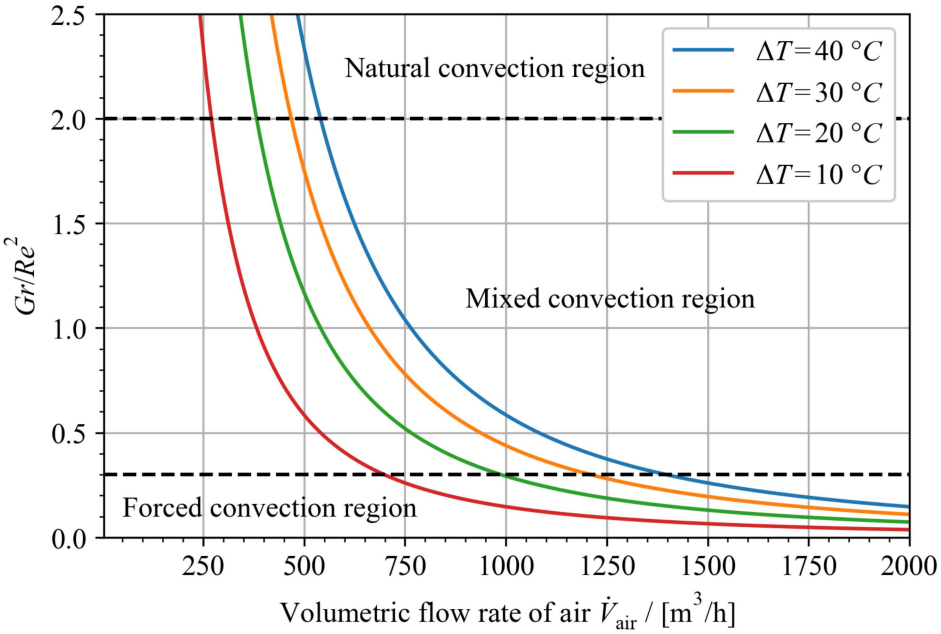

Figure 3.5: Mode of convection selection criterion Gr/Re^2, as a function of air volumetric flow rate $\dot{V}_{\text{air}}$, at various temperature ranges ΔT. Cut-off values for each respective convection region are denoted by the black striped lines.

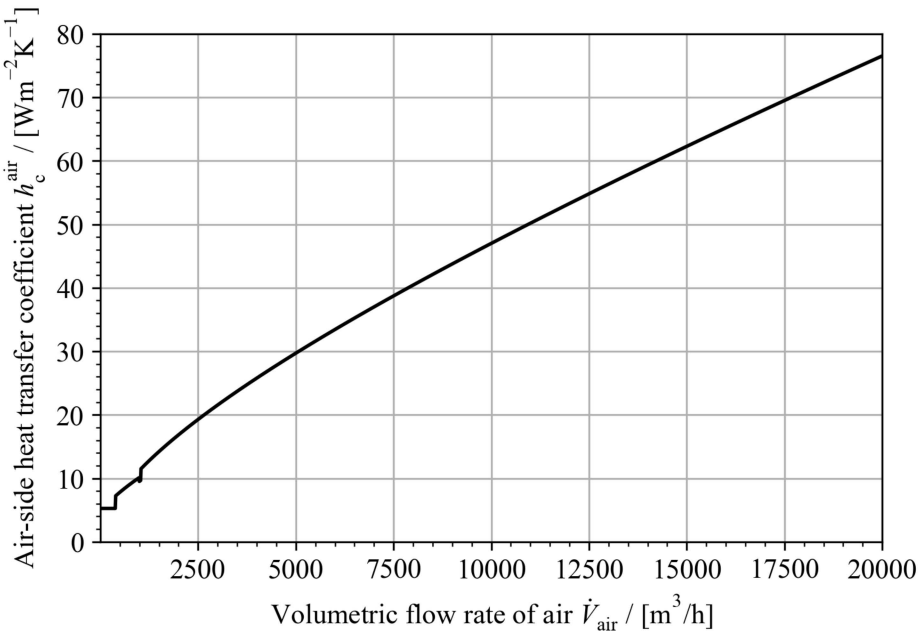

Figure 3.6: Air-side heat transfer coefficient $h_{\text{c}}^{\text{air}}$, for the modules in an aligned tube-bank configuration, as a function of the volumetric flow rate of air $\dot{V}_{\text{air}}$. Values are provided for a temperature difference between the system and air of $\Delta T = 20$ °C. Sudden changes observed in $h_{\text{c}}^{\text{air}}$ are in accordance with the change of convective flow region, as shown in Figure 3.5.

3.2 The Heat Exchangers

An air cooling solution is investigated, as the XINTC system should be capable of off-the-grid performance. The hot flow in this system consists of the liquid electrolyte, and the cold flow consists of ambient air. In this section, a heat exchanger design is proposed, and the corresponding heat transfer performance, as well as pressure drop, will be calculated.

3.2.1 Design

Heat exchangers (HEX) are typically designed to be single-stage or two-stage; both of which will be discussed in this section.

3.2.1.1 Two-Stage Heat Exchanger

Spacial limitations within the container are the main challenge of the HEX design. HEX performance is related to its effective surface area, i.e., spacial limitations result in lowered performance. This challenge can be circumvented by implementing a two-stage HEX. In this approach the primary cooling stage is placed outside of the container. The primary cooling stage consists of an air-cooled HEX that cools a coolant. The coolant travels to the second stage consisting of a dedicated HEX (such as a shell-and-tube HEX), where it cools the electrolyte. A more innovative approach would be to implement the second stage into the separator tanks, since the separators contain the bulk of liquid volume within the section. In this design, the separator tanks function as shell-and-tube HEX simultaneously. Figure 3.7 shows an illustrative example of what such a HEX design would look like. Ensuring sufficient heat exchange between the tube-side coolant, and the shell-side liquid electrolyte provides the main challenge of this design, since the liquid electrolyte only occupies approximately half of the volume. This design can be summarized with a few key advantages and disadvantages denoted in the following list by + and -, respectively:

+ Spacial limitations are circumvented in the first stage.
+ No additional space is occupied within the section due to the separator tanks being already present. The resulting vacant space can be used to increase the number of section modules
+ Convenient integration of external liquid cooling. This design allows the consumer to bypass the first cooling stage, and connect directly with pre-existing liquid cooling systems.
– Does not utilize airflow present due to ventilation requirement.
– Requires significant modification to the separators tanks; potentially affecting separator performance.
– Introduces a second liquid component into the system, and thus potential risk of internal leakage.
– Requires a non-conducting cooling medium to ensure galvanic insulation.

Although applicable; the two-stage separator HEX design is not further considered in this report. The addition of an external air cooler (such as a roof cooling unit), creates a slippery-slope when it comes to system boundaries. The main goal of this work is to design a section for the XINTC system. Whenever solutions are sought outside of the system boundaries it takes away from its containerized and plug-and-play nature. A different approach is suggested.

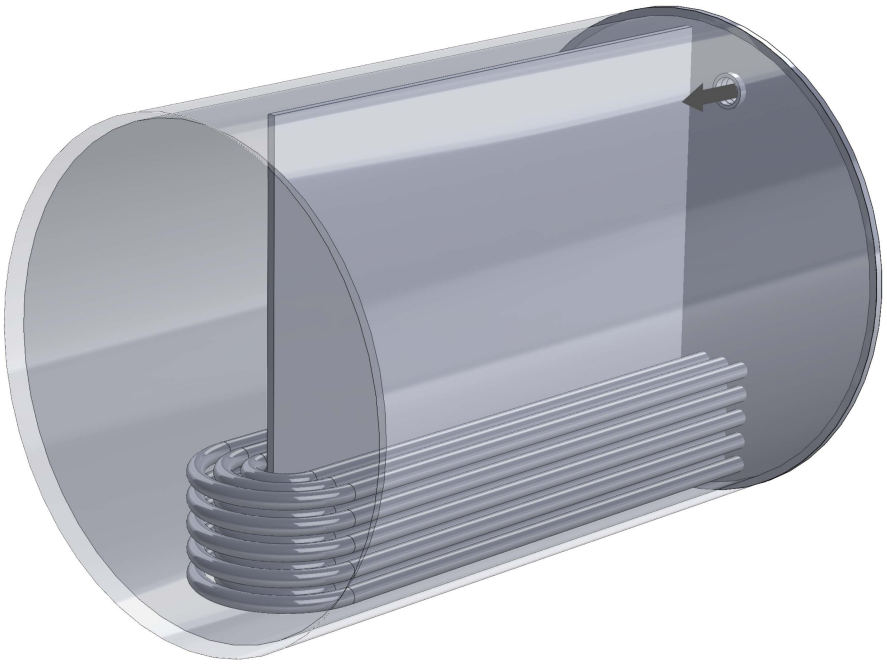

Figure 3.7: Illustrative example of counter-current, shell-and-tube HEX and gas-liquid separator. The figure shows the 2nd stage of a two-stage heat exchanger setup. Metallic tubes contain cooling liquid originating from the primary air-cooling stage. The tubes are submerged in the liquid electrolyte contained by the gas-liquid separator tanks, allowing for heat transfer between the cooling liquid and electrolyte.

3.2.1.2 Single-stage Heat Exchanger

In a single-stage HEX, the cold fluid directly cools the hot fluid. In this case, air will be utilized to cool the liquid electrolyte directly. A single-stage HEX profits from the pre-existing airflow introduced by the ventilation requirements of the section. The main challenge of designing a single-stage HEX is achieving sufficient cooling performance. The spatial limitations, and relatively low convective heat transfer coefficients associated with gas flows necessitate the use of a high area-to-volume ratio HEX. Typically cross-flow finned tube heat exchangers are used in air cooling systems [61, 62, 60]. Finned tubes contain fins to increase effective surface area. There is, however, a major issue when it comes to finned tubes. Finned tubes are most commonly manufactured by welding a ribbon of equal material to the tube [61]. The highly corrosive nature of the electrolyte precludes the welding of any components it comes into direct contact with, as weld defects could result in leakage. The electrolyte also necessitates the usage of chemically resistant materials; typically stainless steel. The conductive heat transfer coefficient of stainless steel is much lower compared to materials typically used in HEX design; typically aluminium [23, 62]. Instead, a design is suggested that is able to cope with the corrosive electrolyte, and enables the utilization of said materials.

Plate-finned tube heat exchanger
A plate-finned tube heat exchanger (PFTHEX) design, as shown in Figure 3.8, is suggested. In a PFTHEX, tubes are press-fitted to the plate-fins. A large area of the PFTHEX (the plate-fins) can thus be manufactured from aluminium; offering far greater heat transfer performance than stainless steel [23]. Stainless steel tubing should still be used due to its direct contact with the electrolyte. Figure 3.9 shows a close-up of the architecture of a PFTHEX. Note that in this work

the terms PFTHEX and radiator are used interchangeably. It is recommended to utilize a radiator pair, as it offers a number of advantages when compared to a single radiator. First, the pressure drop is approximately halved when comparing a radiator pair of half a section width each, to a single radiator spanning an entire section width. Second, connecting a dedicated radiator to each separator results in greater system temperature control. The specifications of the radiator considered in this work are provided by XINTC, and are based on the data-sheet provided by its manufacturer. In this section, the properties of the PFTHEX are described, and models for its thermal and hydrodynamic behaviour are presented and quantified.

Figure 3.8: Illustration of the plate-finned tube heat exchanger design. Cold air flows through the face of the radiator. Liquid electrolyte is distributed across the tube rows; containing multiple tube passes.

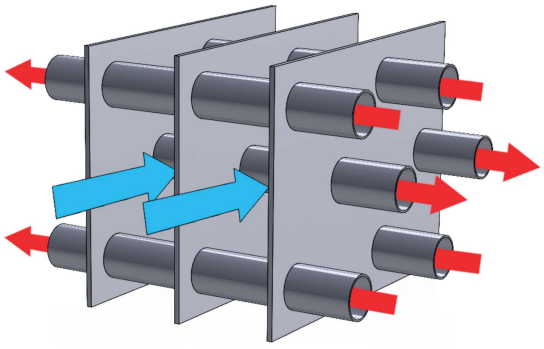

Figure 3.9: Close-up illustration of the plate-finned tube heat exchanger design; including hot and cold flow directions shown by red and blue arrows, respectively.

3.2.2 Heat Transfer Performance

Expressions for the air-side and tube-side convective heat transfer coefficients ($h_{\text{air}}^{\text{rad}}$ and $h_{\text{tube}}^{\text{rad}}$, respectively), and effective and internal area (A_{rad} and $A_{\text{i}}^{\text{tube}}$, respectively), are required to assess radiator performance. A thermal resistance network model is utilized to determine the heat transfer coefficient of a single radiator. Figure 3.10 shows the resistance model in accordance with the radiator design, where $k_{\text{ss}} = 25$ Wm^{-1}K^{-1} represents the thermal conductivity, of –in this case– stainless steel [23].

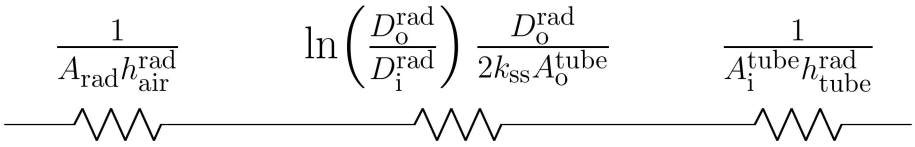

Figure 3.10: Resistance model overview of heat transfer between a single radiator and air. From left to right, the resistances represent the thermal resistance introduced by: the air-side heat transfer coefficient $h_{\text{air}}^{\text{rad}}$, the thermal conductivity of the tube, and the tube side heat transfer coefficient $h_{\text{tube}}^{\text{rad}}$.

3.2.2.1 Heat Transfer Area

Tube-side heat transfer area

The total number of effective tubes per radiator n_{tube}, is the product of the number of tube rows n_{row}, and the number of tube passes n_{pass}:

$$n_{\text{tube}} = n_{\text{pass}} \cdot n_{\text{row}} \tag{3.12}$$

It is assumed that the flow within the tube bends has little influence on the total heat transfer coefficient, as it is not in direct contact with the plates. For a radiator length of L_{rad}, the tube-side inner heat transfer area $A_{\text{i}}^{\text{tubes}}$, follows:

$$A_{\text{i}}^{\text{tubes}} = \pi D_{\text{i}}^{\text{rad}} L_{\text{rad}} n_{\text{tube}} \tag{3.13}$$

Air-side heat transfer area

The total number of radiator plates per radiator depends on plate thickness t_{plate}, plate spacing δ_{plate}, and L_{rad}:

$$n_{\text{plate}} = \text{floor}\left(\frac{L_{\text{rad}}}{t_{\text{plate}} + \delta_{\text{plate}}}\right) \tag{3.14}$$

Total radiator surface area is the sum of the plate area A_{plates}, and the bare tube area A_{tubes}:

$$A_{\text{rad}} = A_{\text{plates}} + A_{\text{tubes}} \tag{3.15}$$

Total plate area A_{plates} should account for both plate sides, and the cross-sectional area of the tube holes:

$$A_{\text{plates}} = 2n_{\text{plate}}\left[W_{\text{rad}} H_{\text{rad}} + t_{\text{plate}} n_{\text{plate}} H_{\text{rad}} - \frac{\pi}{4}(D_{\text{o}}^{\text{rad}})^2 n_{\text{tube}}\right] \tag{3.16}$$

where $D_{\text{o}}^{\text{rad}}$ is the outer tube diameter, and W_{rad} and H_{rad} denote the radiator width and height, respectively. Similarly, the total area of the bare tubes $A_{\text{o}}^{\text{tubes}}$, is:

$$A_{\text{o}}^{\text{tubes}} = n_{\text{tube}} \cdot \pi D_{\text{o}}^{\text{rad}} (L_{\text{rad}} - t_{\text{plate}} \cdot n_{\text{pate}}) \tag{3.17}$$

A final expression for A_{rad} follows:

$$\begin{aligned} A_{\text{rad}} = {} & 2 \cdot n_{\text{plate}}\left[W_{\text{rad}} H_{\text{rad}} + t_{\text{plate}} n_{\text{plate}} H_{\text{rad}} - \frac{\pi}{4}(D_{\text{o}}^{\text{rad}})^2 n_{\text{tube}}\right] \\ & + n_{\text{tube}} \cdot \pi D_{\text{o}}^{\text{rad}} (L_{\text{rad}} - t_{\text{plate}} \cdot n_{\text{pate}}) \end{aligned} \tag{3.18}$$

3.2.2.2 Tube-side Heat Transfer Coefficient

For optimal performance, it is important that the flow regime within the radiator tubes is turbulent. Care must be taken to avoid the transitional flow regime ($2500 - 10^4$ Re), due to unpredictable flow behaviour within this regime [60]. The minimum tube-side flow speed, that maximizes radiator performance is presented as a function of the tube's inner diameter:

$$v_{\text{tube}}^{\text{min}} > \frac{\mu_{\text{EL}}}{\rho_{\text{EL}} D_{\text{i}}^{\text{rad}}} \cdot 10^4 = 1.34 \text{ m/s} \tag{3.19}$$

where μ_{EL} [Pa·s], and ρ_{EL} [kg/m^3], denote the electrolyte dynamic viscosity and density, respectively. The material properties of the electrolyte are determined through the methods described in Appendix A. The tube-side heat transfer coefficient is determined through its relation with Nu, Equation (B.2). Nu is determined through the method described in Appendix B, and more specifically Equation (B.10). Note that the relative viscosity term will be omitted. Viscosity in the bulk liquid μ_{b}, is approximately equal to the viscosity at the wall μ_{w}, because the electrolyte undergoes a relatively small change in temperature, and the flow is assumed to be highly mixed in the turbulent regime. Equation (B.10) shows that the convective heat transfer coefficient is related to v_{tube} through Re, i.e., tube-side heat transfer increases with v. It is recommended to isolate the electrolyte flow loop for each radiator and separator pair from the modules. Bypassing the modules circumvents the upper limit of liquid flow rate introduced by the gas crossover limit within the modules.

3.2.2.3 Air-side Heat Transfer Coefficient

The air-side heat transfer coefficient is estimated through literature. In 1998, Wang et al. [63, 64] published a meta-analysis of plain plate-finned tube heat exchangers. They developed a correlation for the air-side Colburn factor of a PFTHEX with plain fins. The correlation was based on experiments containing 18 test samples [63], and 74 samples sourced from literature [64]. The Colburn factor j, is a dimensionless number used to characterize the convective heat transfer efficiency [60]. It is defined as a function of the Reynolds, Nusselt, and Prandtl numbers:

$$j \equiv \frac{Nu}{RePr^{1/3}} \tag{3.20}$$

The relation presented by Wang et al. [64], j is a function of n_{row}, the Reynolds number with respect to the outer tube diameter $Re_{D_{\text{o}}}$, the transverse and longitudinal tube pitch (P_{T} and P_{L}, respectively), the fin pitch F_{p}, and the hydraulic diameter D_{h}. More information regarding the hydraulic diameter is provided in Appendix C.1. The fin pitch is defined as:

$$F_{\text{p}} \equiv \delta_{\text{plate}} + t_{\text{plate}} \tag{3.21}$$

The correlation presented by Wang et al. for a single row plain PFTHEX ($n_{\text{row}} = 1$), reads [64]:

$$j = 0.0108 Re_{D_{\text{o}}}^{-0.29} \left(\frac{P_{\text{T}}}{P_{\text{L}}}\right)^{P1} \left(\frac{F_{\text{p}}}{D_{\text{o}}}\right)^{-1.084} \left(\frac{F_{\text{p}}}{D_{\text{h}}}\right)^{-0.786} \left(\frac{F_{\text{p}}}{P_{\text{T}}}\right)^{P2} \tag{3.22}$$

where

$$P1 = 1.9 - 0.23 \ln\left(Re_{D_{\text{o}}}\right) \tag{3.23a}$$

$$P2 = -0.236 + 0.126 \ln\left(Re_{D_{\text{o}}}\right) \tag{3.23b}$$

For more than a single single tube row ($n_{\text{row}} > 1$), j is approximated by [64]:

$$j = 0.086 Re_{D_{\text{o}}}^{P3} \cdot n_{\text{row}}^{P4} \left(\frac{F_{\text{p}}}{D_{\text{o}}}\right)^{P5} \left(\frac{F_{\text{p}}}{D_{\text{h}}}\right)^{P6} \left(\frac{F_{\text{p}}}{P_{\text{T}}}\right)^{-0.93} \tag{3.24}$$

where

$$P3 = -0.361 - \frac{0.042 n_{\text{row}}}{\ln\left(Re_{D_\text{o}}\right)} + 0.158 \ln\left[n_{\text{row}} \left(\frac{F_\text{p}}{D_\text{o}}\right)^{0.41}\right] \tag{3.25a}$$

$$P4 = -1.224 - \frac{0.076 \left(\frac{P_\text{L}}{D_\text{h}}\right)^{1.42}}{\ln\left(Re_{D_\text{o}}\right)} \tag{3.25b}$$

$$P5 = -0.083 + \frac{0.058 n_{\text{row}}}{\ln\left(Re_{D_\text{o}}\right)} \tag{3.25c}$$

$$P6 = -5.735 + 1.21 \ln\left(\frac{Re_{D_\text{o}}}{n_{\text{row}}}\right) \tag{3.25d}$$

Equation (3.20) is used to determine Nu through j, and in turn the air-side heat transfer coefficient $h_{\text{air}}^{\text{rad}}$ [$\text{Wm}^{-2}\text{K}^{-1}$], is determined through Equation (B.2).

3.2.2.4 Total Heat Transfer of Radiators

The overall heat transfer coefficient of a single radiator U_{rad} [$\text{Wm}^{-2}\text{K}^{-1}$], is based on the resistance network model illustrated in Figure 3.10:

$$\frac{1}{U_{\text{rad}} A_{\text{rad}}} = \frac{1}{A_{\text{rad}} h_{\text{air}}^{\text{rad}}} + \ln\left(\frac{D_\text{o}^{\text{rad}}}{D_\text{i}^{\text{rad}}}\right) \frac{D_\text{o}^{\text{rad}}}{2 k_{\text{ss}} A_\text{o}^{\text{tube}}} + \frac{1}{A_\text{i}^{\text{tube}} h_{\text{tube}}^{\text{rad}}} \tag{3.26}$$

The overall heat transfer coefficient relates to the heat flux $\dot{Q}_{\text{rad}}$ [W], providing an expression for the cooling performance of the radiator:

$$\dot{Q}_{\text{rad}} = U_{\text{rad}} A_{\text{rad}} \Delta T \tag{3.27}$$

where ΔT is the temperature difference between the hot and cold inlet streams:

$$\Delta T = T_{\text{in}}^{\text{EL}} - T_{\text{in}}^{\text{air}} \tag{3.28}$$

Solving Equation (3.26) for U_{rad}, and filling it into (3.27) results in a value for $\dot{Q}_{\text{rad}}$ far greater than the theoretical maximum heat flow. In reality, the heat transfer within the plain PFTHEX is limited by the amount of heat each fluid is capable of exchanging [65]. The change in temperature of a flow is dependent on its specific heat capacity c_p [$\text{Jkg}^{-1}\text{K}^{-1}$], and mass flow rate $\dot{m}$ [kg/s]. Heat capacity C [J/K], is a property that describes the amount of heat necessary to change the temperature of a given amount of matter. The heat required to change the temperature of a flow can be described by the following expression:

$$\dot{Q} = \dot{m} c_\text{p} \Delta T = \dot{C} \Delta T \tag{3.29}$$

with the heat flow capacity $\dot{C}$ [W/K], defined as:

$$\dot{C} \equiv \frac{\text{d}C}{\text{d}t} = \dot{m} c_\text{p} \tag{3.30}$$

For mathematical convenience, the minimum heat flow capacity $\dot{C}_{\text{min}}$, maximum heat flow capacity $\dot{C}_{\text{max}}$, and heat flow capacity ratio $\dot{C}^*$ are introduced:

$$\dot{C}_{\text{min}} \equiv \min\left(c_\text{p}^{\text{EL}} \dot{m}_{\text{EL}},\ c_\text{p}^{\text{air}} \dot{m}_{\text{air}}\right) \tag{3.31}$$

$$\dot{C}_{\text{max}} \equiv \max\left(c_\text{p}^{\text{EL}} \dot{m}_{\text{EL}},\ c_\text{p}^{\text{air}} \dot{m}_{\text{air}}\right) \tag{3.32}$$

$$\dot{C}^* \equiv \frac{\dot{C}_{\text{min}}}{\dot{C}_{\text{max}}} \tag{3.33}$$

Theoretical maximum heat flow of a single radiator $\dot{Q}^{\text{rad}}_{\text{max}}$, is dominated by the flow least capable of heat exchange, i.e., the flow for which $\dot{C} = \dot{C}_{\text{min}}$:

$$\dot{Q}^{\text{rad}}_{\text{max}} = \Delta T \dot{C}_{\text{min}} \tag{3.34}$$

The effectiveness-NTU method is applied to determine the effectiveness of the heat exchange between hot and cold flows. First, the Number of Transfer Units NTU, is determined. NTU is a dimensionless number defined as the ratio of $\dot{Q}_{\text{rad}}$, to $\dot{Q}^{\text{rad}}_{\text{max}}$ [65]:

$$NTU_{\text{rad}} \equiv \frac{\dot{Q}_{\text{rad}}}{\dot{Q}_{\text{max}}} = \frac{U_{\text{rad}} A_{\text{rad}}}{\dot{C}_{\text{min}}} \tag{3.35}$$

Next, the effectiveness of the HEX is determined. The effectiveness ε, is a dimensionless property defined as the ratio of real heat flow $\dot{Q}^{\text{rad}}_{\text{real}}$, to $\dot{Q}_{\text{max}}$ [65]:

$$\varepsilon \equiv \frac{\dot{Q}^{\text{rad}}_{\text{real}}}{\dot{Q}_{\text{max}}} \tag{3.36}$$

For a cross-flow HEX with more than 4 tube-rows ε is given by [63]:

$$\varepsilon_{\text{rad}} = 1 - \exp\left[\frac{NTU^{0.22}_{\text{rad}}}{\dot{C}^*} \exp(-\dot{C}^* \cdot NTU^{0.78}_{\text{rad}} - 1)\right] \tag{3.37}$$

Finally, the real heat flow, and thus cooling performance of the radiator pair is obtained from the definition of the effectiveness, Equation (3.36):

$$\dot{Q}^{\text{sec}}_{\text{rad}} = 2 \cdot \varepsilon \cdot \dot{Q}^{\text{rad}}_{\text{max}} \tag{3.38}$$

where a factor 2 is introduced to account for both radiators. Equation (3.27) shows a linear relation between $\dot{Q}$ and ΔT. Figure 3.11 shows the cooling performance of the radiator pair per unit temperature difference $\dot{Q}^{\text{sec}}_{\text{rad}}/\Delta T$ [kW/K], as a function volumetric flow rate of air $\dot{V}_{\text{air}}$, at $v_{\text{tube}} = 2$ m/s, and $T^{\text{air}}_{\text{in}} = 20$ °C. Figure 3.12 shows $\dot{Q}^{\text{sec}}_{\text{rad}}/\Delta T$, as a function of tube-side flow velocity v_{tube}, at $\dot{V}_{\text{air}} = 12000$ m^3/h. The sudden drop in $\dot{Q}^{\text{sec}}_{\text{rad}}/\Delta T$, observed at $v_{\text{tube}} = 0.33$ m/s, in Figure 3.12, is a result of the change from laminar to the transitional regime, and is in accordance with Equation B.10. Based on the model provided, and within expected operating temperature ranges, temperature-induced variations of air and electrolyte properties (e.g., μ, c_{p}, ρ, and k), have little effect on cooling performance. Comparing the extremes of the range of operation $T^{\text{air}}_{\text{in}} = -10$ °C, and $T^{\text{air}}_{\text{in}} = 35$ °C, the deviation in $\dot{Q}^{\text{sec}}_{\text{rad}}/\Delta T$ is less than 10%. Remarks comparing the radiator pair cooling capacity to the heat generation in the modules will be discussed in section 4.2.

3.2.3 Hydrodynamics

The pressure drop induced by the radiators on both the air and tube-side are to be determined. Appendix C contains information on various topics significant to this section. It will be explicitly mentioned when Appendix C is consulted. Note that channel, pipe, and conduit are used interchangeably in this report.

3.2.3.1 Air-side Pressure Drop

Total air-side pressure drop equals that of a single radiator, as the pressure losses along the radiator pair are in a parallel configuration. The largest pressure drop is expected to occur where the airflow velocity is highest, i.e., where the cross-sectional area is minimal. The minimum cross-sectional area is described as:

$$A^{\text{min}}_{\text{c}} = H_{\text{rad}} \left(L_{\text{rad}} - t_{\text{plate}} \cdot n_{\text{plate}}\right) - n_{\text{tube}} \cdot D^{\text{rad}}_{\text{o}} (L_{\text{rad}} - t_{\text{plate}} \cdot n_{\text{plate}}) \tag{3.39}$$

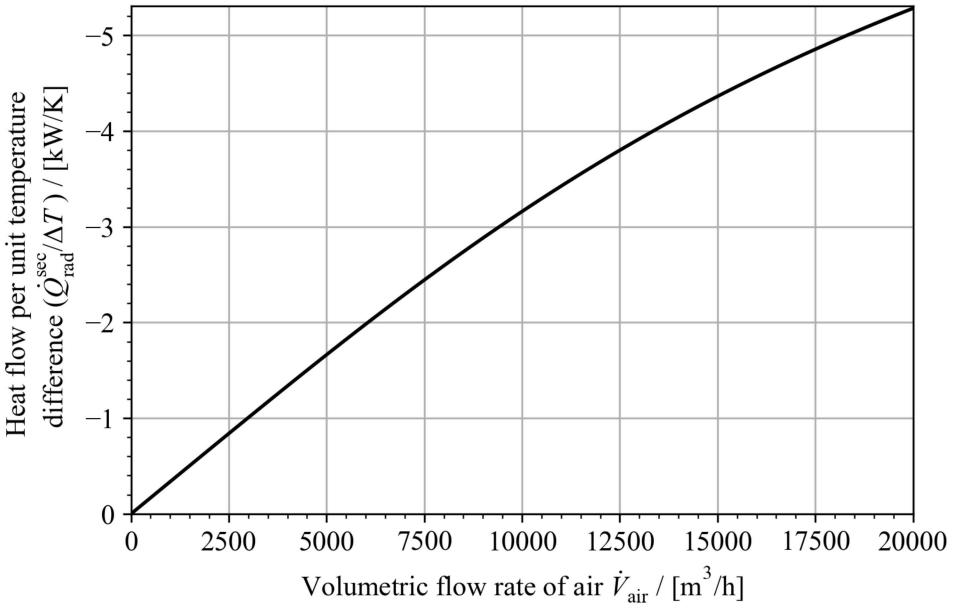

Figure 3.11: Total heat flow of the radiator pair per unit temperature difference $\dot{Q}^{sec}_{rad}/\Delta T$ [kW/K], as a function of the volumetric flow rate of air $\dot{V}_{air}$, at $v_{tube} = 2$ m/s $\wedge$ $T^{air}_{in} = 20$ °C. E.g., for $\dot{V}_{air} = 12000$ m^3/h, and $\Delta T = 10$ °C, radiator pair heat flow is: $\dot{Q}^{sec}_{rad}$ = -37 kW.

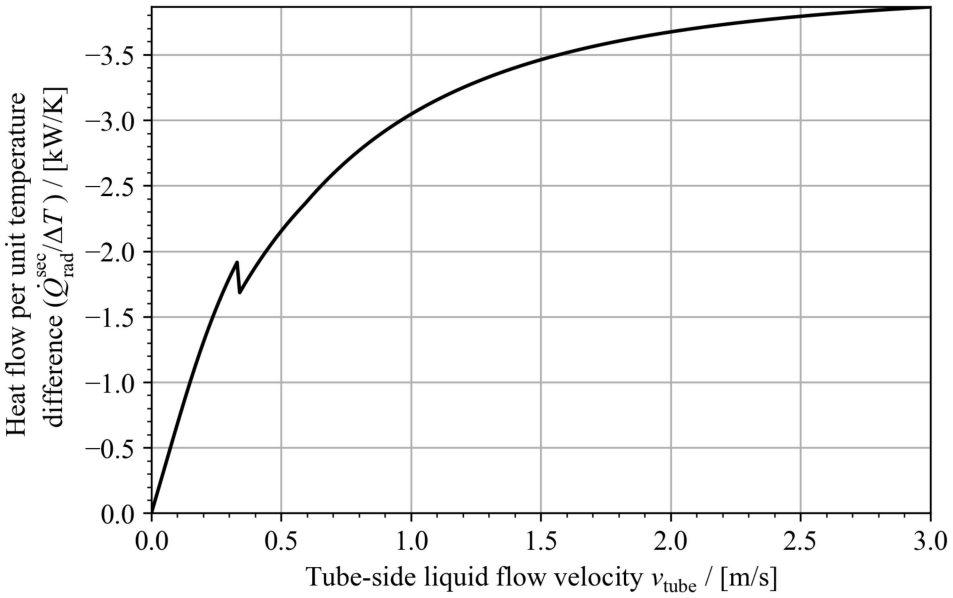

Figure 3.12: Total heat flow of the radiator pair per unit temperature difference $\dot{Q}^{sec}_{rad}/\Delta T$ [kW/K], as a function of tube-side flow velocity v_{tube}, at $\dot{V}_{air} = 12000$ m^3/h $\wedge$ $T^{air}_{in} = 20$ °C. E.g., for $v_{tube} = 2$ m/s, and $\Delta T = 10$ °C, radiator pair heat flow is: $\dot{Q}^{sec}_{rad}$ = -37 kW. The sudden drop in $\dot{Q}^{sec}_{rad}$, observed at $v_{tube} = 0.3$ m/s, is a result of the tube flow transitioning from the laminar flow regime to the transitional flow regime; in accordance with Equation B.10.

Next to the expression for the Colburn factor, Wang et al. [63, 64], provided a correlation for the air-side friction factor f. The friction factor is a dimensionless quantity that represents the resistance to fluid flow in a channel. It is typically used to calculate the pressure drop in fluid flow systems. Similar to the Colburn factor, the correlation derived by Wang et al. is based on experiments performed on 18 test samples [63], and 74 samples sourced from literature [64]. The correlation reads:

$$f = 0.0267 Re_{D_\mathrm{o}}^{F1} \left(\frac{P_\mathrm{T}}{P_\mathrm{L}}\right)^{F2} \left(\frac{F_\mathrm{p}}{D_\mathrm{o}}\right)^{F3} \tag{3.40}$$

where

$$F1 = -0.764 + 0.739\frac{P_\mathrm{T}}{P_\mathrm{L}} + 0.177\frac{F_\mathrm{p}}{D_\mathrm{o}} - \frac{0.00758}{n_\mathrm{row}} \tag{3.41a}$$

$$F2 = -15.689 + \frac{64.021}{\ln(Re_{D_\mathrm{o}})} \tag{3.41b}$$

$$F3 = 1.696 - \frac{15.695}{\ln(Re_{D_\mathrm{o}})} \tag{3.41c}$$

Wang et al. correlated the experimentally determined pressure drop to the friction factor through a relation provided by Kays and London [66]. An expression for the air-side pressure drop $\Delta P_\mathrm{air}^\mathrm{rad}$, as a function of f is found [60, 67]:

$$\Delta P_\mathrm{air}^\mathrm{rad} = \frac{v_\mathrm{max}^2 \rho_\mathrm{in}^\mathrm{air}}{2} \left[(1+\sigma_\mathrm{o}^2)\left(\frac{\rho_\mathrm{in}^\mathrm{air}}{\rho_\mathrm{out}^\mathrm{air}} - 1\right) + \frac{f}{4}\frac{A_\mathrm{rad}}{A_\mathrm{c}^\mathrm{min}}\frac{\rho_\mathrm{in}^\mathrm{air}}{\rho_\mathrm{m}^\mathrm{air}}\right] \tag{3.42}$$

with $\rho_\mathrm{in}^\mathrm{air}$ and $\rho_\mathrm{out}^\mathrm{air}$ the densities of the air at the inlet and outlet, respectively; $\rho_\mathrm{m}^\mathrm{air}$ the mean density of the airflow, and σ_o the contraction ratio of the cross-sectional area:

$$\sigma_\mathrm{o} \equiv \frac{A_\mathrm{c}^\mathrm{min}}{L_\mathrm{rad} H_\mathrm{rad}} \tag{3.43}$$

Equation (3.47) does not account for the inlet and outlet pressure drop. However, as f is based on experimental data, the inlet and outlet effects are accounted for in the friction coefficient [63, 60]. Air density is solely a function of temperature, as air can be treated as incompressible at flow speeds below 100 m/s [68]. The mean density is thus a function of the mean temperature T_m, within the radiator:

$$\rho_\mathrm{m}^\mathrm{air}(T) = \rho_{air}(T_\mathrm{m}) \tag{3.44}$$

The mean temperature is approximated by the logarithmic mean temperature:

$$T_\mathrm{m} \approx \frac{T_\mathrm{out}^\mathrm{air} - T_\mathrm{in}^\mathrm{air}}{\ln\left(\frac{T_\mathrm{out}^\mathrm{air}}{T_\mathrm{in}^\mathrm{air}}\right)} \tag{3.45}$$

Since $\rho \propto T^{-1}$, it can be stated that $\rho_\mathrm{m}^\mathrm{air} > \rho_\mathrm{out}^\mathrm{air}$. It is observed that density varies little for the temperatures associated with system operating conditions. It can thus be assumed that:

$$1 < \frac{\rho_\mathrm{in}^\mathrm{air}}{\rho_\mathrm{m}^\mathrm{air}} < \frac{\rho_\mathrm{in}^\mathrm{air}}{\rho_\mathrm{out}^\mathrm{air}} \approx 1 \tag{3.46}$$

allowing for simplification of the expression in Equation (3.42):

$$\Delta P_\mathrm{air}^\mathrm{rad} = \frac{f}{4}\frac{A_\mathrm{rad}}{A_\mathrm{c}^\mathrm{min}}\frac{v_\mathrm{max}^2 \rho_\mathrm{in}^\mathrm{air}}{2} \tag{3.47}$$

Equation (C.1) shows that $A_\mathrm{rad}/4A_\mathrm{c}^\mathrm{min}$ can be rewritten as L/D_h, meaning that Equation (3.42), and (3.47), simplify to the expression for pressure drop in horizontal a channel (C.6). Figure 3.13 shows $\Delta P_\mathrm{air}^\mathrm{rad}$ as a function of $\dot{V}_\mathrm{air}$. It is concluded that the radiator air-side pressure drop is negligible.

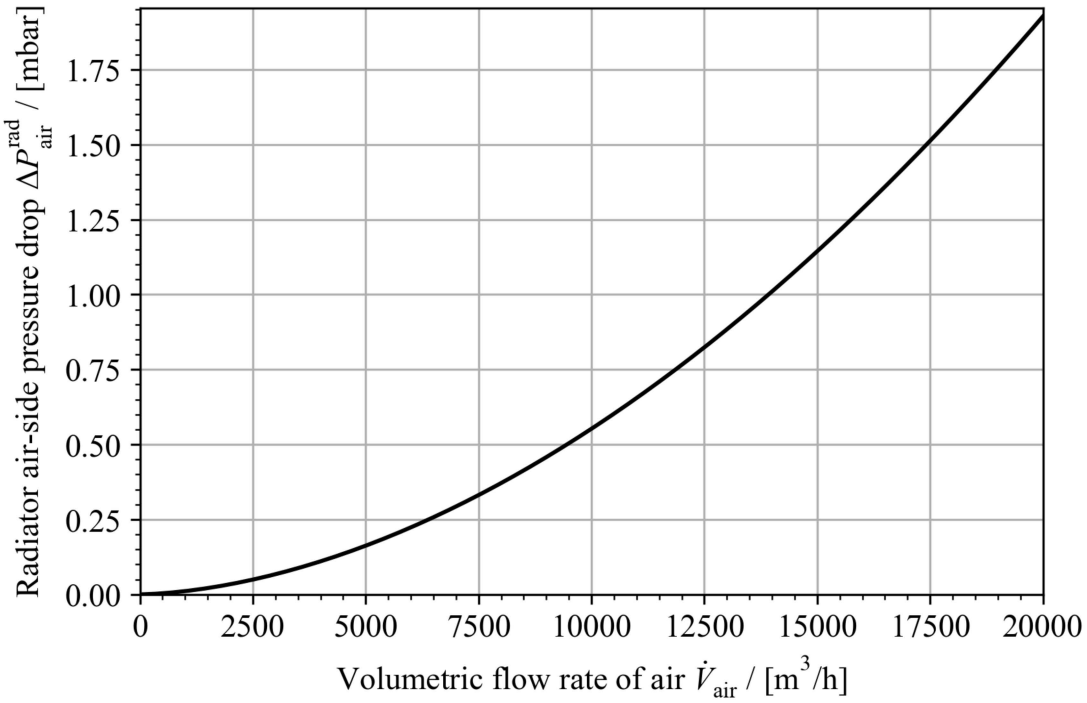

Figure 3.13: Radiator air-side pressure drop $\Delta P_{\text{air}}^{\text{rad}}$, as a function of the volumetric flow rate of air $\dot{V}_{\text{air}}$.

3.2.3.2 Tube-side Pressure Drop

The total internal pressure drop in the radiator is the sum of the pressure drop in each section of the radiator:

$$\Delta P_{\text{rad}} = \Delta P_{\text{in}}^{\text{rad}} + \Delta P_{\text{core}}^{\text{rad}} + \Delta P_{\text{out}}^{\text{rad}} \tag{3.48}$$

where $\Delta P_{\text{in}}^{\text{rad}}$, $\Delta P_{\text{out}}^{\text{rad}}$, and $\Delta P_{\text{core}}^{\text{rad}}$, represent the pressure drop along the inlet, outlet, and core of the radiator, respectively. Pressure drop due to gravitational effects is not considered, as the inlet and outlet of the radiator are at equal altitudes ($\Delta z = 0$). Figure 3.14 shows a basic illustration of the internal flow of the radiator. The aforementioned pressure drop components will be evaluated in this section.

Inlet Pressure Drop
Dividing and combining manifolds are necessary at the radiator inlet and outlet, respectively. Manifolds are discussed in Appendix C.2.5. Equation (C.12) provides a lower boundary for the hydraulic diameter of the manifold, as tube diameter and count are provided by XINTC. A circular manifold of diameter $D_{\text{mani}} = 5$ cm is initially proposed. The total pressure drop in the inlet manifold of the radiator is a function of the loss coefficients of the flow division, the abrupt flow contraction, and wall friction. Upon investigation, the inlet losses are approximately equal to that of isolated dividing T-junctions, because:

- the loss coefficient due to the contraction of the flow is negligible, as it is a stable process [69];
- from applying the methods described in Appendix C.2.2, it is concluded that wall friction losses within the manifold are negligible;

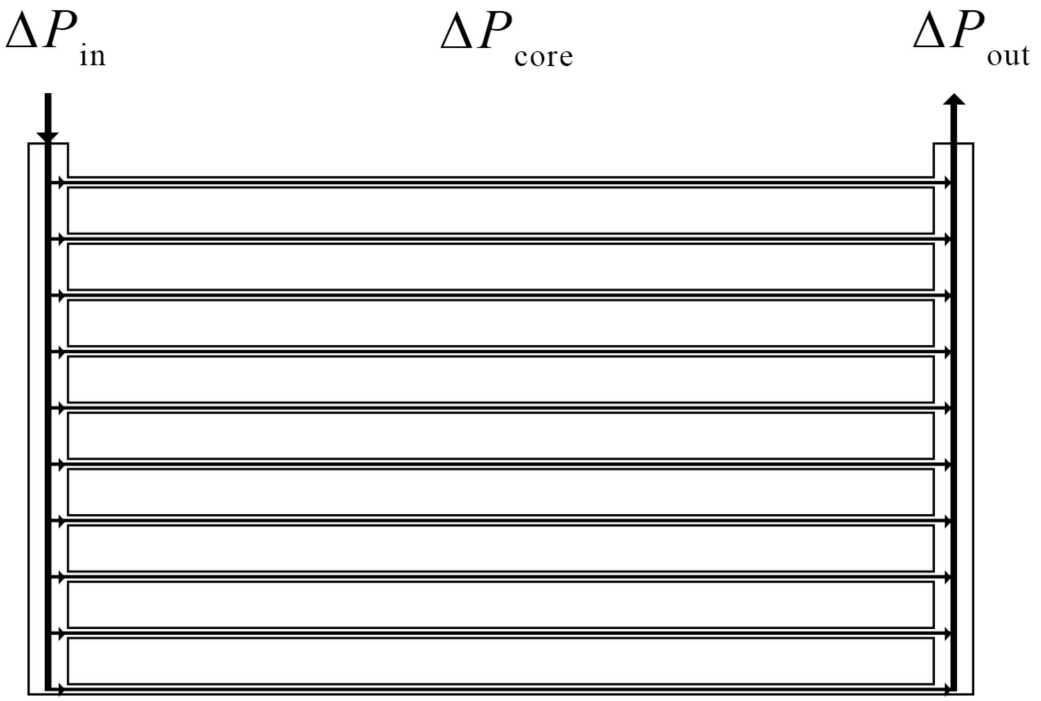

Figure 3.14: Schematic representation of liquid flow within the radiator, and its pressure drop components $\Delta P_{\text{in}}^{\text{rad}}$, $\Delta P_{\text{out}}^{\text{rad}}$, and $\Delta P_{\text{core}}^{\text{rad}}$.

- the radiator proposed in this report requires a manifold with 10 tubes, meaning that the tube flow rate is 10%; and
- the tubes are more than four tube diameter apart.

The loss coefficients of a dividing T-junction are determined through Figure C.2b. The total pressure drop within the junctions is a function of the branch loss K_{12}, and the manifold loss K_{13}. The tube flow velocity in the n-th tube (defined as $v_{12}^n = v_{\text{tube}}^n$), is initially assumed to be equal to $v_{\text{tube}}^{\text{rad}} = 2$ m/s. The manifold velocity at the n-th tube v_{13}^n, follows from conservation of mass:

$$v_{13}^n = v_{\text{mani}} - \sum_{0}^{n-1} v_{12}^n \left(\frac{D_{\text{i}}^{\text{rad}}}{D_{\text{mani}}} \right)^2, \quad n = 1, 2, 3, ..., 10 \tag{3.49}$$

with $n = 1$ the first tube with respect to the manifold inlet, and v_{mani} the flow velocity at the inlet of the manifold; initially assumed to be:

$$v_{\text{mani}} = n_{\text{tube}} v_{\text{tube}}^{\text{rad}} \left(\frac{D_{\text{i}}^{\text{rad}}}{D_{\text{mani}}} \right)^2 \tag{3.50}$$

To determine the value of the pressure drop at the n-th junction ΔP_{in}^n, Equation (C.4) is modified, to weigh each loss coefficient to its respective flow velocity:

$$\Delta P_{\text{in}}^n = \frac{\rho_{\text{EL}}}{2} \left[K_{12}^n (v_{12}^n)^2 + K_{13}^n (v_{13}^n)^2 \right], \quad n = 1, 2, 3, ..., 10 \tag{3.51}$$

Outlet pressure drop
The total pressure drop in the outlet manifold is a function of the loss coefficients of flow division,

abrupt flow expansion, and wall friction. Similar to the inlet manifold, wall friction losses are negligible, and manifold losses are approximately the combining losses in a T-junction; determined through Figure C.2a. K_{exp} should be considered, as Figure C.2a does not account for a variation in cross-sectional area. The value of K_{exp} is determined through Equation (C.11). The branch velocity is denoted by $v_{23} = v^n_{tube}$. The manifold flow velocity v_{13}, follows from Equation (3.49). Following the same methodology as described for the inlet manifold, the pressure drop at the n-th junction of the outlet manifold ΔP^n_{out}, is:

$$\Delta P^n_{\text{out}} = \frac{\rho_{\text{EL}}}{2}\left[(K^n_{23} + K_{\text{exp}})(v^n_{23})^2 + K^n_{13}(v^n_{13})^2\right], \quad n = 1, 2, 3, ..., 10 \tag{3.52}$$

Pressure drop in the radiator core

Pressure drop in the core $\Delta P^{\text{rad}}_{\text{core}}$ is determined through the methods described in Appendix C. The core of the radiator consists of drawn stainless steel tubing (surface roughness equal to $\epsilon = 1.5$ μm [70, 71]), with a total of 10 parallel tube rows. Pressure drop along parallel channels is typically equalized, i.e. the core pressure drop is equal to that of a single channel [69]. Each tube row contains 8 passes, and 7 turns. The total hydraulic losses within the radiator core consist of frictional and turn losses. Frictional losses depend on the friction loss coefficient K_{fr}, and in turn the friction factor f_{fr}; both detailed in Appendix C.2.2. Turn losses depend on the turn loss coefficient K_{turn}, detailed in Appendix C.2.3. Following the general expression for pressure drop in a channel, Equation (C.4), the radiator core pressure drop in the n-th tube is described by:

$$\Delta P^n_{\text{core}} = (K_{\text{fr}} + K_{\text{turn}} \cdot n_{\text{turn}}) \frac{\rho_{\text{EL}} v^n_{\text{tube}}}{2}, \quad n = 1, 2, 3, ..., 10 \tag{3.53}$$

with $n_{\text{turn}} = 7$, the number of tube turns. The tube turns are considered perfect half circles, where turn radius r_{t}, depends on the transverse and longitudinal tube pitch:

$$r_{\text{t}} = \frac{1}{2}\sqrt{P^2_{\text{T}} + P^2_{\text{L}}} \tag{3.54}$$

The value of the turn loss coefficient follows from table C.2, and is $K_{\text{turn}} = 0.48$ [61]. The friction factor within the radiator tubes is determined through Equation (C.9), provided by Churchill [72]. Following Equation (C.10), the friction loss factor is:

$$K_{\text{fr}} = f_{\text{fr}} \frac{L_{\text{rad}} \cdot n_{\text{pass}}}{D^{\text{rad}}_{\text{i}}} \tag{3.55}$$

The pressure drop in the radiator core can be determined through Equation (3.53), and Figure 3.15 shows $\Delta P^{\text{n}}_{\text{core}}$ as a function v_{tube}.

Overall pressure drop

The relations suggested in this section can be used to determine the overall pressure drop in the n-th tube of the radiator. The flow speeds within the tubes typically vary to equalize the tube-side pressure drop [69], i.e.:

$$\Delta P_{\text{rad}} = \Delta P^n_{\text{rad}} = \Delta P^n_{\text{in}} + \Delta P^n_{\text{core}} + \Delta P^n_{\text{out}}, \quad n = 1, 2, 3, ..., 10 \tag{3.56}$$

To determine the flow distribution along the manifold tubes, and the true value of ΔP_{rad}, an iterative approach is required. An initial guess of $v_{12} = v_{\text{tube}} = 2$ is applied to all tubes. Table 3.1 shows the corresponding values for all pressure drop components and the total pressure drop across the radiator, as in accordance with Equation (3.56). After an iterative process, the velocity distribution is determined, and the final value for the total internal radiator pressure drop $\Delta P_{\text{rad}} =$ 234 mbar is calculated. The data corresponding to this value are shown in Table 3.2.

From the values determined in this section, it is concluded that the core pressure drop dominates the pressure drop along the radiator. The pressure drop through the radiator can be accounted

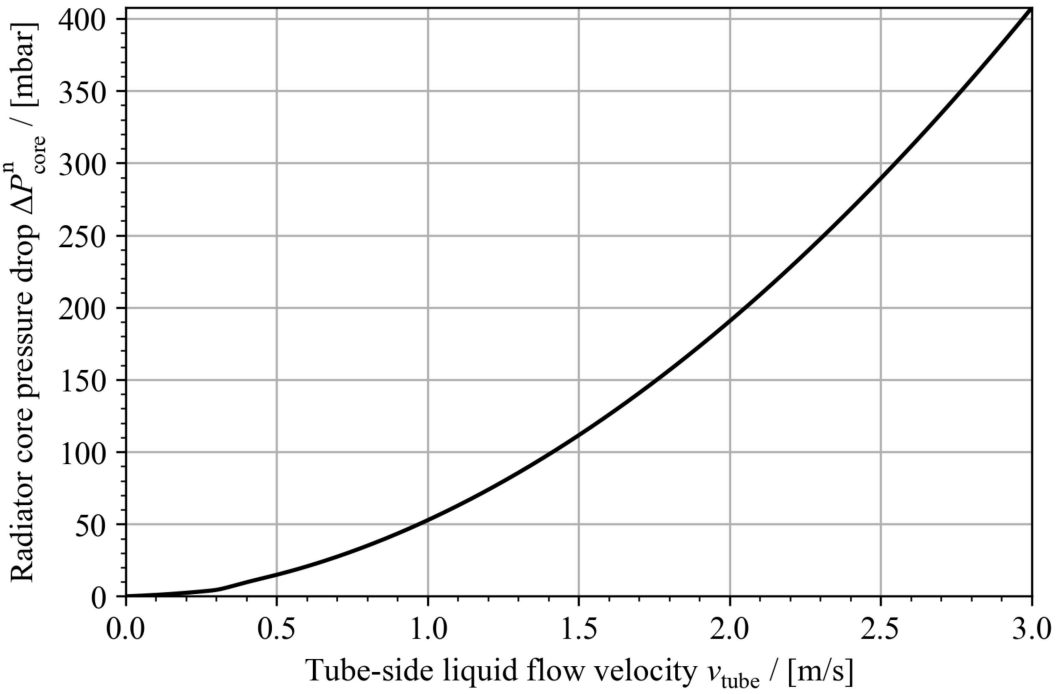

Figure 3.15: Radiator core pressure drop ΔP^{n}_{core}, as a function of tube-side liquid flow velocity v_{tube}.

for by the liquid pumps, and the internal pressure poses no structural risk for the stainless steel tubing. The flow is well distributed and is not considered a hindrance to radiator performance. Varying D_{mani} does not significantly affect the pressure drop for values $D_{mani} > 3.2$ cm. A manifold diameter of $D_{mani} = 5$ cm is recommended, as this will be beneficial later in this work. It is recommended the maximum tube-side flow velocity is set to $v_{tube} = 2$ m/s, as pressure drop is considered manageable, and increasing v_{tube} further does not increase radiator performance significantly (see Figure 3.12). It is concluded that the value of ΔP_{rad} is within 500 mbar limit set by the PED [24].

Table 3.1: Values of pressure drop components within the radiator for tube flow velocity $v_{12} = v_{23} = 2$ m/s. Total pressure drop is the sum of inlet, outlet, and core pressure drop $\Delta P_{\text{in}}^{\text{rad}}$, $\Delta P_{\text{out}}^{\text{rad}}$, and $\Delta P_{\text{core}}^{\text{rad}}$, respectively. The volumetric flow rate fraction is based on v_{12} and the manifold flow velocity v_{13}. Value of loss coefficients K, follow from Figure C.2, and are based on the volumetric flow rate fraction.

				Inlet			**Outlet**			**Core**	**Total**
n	v_{12}, v_{23}/ [m/s]	v_{13}/ [m/s]	$\dot{V}_2/\dot{V}_1$, $\dot{V}_2/\dot{V}_3$	K_{12}	K_{13}	$\Delta P_{\text{in}}^{\text{rad}}$/ [mbar]	K_{23}	K_{13}	$\Delta P_{\text{out}}^{\text{rad}}$/ [mbar]	$\Delta P_{\text{core}}^{\text{rad}}$/ [mbar]	ΔP_{rad}/ [mbar]
1	2.00	0.968	0.10	0.9	0	24.4	-0.5	0.2	12.2	191	227
2	2.00	0.871	0.11	0.9	0	24.4	-0.5	0.2	12.0	191	227
3	2.00	0.774	0.13	0.9	0	24.4	-0.4	0.2	14.5	191	229
4	2.00	0.678	0.14	0.9	0	24.4	-0.4	0.2	14.3	191	229
5	2.00	0.581	0.17	0.9	0	24.4	-0.3	0.2	16.8	191	232
6	2.00	0.484	0.20	0.9	0	24.4	-0.2	0.3	19.6	191	234
7	2.00	0.387	0.25	0.9	0	24.4	-0.1	0.3	22.1	191	237
8	2.00	0.29	0.33	0.85	0	23.0	0.1	0.4	27.4	191	241
9	2.00	0.194	0.50	0.9	0	24.4	0.4	0.5	35.5	191	250
10	2.00	0.097	1	1.3	0.3	35.2	0.5	1.1	38.1	191	264

Table 3.2: Values of pressure drop components within the radiator. Total pressure drop ΔP_{rad} normalized through iterative variation of tube flow velocity $v_{12} = v_{23}$. Total pressure drop is the sum of inlet, outlet, and core pressure drop $\Delta P_{\text{in}}^{\text{rad}}$, $\Delta P_{\text{out}}^{\text{rad}}$, and $\Delta P_{\text{core}}^{\text{rad}}$, respectively. The volumetric flow rate fraction is based on v_{12} and the manifold flow velocity v_{13}. Value of loss coefficients K, follow from Figure C.2, and are based on the volumetric flow rate fraction.

				Inlet			**Outlet**			**Core**	**Total**
n	v_{12}, v_{23}/ [m/s]	v_{13}/ [m/s]	$\dot{V}_2/\dot{V}_1$, $\dot{V}_2/\dot{V}_3$	K_{12}	K_{13}	ΔP_{in}/ [mbar]	K_{23}	K_{13}	ΔP_{out}/ [mbar]	ΔP_{core}/ [mbar]	ΔP_{rad}/ [mbar]
1	2.03	0.968	0.09	0.9	0	25.1	-0.5	0.2	12.6	196	234
2	2.03	0.871	0.10	0.9	0	25.2	-0.5	0.2	12.4	197	234
3	2.02	0.774	0.11	0.9	0	24.8	-0.4	0.2	14.7	194	234
4	2.02	0.678	0.13	0.9	0	24.8	-0.4	0.2	14.6	194	234
5	2.01	0.581	0.15	0.9	0	24.6	-0.3	0.2	17.0	192	234
6	2.00	0.484	0.20	0.9	0	24.4	-0.2	0.3	19.5	191	234
7	1.985	0.387	0.25	0.9	0	24.0	-0.1	0.3	21.8	188	234
8	1.97	0.29	0.34	0.85	0	22.3	0.1	0.4	26.6	185	234
9	1.93	0.194	0.50	0.9	0	22.7	0.4	0.5	33.0	178	234
10	1.877	0.097	1.00	1.3	0.3	31.0	0.5	1.1	33.6	169	234

3.3 The Flow Panels

Every module contains two inputs and two outputs, resulting in a large number of channels per section. The main function of the flow panel is to reduce the installation and maintenance complexity of the section. The flow panel is a novel component that is, in essence, a large panel with embedded flow channels. Figure 3.16 shows the general principle of the flow panel functionality within the section. In this section, the general design architecture of the flow panel will be discussed. Hydrodynamic and thermal behaviour will be assessed, a detailed material selection procedure is performed, and methods of in-house manufacturing will be discussed. The complex shape of the proposed flow panel design results in a conductive heat transfer coefficient that is difficult to determine analytically. Therefore, the heat flux of the flow panels will not be discussed, and is instead recommended for future work.

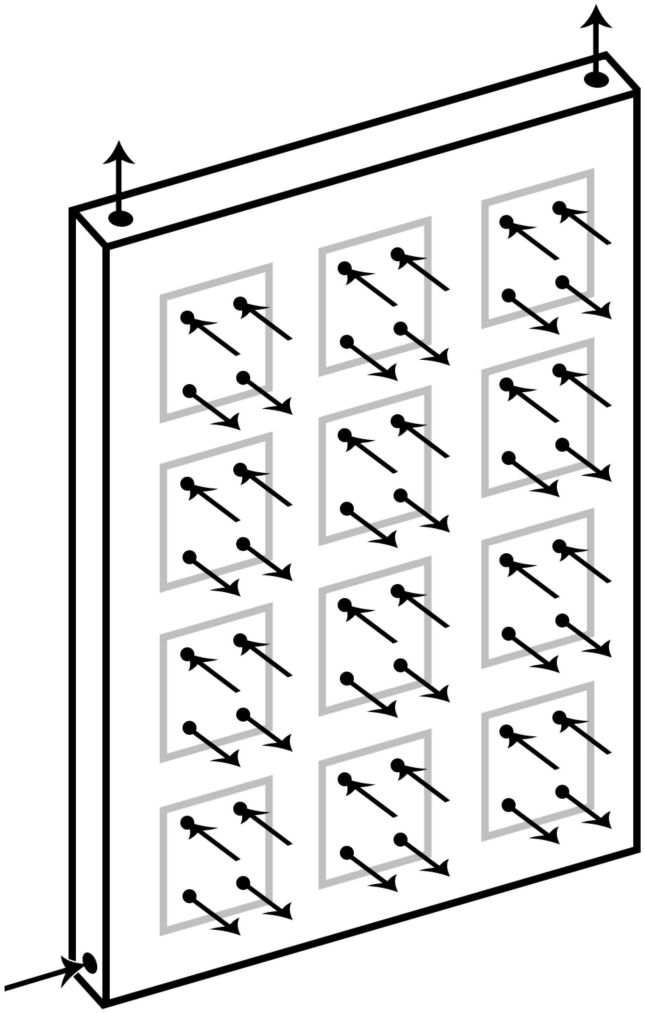

Figure 3.16: Illustration of the general principle of flow panel functionality. Liquid electrolyte flow enters at the bottom of the panel to be distributed across modules. Grey squares indicate module positions. Arrows on the face of the panel indicate the flow entering and leaving the modules. Finally, the gas-liquid product exits at the top of the flow panel and travels to the separators.

3.3.1 Design and Manufacturing Method

The flow panel should be designed with a suitable manufacturing method in mind due to its large size and complex shape. A limited number of manufacturing methods are suitable for the manufacturing process [23]. It is recommended to divide the flow panel load over multiple smaller flow panels, as it offers a number of advantages. First, weight and size reduction increases manufacturability. Second, driving down costs through to the economy of numbers. Third, it offers advantages in transport, handling and installation. The flow panels should span the height of a module column, as in each column the modules utilize the same channels within the flow panel. Flow panels that span the width of a single module column are recommended, as they offer the greatest advantage in the economy of numbers.

Two-channel configurations of the flow panels are discussed. First, a simple design consisting of straight channels, as shown in Figure 3.17a, is considered. The simple design contains straight channels that allow for a multitude of manufacturing methods. These manufacturing methods include: extrusion; polymer resin casting; thermoforming; reaction, gas-assisted, and structural foam injection moulding; and CNC-machining. The aforementioned manufacturing methods are detailed in Appendix D.1. With the exception of extrusion and CNC-machining, the methods mentioned are single-step processes, i.e., the component is manufactured without requiring additional process steps. Both extrusion and CNC-machining require additional joining processes that introduce a risk of internal and external leakage; making single-step manufacturing methods much preferred. However, the simple design requires the module inputs and output channels to be located at different points along the face plane. This difference can be seen clearly when comparing the simple design shown in Figure 3.17a, to a branched design shown in Figure 3.17b. The architecture of the modules does not allow for the implementation of the simple design. The module inputs and outputs are positioned such that current losses are minimized. Instead, an alternative design is proposed. The branched design, as shown in Figure 3.17b, is based on optimal module channel position. Although favourable towards module architecture, this configuration does not allow for single-step manufacturing methods. The complexity introduced by the branching of channels makes extrusion, thermoforming, moulding and casting processes inapplicable. Instead, the flow panels should be manufactured through CNC-machining. This implies that the flow panels are to be manufactured in two parts that are joined together. Joining methods remain undisclosed.

3.3.2 Material Selection

The material of the flow panel should offer high chemical resistance to KOH, low electrical conductivity, and sufficient structural strength to be handled. Polymer plastics offer the aforementioned properties. Some of the subjects covered in this section are discussed in more detail in Appendix D. It is explicitly mentioned when Appendix D is consulted. The large amount of commercially available polymers, and their many varieties, make polymer selection a challenging process. It should be noted that there is seldom a perfect solution to the polymer selection process [73]. In this work, only bulk materials are considered, and commodity plastics are preferred. Fibre-reinforced polymers are not considered, as they are typically only advantageous for high-performance applications [74]. A computer-assisted material selection is performed; utilizing the ANSYS eduPack software [23]. The criteria set for polymer primary selection are as follows:

- Price per unit volume €/m^3: the ANSYS eduPack database has over 900 polymer entries. A cut-off is made at polymers that cost over 3000 €/m^3. Price per unit volume is preferred over price per unit mass, as the flow panel size is constant.

- Glass transition temperature: the temperature at which a polymer moves from the glassy regime to the rubbery regime. The rubbery regime is typically associated with lower Young's modulus. Young's modulus and its impact on the flow panel are covered in section 3.3.2.1. Little reduction in Young's modulus is seen for temperature variations below the glass transition temperature. However, especially semi-crystalline and amorphous polymers show a

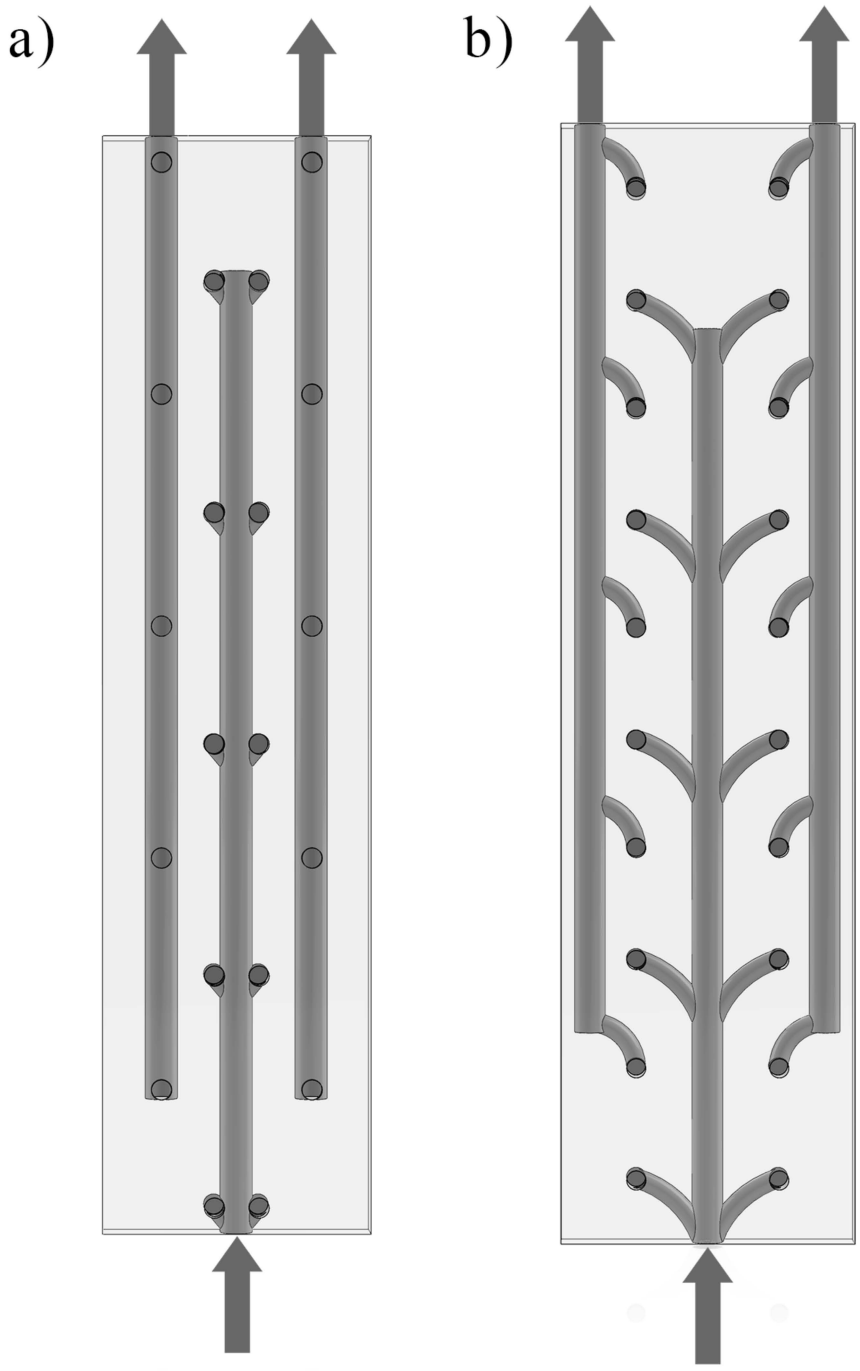

Figure 3.17: Two possible flow panel designs: a) simple design with straight channels, allowing for great manufacturability; b) branched design based on optimal module input and output positioning.

rapid decrease in Young's modulus after the glass transition temperature. A material that is in the glassy regime should be selected, as these provide a relatively high and stable Young's modulus [75].

- Maximum service temperature: the temperature at which a material can be loaded for an extended duration; without encountering notable issues (e.g., excessive creep, strength deterioration, chemical alteration, and oxidation). To ensure durability of the product, the maximum service temperature of the material should be above the maximum operating temperature of the system.
- Electrical conductivity: a material property that measures the ability of a material to conduct electric current. A low electrical conductivity is crucial to safely transport the electrically charged electrolyte.
- Chemical resistance: high chemical resistance to KOH is crucial to prevent material deterioration.

The following polymers meet the proposed criteria:

- Acrylonitrile Butadiene Styrene (ABS)
- Acrylonitrile Styrene Acrylate (ASA)
- Methyl Methacrylate Acrylonitrile Butadiene Styrene (MABS)
- Polyethylene Terephthalate (PET)
- Polymethyl Methacrylate (PMMA)
- Styrene Acrylonitrile (SAN)
- Polyvinyl Chloride (PVC)
- Polystyrene (PS)

A further selection is conducted by reviewing Young's modulus, toughness, permeability, and connectivity. Figure 3.18 lays out the aforementioned material properties.

3.3.2.1 Young's Modulus and Toughness

Young's modulus is a measure of the stiffness or rigidity of a material. It represents the ratio of stress to strain within the material under linear deformation. A high Young's modulus should be preferred, as it minimizes the amount of deformation in the flow panel under its own weight. Figure 3.18a shows Young's moduli of the polymer selection per unit volumetric cost. ASA, MABS, and PS are not further considered due to their relatively low Young's modulus.

3.3.2.2 Toughness

Toughness is a material property that represents its ability to absorb energy and resist fracture under the application of external forces. A low material toughness indicates a more brittle material. Material toughness should not be too low to ensure the flow panel does not get damaged during transport, handling, and installation, Figure 3.18b shows the toughness of the material selection per unit volumetric cost. ABS, SAN, and PMMA are not further considered due to their relatively low toughness.

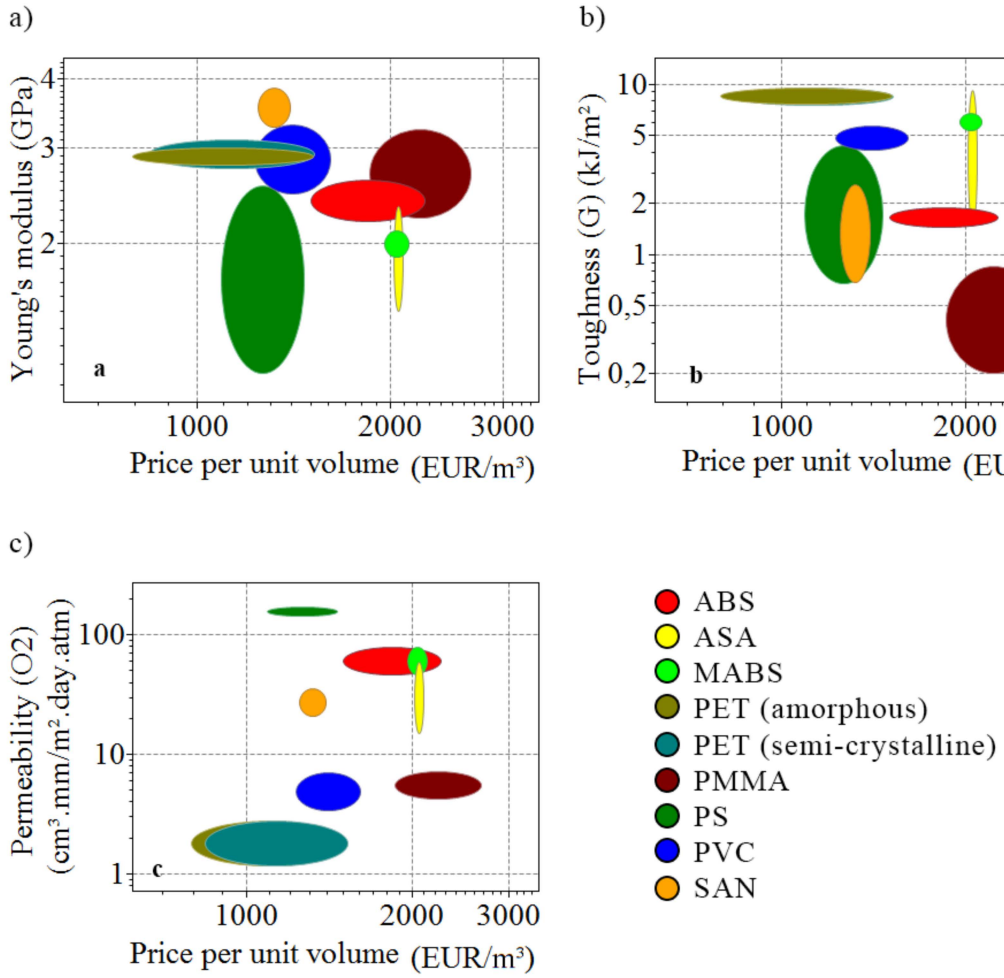

Figure 3.18: Material properties of primarily selected plastics: a) Young's modulus [GPa], b) toughness [kJ/m^2], c) permeability of oxygen [cm^3·mm/m^2·day·atm]. All properties are displayed per price per unit volume [€/m^3]. Image used courtesy of ANSYS, Inc. [23].

3.3.2.3 Connectivity

Connectivity is the decisive factor for material selection. Most industry piping is manufactured from PVC [62]. The joining of PVC to other PVC components can be achieved with PVC adhesive. The PVC adhesive chemically bonds the two PVC surfaces, creating a strong and durable joint. When applied correctly the adhesive forms a tight seal; reducing the likelihood of leaks. Connecting a PET flow panel to PVC tubing is less successful, as the difference in the chemical composition of the two materials makes adhesives less effective. It is concluded that PVC is the most suitable material for the flow panels. Specifically, unplasticized PVC (uPVC) is to be utilized for the flow panel. uPVC offers greater strength properties, at the cost of less flexibility when compared to its plasticized counterparts [23].

3.3.2.4 Permeability

Permeability is a material property that describes the degree to which a fluid, referred to as permeate, is capable of penetrating a solid material. It is typically utilized to determine the volumetric flux J_i [$\mathrm{m}^3 \cdot \mathrm{m}^{-2}\mathrm{s}^{-1}$], of a fluid through a solid. It is in accordance with Fick's first law of diffusion:

$$J_i = -D_i \frac{\mathrm{d}c_i}{\mathrm{d}x} \tag{3.57}$$

where D_i [m^2/s] is the diffusion coefficient of component i in the solid material; c_i [$\mathrm{m}_i^3/\mathrm{m}^3$] the concentration of component i in the material and x [m] the distance to the feed. Integration of Fick's first law results in a steady state expression for J_i:

$$J_i = -D_i \frac{c_{i_\mathrm{P}} - c_{i_\mathrm{F}}}{\delta} \tag{3.58}$$

with δ [m] the thickness of the solid material; and c_{i_F}, and c_{i_P} the concentration of component i in the feed, and permeate respectively. The concentration profile of component i within the solid material can be described with Henry's law:

$$c_i = S_i p_i \tag{3.59}$$

where p_i [Pa] is the partial pressure of component i, and S_i [$\mathrm{m}_\mathrm{i}^3 \cdot \mathrm{m}^{-3}\mathrm{Pa}^{-1}$] the solubility coefficient. Combining Equations (3.58), and (3.59) results in:

$$J_i = -P_i \frac{p_{i_\mathrm{P}} - p_{i_\mathrm{F}}}{\delta} \tag{3.60}$$

providing the definition of a materials' permeability to component i, P_i:

$$P_i \equiv D_i S_i \quad \left[\frac{\mathrm{m}^3\mathrm{m}}{\mathrm{m}^2\mathrm{sPa}}\right] \tag{3.61}$$

The ANSYS eduPack software [23] provides values for the oxygen permeability of polymers, which is shown per unit volumetric cost in Figure 3.18c. It can be seen that PVC has low oxygen permeability. The hydrogen permeability of PVC is not mentioned in eduPack, but literature suggests that it is also relatively low [76]. Equation (3.60) shows that J_i is dependent on the partial pressure of the permeate. Since the system operates at atmospheric pressure, the partial pressure difference for both hydrogen and oxygen is approximately 1 atm. The resulting value of the permeate flow rate through the flow channel is considered:

$$\dot{V}_i = J_i A_i \tag{3.62}$$

The permeate flow rate is the largest for permeation between the hydrogen channel and the environment. In this scenario, the partial pressure difference is maximized, and the wall thickness is minimized; resulting in the largest value for J_i, in accordance with Equation 3.60. After evaluation, it is observed that $\dot{V}_{\mathrm{H}_2}$ is in the order of mm^3/day. It is concluded that the effects of permeation within the system are negligible at maximum, and deemed insignificant in any uPVC component.

3.3.3 Hydrodynamics

In essence, the flow panel channels behave as vertical manifolds. The theory behind manifolds is discussed in Appendix C.2.5. The approach taken in this section is similar to that of the inlet and outlet manifolds of the radiator (see section 3.2.3.2), and will therefore be covered in less detail. The inlet manifold of the flow panel contains the liquid electrolyte stream travelling towards module inlets. The outlet manifold of the flow panel contains the gas-liquid flow collected from the module outlets. The total pressure drop over the flow panel is the sum of the pressure drop along the inlet and outlet manifolds, $\Delta P_{in}^{\mathrm{FP}}$ and $\Delta P_{in}^{\mathrm{FP}}$, respectively. Gravitational effects are not considered, as the flow panel is in the same flow loop as the liquid downcomer.

$$\Delta P_{\mathrm{FP}} = \Delta P_{in}^{\mathrm{FP}} + \Delta P_{\mathrm{out}}^{\mathrm{FP}} + \rho_{\mathrm{EL}} g \Delta z \tag{3.63}$$

3.3.3.1 Outlet Manifold: Two-phase Flow

The pressure drop in a gas-liquid flow can be determined through similar methods as a mono-phase flow [77]. The general expression for pressure drop, Equation (C.4), applies. The Reynolds number of the two-phase mixture Re_{M}, is required to determine the friction coefficient, and thus the loss coefficient of a two-phase flow. Michaelides, et al [77], provided an alternative definition of Re_{M} for gas-liquid mixtures:

$$Re_{\mathrm{M}} = \frac{\dot{m} L_{\mathrm{c}}}{A_{\mathrm{c}} \mu_{\mathrm{M}}} \tag{3.64}$$

The dynamic viscosity of the mixture μ_{M}, is determined through the model provided by McAdams, et al. [78]:

$$\mu_{\mathrm{M}} = \left(\frac{x}{\mu_{\mathrm{G}}} + \frac{1-x}{\mu_{\mathrm{L}}} \right)^{-1} \tag{3.65}$$

with x the two-phase flow quality; defined as the fraction of the mass of gas m_{G} to the total mass of the mixture m_{M}:

$$x \equiv \frac{m_{\mathrm{G}}}{m_{\mathrm{M}}} = \frac{\dot{m}_{\mathrm{G}}}{\dot{m}_{\mathrm{M}}} \tag{3.66}$$

Although the vertical channel of the flow panel is in the same flow loop as the liquid downcomer, the gravitational pressure drop is initially considered. The gravitational pressure drop for a gas-liquid flow differs from that of a mono-phase flow [77]:

$$\Delta P_{\mathrm{M}}^{\mathrm{g}} = (\lambda_{\mathrm{G}} \rho_{\mathrm{G}} + (1-\lambda_{\mathrm{G}}) \rho_{\mathrm{L}}) \cdot g \Delta z \tag{3.67}$$

with λ_{G} the gas volumetric flow fraction; defined as the fraction of the volumetric flow rate of gas $\dot{V}_{\mathrm{G}}$, to the total volumetric flow rate of the mixture $\dot{V}_{\mathrm{M}}$:

$$\lambda_{\mathrm{G}} \equiv \frac{\dot{V}_{\mathrm{G}}}{\dot{V}_{\mathrm{M}}} \tag{3.68}$$

It is observed that $x \approx 0$, and $(1-\lambda_{\mathrm{G}})\rho_{\mathrm{L}} \gg \lambda_{\mathrm{G}} \rho_{\mathrm{G}}$, for both the hydrogen and oxygen in their respective flow panel channels. As a result, $\mu_{\mathrm{M}} = \mu_{\mathrm{L}}$, and $\Delta P_{\mathrm{M}}^{\mathrm{g}} = \Delta P_{\mathrm{L}}^{\mathrm{g}}$. It is concluded that the pressure losses of the gas-liquid flow within the flow panel behave similarly to that of a mono-phase electrolyte flow.

3.3.3.2 Flow Panel Pressure Drop

The total pressure drop in the inlet and outlet manifolds is the sum of the pressure loss due to wall friction $\Delta P_{\mathrm{fr}}^{\mathrm{FP}}$, the inlet manifold $\Delta P_{\mathrm{in}}^{\mathrm{FP}}$, and the outlet manifold $\Delta P_{\mathrm{out}}^{\mathrm{FP}}$:

$$\Delta P_{in}^{\mathrm{FP}} = \Delta P_{\mathrm{fr}}^{\mathrm{FP}} + \Delta P_{\mathrm{in}}^{\mathrm{FP}} + \Delta P_{\mathrm{out}}^{\mathrm{FP}} \tag{3.69}$$

In contrast to the radiator, the manufacturing method applied to the flow panel (CNC machining), allows for easy integration of slanted junctions. A slanted junction of angle 45° is recommended to reduce pressure drop. The flow division and joining loss components are determined through the methods described in Appendix C.2.5. $\Delta P_{\mathrm{div}}^{\mathrm{FP}}$ is approximately equal to the pressure drop of isolated flow junctions, as branches are more than 5 manifold diameters apart in both flow panel manifolds [69]. The loss coefficients of dividing and joining flows K_{12}^{n}, K_{13}^{n}, and K_{23}^{n}, are sourced from the work of Miller [69].

The loss coefficient of the flow contraction from the inlet manifold to the branch is negligible [69]. The pressure drop at the n-th branch of the inlet manifold ΔP_{in}^{n}, is determined through modifying Equation (3.51), to account for a total of 5 branches:

$$\Delta P_{in}^{n} = \frac{\rho_{\mathrm{EL}}}{2} \left[K_{12}^{n} (v_{12}^{n})^2 + K_{13}^{n} (v_{13}^{n})^2 \right], \quad n = 1,2,3,4,5 \tag{3.70}$$

Expansion losses from branch to outlet manifold are accounted for. The expansion loss coefficient K_{exp} is calculated using Equation (C.11). The pressure drop at the n-th branch of the outlet manifold ΔP^n_{out}m is determined through modifying Equation (3.71), to account for a total of 5 branches:

$$\Delta P^n_{\text{out}} = \frac{\rho_{\text{EL}}}{2}\left[(K^n_{23} + K_{\text{exp}})(v^n_{23})^2 + K^n_{13}(v^n_{13})^2\right], \quad n = 1, 2, 3, 4, 5 \tag{3.71}$$

The wall friction component is determined through the methods described in Appendix C.2.2. Equation (C.9), provided by Churchill [72], is used to determine the value of the friction coefficient. The value of f_{fr} depends on the flow velocity within the flow panel manifolds v_{13}. Since v_{13} decreases as flow is distributed across the manifold branches, a sum total of the friction loss coefficients $K^{\text{FP}}_{\text{fr}}$, is determined. From the definition of $K^{\text{FP}}_{\text{fr}}$, Equation (C.10), and the general expression for pressure drop, Equation (C.4), an expression for $\Delta P^{\text{FP}}_{\text{fr}}$ follows:

$$\Delta P^{\text{FP}}_{\text{fr}} = \frac{\rho_{\text{EL}}}{2} \cdot \frac{H_{\text{FP}}}{5D^{\text{FP}}_{\text{mani}}} \sum_{n=1}^{5} f^n_{\text{fr}}(v^n_{13})^2 = 1.38 \text{ mbar} \tag{3.72}$$

with the diameter of the flow panel manifold $D^{\text{FP}}_{\text{mani}}$, and the height of the flow panel H_{FP}. A factor 5 is introduced to divide the flow panel manifold in 5 sections, each corresponding to their respective value for v_{13}. The flow panel pressure drop at n-th module follows from substituting Equations (3.70),(3.71), and (3.72) into Equation (3.63):

$$\Delta P^n_{\text{FP}} = P^{\text{FP}}_{\text{fr}} + \Delta P^n_{in} + \Delta P^n_{\text{out}}, \quad n = 1, 2, 3, 4, 5 \tag{3.73}$$

Table 3.3 shows the values of the pressure drop components within the flow panel. The branch flow velocity is based on the maximum allowable module electrolyte flow rate ($v_{12} = v_{23} = 0.53$ m/s). Flow velocity within the manifold v_{13} follows from the mass balance. An iterative method is required to determine the value of ΔP^n_{FP}, similar to the overall pressure drop in the radiator. At the time of writing, there is no data regarding the pressure drop along the modules. The pressure drop inside the modules is likely a function of v^2, affecting the flow distribution along the manifold branches. No decisive conclusion can be drawn regarding the flow distribution along the modules. However, it can be stated that the flow panel introduces little pressure drop to the system ($\Delta P_{\text{FP}} \sim 3.7$ mbar).

Table 3.3: Values of pressure drop components within the flow panel manifolds for branch flow velocity $v_{12} = v_{23} = 0.53$ m/s. Total pressure drop is the sum of inlet and outlet pressure drop $\Delta P^{\text{n}}_{\text{in}}$ and $\Delta P^{\text{n}}_{\text{out}}$, respectively. The volumetric flow rate fractions are based on v_{12} and the manifold flow velocity v_{13}. Value of loss coefficients K, follow from Figure C.2, and are based on the volumetric flow rate fraction.

				Inlet			**Outlet**			**Friction**	**Total**
n	v_{12}, v_{23}/ [m/s]	v_{13}/ [m/s]	$\dot{V}_2/\dot{V}_1$, $\dot{V}_2/\dot{V}_3$	K_{12}	K_{13}	$\Delta P^{\text{n}}_{\text{in}}$/ [mbar]	K_{23}	K_{13}	$\Delta P^{\text{n}}_{\text{out}}$/ [mbar]	$\Delta P^{\text{FP}}_{\text{fr}}$/ [mbar]	ΔP_{FP}/ [mbar]
1	0.53	1.178	0.2	0.7	-0.02	1.14	-0.45	0.15	1.14	1.38	3.66
2	0.53	0.942	0.25	0.6	-0.05	0.84	-0.2	0.2	1.41	1.38	3.63
3	0.53	0.707	0.33	0.55	-0.05	0.88	-0.15	0.2	0.98	1.38	3.24
4	0.53	0.471	0.5	0.45	0	0.86	0.12	0.15	1.04	1.38	3.28
5	0.53	0.236	1	0.5	0.3	1.06	0.32	-0.58	0.98	1.38	3.42

3.4 The Gas-Liquid Separators

Gas-liquid separation within the separators occurs through the inlet device, separation chamber, and coalescing elements; all of which will be discussed in this section. Figure 3.19 shows a generic overview of the separator tank implemented in the XINTC system. The separators should be placed above the flow panel and AEL modules to avoid flooding of the separators due to hydrostatic pressure. A generic horizontal separator is suggested as head space is limited in this area. The gas-liquid separation systems should be as efficient as economically feasible to prevent chemical deterioration of downstream equipment.

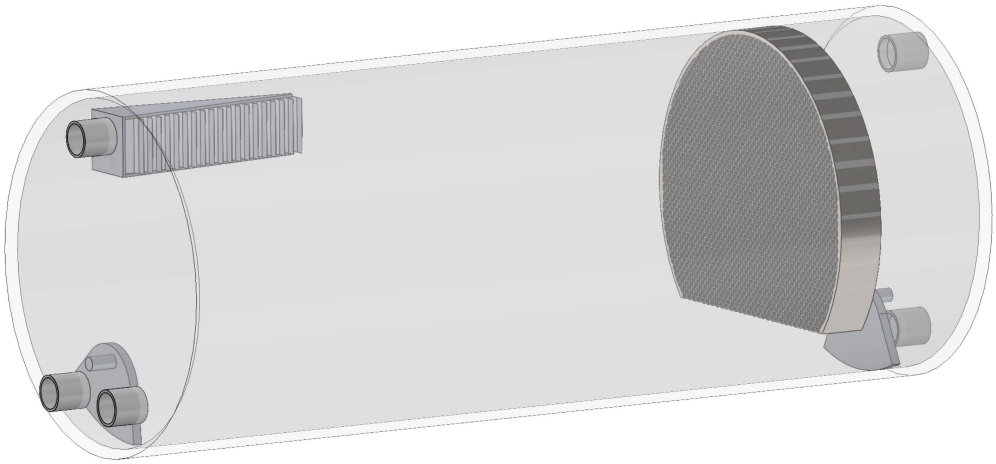

Figure 3.19: General overview of separator tank implemented in the XINTC system. Flow enters the top left, and reaches the primary separation device. Gas product travels to the right, and through a coalescing element; before exiting the separator at the top right. Inlets and outlets at the bottom facilitate liquid to and from the radiator, and to the modules via a mixer and the flow panels.

3.4.1 Material selection

The low relative pressure in the separators allows for the usage of low-cost materials. The criteria for material selection are equal to that of the flow panel; covered in detail in Section 3.3.2. The major difference in the material of the separators is that other manufacturing methods apply. However, the design of the separators is in essence that of a modified straight tube. As uPVC is already the industry standard for polymer tubing it is also the selected material for the separators [70].

3.4.2 Gravity settling

The large difference in the densities of the gas and liquid components implies that gravity separation should be effective. To achieve separation of a droplet, the residence time of the gas in the separator should exceed the time it takes for that droplet to fall from the highest point to the surface of the liquid level. The gas velocity depends on the volumetric flow rate of gas production, as well as the diameter and liquid fraction of the separator. It is assumed that the droplets are spherical in shape, and the liquid fraction is 0.5. Most engineering handbooks suggest basing the sizing of a separator on the terminal velocity v_t [70, 62, 71, 79]. However, the timespan for a spherical droplet to reach v_t, is not evident. A different approach should be explored if the time to reach v_t, is of a similar order of magnitude as the timespan of separation. To determine the time to reach v_t, the

behaviour of the falling droplets is analyzed. A force balance is proposed to determine the vertical acceleration a_z, of a droplet:

$$F_a = F_D + F_g \tag{3.74}$$

with F_a, F_D, F_g the accelerating force, drag force, and gravitational force, respectively:

$$F_D \equiv \frac{\pi}{8}\rho_g v_z^2 C_D D_{drop}^2 \tag{3.75a}$$

$$F_a \equiv ma_z \tag{3.75b}$$

$$F_g \equiv -mg \tag{3.75c}$$

Here C_D is the dimensionless drag coefficient, v_z the droplet vertical velocity, g the gravitational acceleration, ρ_g the gas density, and m the relative mass of a single droplet:

$$m = \frac{\pi}{6}D_{drop}^3(\rho_L - \rho_g) \tag{3.76}$$

with ρ_L the density of the liquid droplet. Filling in for Equation (3.74), and dividing by m results in an expression for the acceleration:

$$a_z = \frac{3C_D\rho_g}{4D_{drop}(\rho_L - \rho_g)}v_z^2 - g \tag{3.77}$$

An expression for the drag coefficient of a spherical particle can be derived from Equation (3.75a). However, this relation is dependent on the drag force F_D, and the droplet velocity v_z. In 1986, Turton and Levenspiel [80] suggested expressions for C_D as a function of the Reynolds number. They based their expression on comparing experimental data to existing correlations. However, Re is a function of the velocity itself and an iterative process is required to determine C_D for an accelerating object [71]. To avoid this, Karamanev [81] proposed an expression for C_D as a function of the Archimedes number Ar, at terminal velocity. The Archimedes number is a dimensionless number used to describe the motion of a fluid due to its relative density. It is defined as the ratio between buoyant and viscous forces:

$$Ar \equiv \frac{gD_{drop}^3(\rho_L - \rho_g)}{\mu^2} \tag{3.78}$$

The relation derived by Karamanev circumvents the velocity term. Instead, it represents C_D as a function of the driving buoyant and viscous forces. Based on 466 experimental and theoretical data points obtained from literature, Karamanev provides the following expression [81]:

$$C_D = \frac{432}{Ar}(1 + 0.0470Ar^{2/3}) + \frac{0.517}{1 + 154Ar^{-1/3}} \tag{3.79}$$

Note that as Equation (3.79) describes C_D at $v_z = v_t$, this method is not perfectly accurate. However, as the current goal is to determine the order of magnitude of the timespan required to reach terminal velocity, it is assumed to be a sufficient approximation. Figure 3.20 shows the drag coefficient of KOH droplets in both hydrogen and oxygen environments, as a function of liquid droplet diameter; based on the relation provided in Equation (3.79). With the expression for C_D, the acceleration of the droplet can be determined. A system property Z is introduced for mathematical convenience:

$$Z \equiv \frac{3C_D\rho_g}{4D_{drop}(\rho_L - \rho_g)} \tag{3.80}$$

Through the relation of acceleration and velocity, and the substitution of Z, Equation (3.77) can be written as:

$$a_z \equiv \frac{dv_z}{dt} = Zv_z^2 - g \tag{3.81}$$

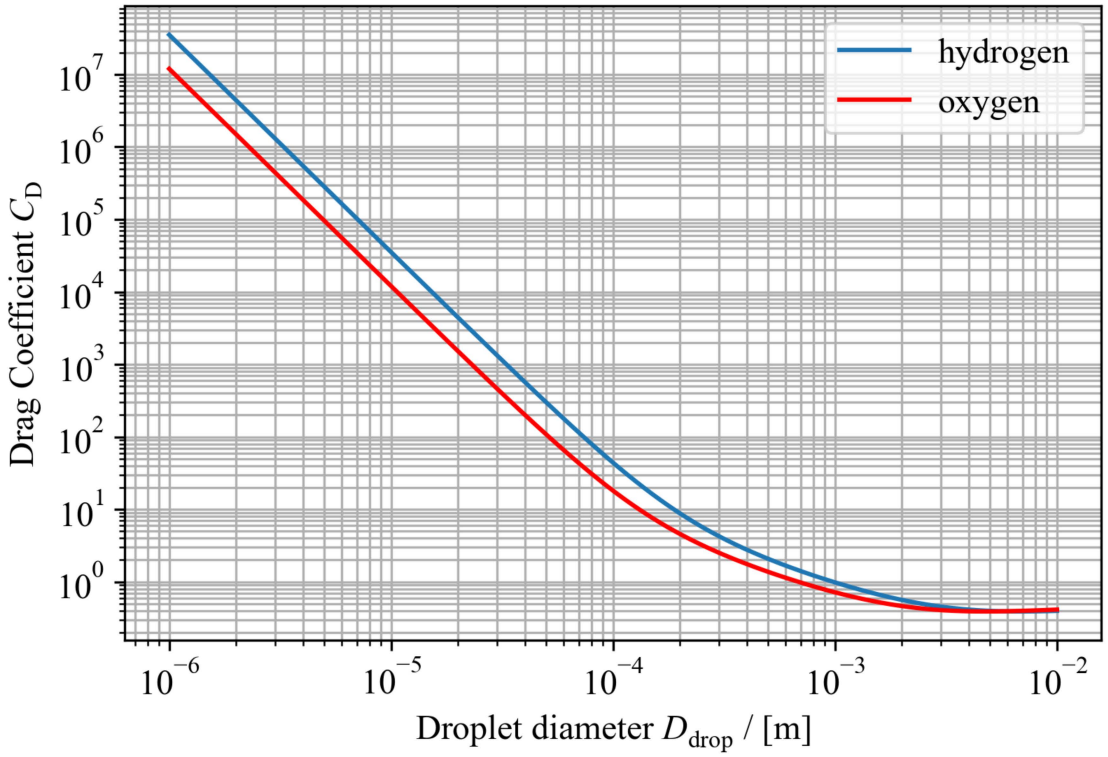

Figure 3.20: Drag coefficient C_D of KOH droplets in hydrogen and oxygen environments, as a function of droplet diameter, D_{drop}. Based on the relation provided by Karamanev [81].

Utilizing Wolfram|Alpha [82] to solve Equation (3.81), with the boundary condition $v_z(0) = 0$ yields an expression for the velocity of a droplet as a function of time t:

$$v_z(t) = \sqrt{\frac{g}{Z}} \tanh\left(t\sqrt{Zg}\right) \tag{3.82}$$

Similarly, it is possible to determine the vertical displacement $s_z(t)$, of the droplet as a function of time:

$$v_z \equiv \frac{ds_z}{dt} \tag{3.83}$$

$$s_z(t) = \frac{1}{Z} \ln\left[\cosh\left(t\sqrt{Zg}\right)\right] \tag{3.84}$$

Equations (3.82) and (3.84) provide a relation between velocity, displacement and residence time of droplets in the separators. Figure 3.21 shows the relation between velocity and time, and displacement and time of liquid KOH droplets in hydrogen and oxygen environments. It is observed that large droplets rapidly achieve high velocity and displacement; indicating that the separator performance is bottle-necked by small-diameter droplets. It is also observed that small-diameter droplets reach terminal velocity almost instantaneously. It is concluded that the assumption that droplets in the separators travel at the terminal velocity v_t, is correct. Terminal velocity is reached when $a_z = 0$, implying that the velocity of the droplet is constant. By rearranging Equation (3.77), and filling in $a_z = 0$, an expression for the terminal velocity is found:

$$v_t = \sqrt{\frac{4gD_{drop}}{3C_D} \frac{(\rho_L - \rho_g)}{\rho_g}} \tag{3.85}$$

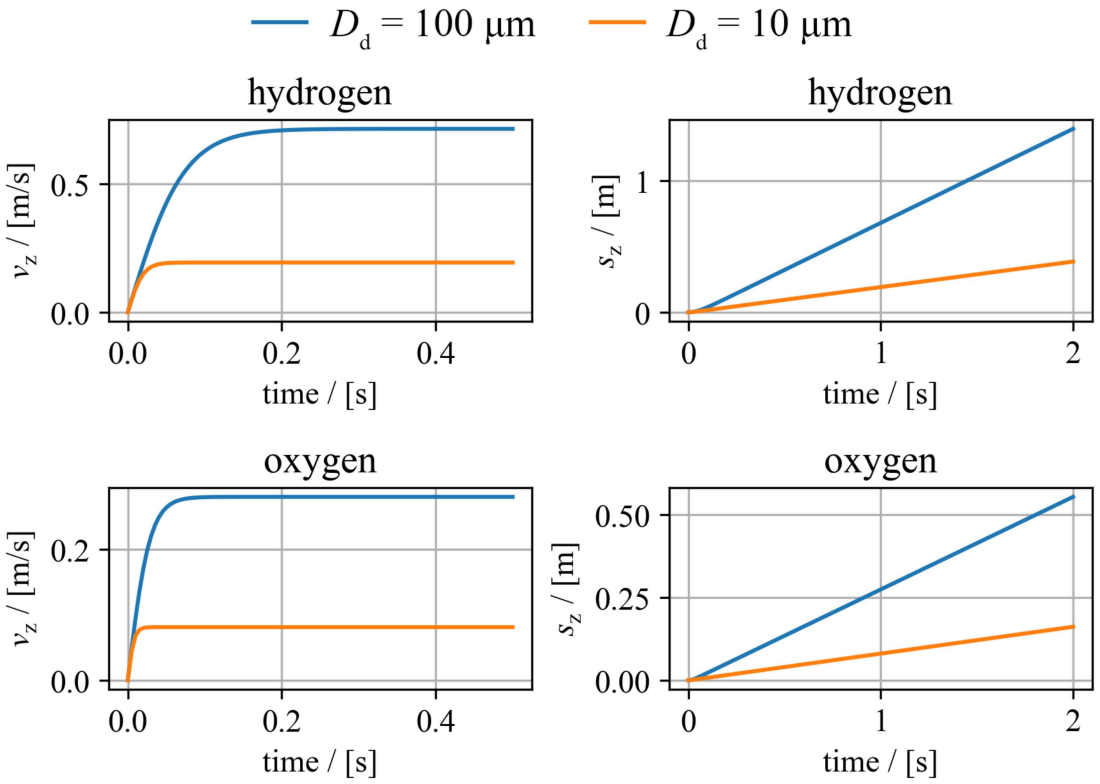

Figure 3.21: Velocity and distance of KOH droplets of various diameters D_{drop}, in a hydrogen and oxygen environment, as a function of time.

3.4.2.1 Length-to-Diameter Ratio

To achieve a desired degree of separation in a horizontal separator, the residence time of the gas phase should exceed the time it takes for the droplet to reach the liquid surface. This concept is illustrated in Figure 3.22. A relation between the length of the gravity settling section L_{set}, and separator diameter D_{sep}, is determined:

$$\frac{L_{\text{set}}}{v_{\text{g}}} > \frac{s_{\text{sag}}}{v_{\text{t}}} \tag{3.86a}$$

$$L_{\text{set}} > \frac{v_{\text{g}}}{v_{\text{t}}} s_{\text{sag}} \tag{3.86b}$$

with s_{sag} the sagitta, which in this case describes the distance from the top of the separator to the liquid level; expressed as a function of the gas volume fraction φ_{g}:

$$s_{\text{sag}} \equiv \frac{D_{\text{sep}}}{2}[1 - \cos(\pi\varphi_{\text{g}})] \tag{3.87}$$

The velocity of the gas in the separator can be determined from the volumetric flow rate of the gaseous product:

$$v_{\text{g}} = \frac{\dot{V}_{\text{g}}}{A_{\text{g}}} = \frac{4\dot{V}_{\text{g}}}{\varphi_{\text{g}} \cdot \pi D_{\text{sep}}^2} \tag{3.88}$$

Combining Equations (3.86b), (3.88), and (3.85), with the expressions of the volumetric flow rate of hydrogen and oxygen, Equations (3.4a) and (3.4b) respectively, yields an expression for the

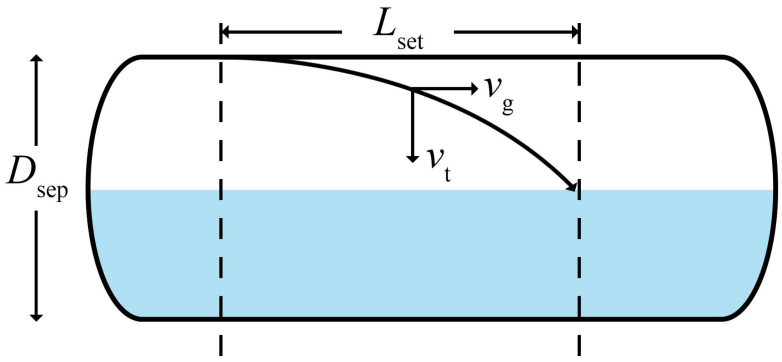

Figure 3.22: Travel path of the liquid droplet to liquid surface in the separators, assumed to be located at half the separator diameter D_{sep}. Horizontal velocity equals the gas flow velocity v_{g}, and the vertical velocity is assumed to be equal to the terminal velocity v_{t}. The length of the gravity settling section is denoted by L_{set}.

minimal settling section length of each separator:

$$L_{\text{H}_2}^{\text{set}} > n_{\text{mod}} \cdot \frac{2\rho_{\text{H}_2} M_{\text{H}_2} n_{\text{cell}} I_{\text{cell}}}{\pi F D_{\text{sep}}^2} \cdot \sqrt{\frac{3C_{\text{D}}}{gD_{\text{drop}}} \frac{\rho_{\text{H}_2}}{(\rho_{\text{L}} - \rho_{\text{H}_2})}} \cdot [1 - \cos(\pi\varphi_{\text{g}})] \tag{3.89a}$$

$$L_{\text{O}_2}^{\text{set}} > n_{\text{mod}} \cdot \frac{\rho_{\text{O}_2} M_{\text{O}_2} n_{\text{cell}} I_{\text{cell}}}{\pi F D_{\text{sep}}} \cdot \sqrt{\frac{3C_{\text{D}}}{gD_{\text{d}}^2} \frac{\rho_{\text{O}_2}}{(\rho_{\text{L}} - \rho_{\text{O}_2})}} \cdot [1 - \cos(\pi\varphi_{\text{g}})] \tag{3.89b}$$

The number of modules per section n_{mod}, is introduced to translate the gas production per module to total gas production in the section. The expressions provided in Equations (3.89a) and (3.89b), are evaluated at the maximum production capacity of the section ($I_{\text{cell}} = 27$ A). At the maximum production capacity, the aforementioned equation contains only two variables, namely φ_{g}, and D_{drop}. It is highly recommended to keep the liquid level at approximately half its diameter $\varphi_{\text{g}} = \varphi_{\text{L}} \approx 0.5$. Deviations in liquid level are much smaller at the half point, due to its cylindrical shape. Resulting in a system more resistant to perturbations. Lower and higher liquid levels increase the risk of separators draining or flooding, respectively. Assuming a gas fraction of $\varphi_{\text{g}} = 0.5$, Equations (3.89a) and (3.89b), simplify to contain only D_{drop} as a variable. Both equations are plotted as a function of D_{drop} in Figure 3.23, assuming a separator diameter of $D_{\text{sep}} = 40$ cm. It is observed that the separation performance of the separators shows diminishing returns for increasing L_{set}. Concluding remarks regarding the length of the gravity settling section will be presented in section 3.4.7.

3.4.3 Inlet device

Inlet devices, or inlet diverters, are commonly used in separator tanks to improve the separation efficiency of the system. The main purpose of an inlet device is to promote a uniform flow distribution of the feed stream, and ensure that the stream is evenly distributed across the cross-sectional area of the vessel. They also provide primary separation between the gas and liquid phases through their relative density, and thus momentum. Most inlet devices function by changing the flow direction and inducing a change in momentum. The lower-density gas possesses less momentum, and can change direction more easily. The gas can therefore flow around the diverter, disengaging the gas and liquid flows [83]. The most common types of inlet devices used in gas-liquid separators will be covered.

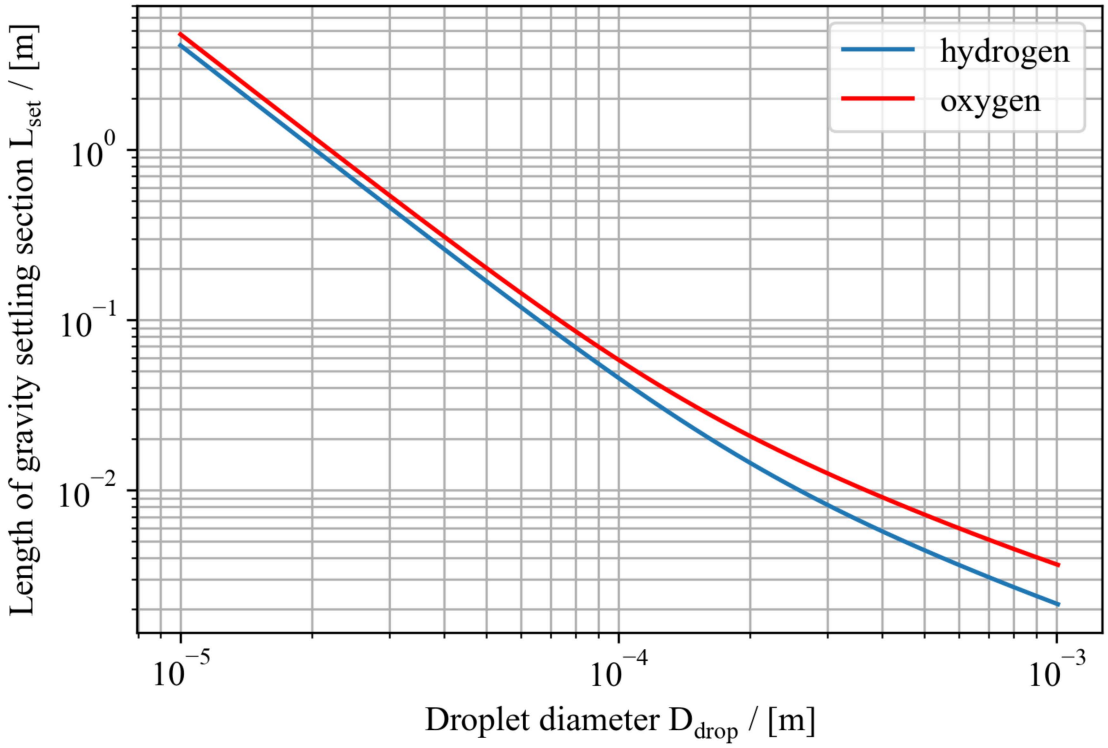

Figure 3.23: Gravity settling compartment length L_{set} as a function of droplet diameter, assuming a tank diameter of $D_{\text{sep}} = 0.4$ m, and a gas fraction of $\varphi_{\text{g}} = 0.5$.

3.4.3.1 Baffle Plate Inlet Devices

Baffle plate inlet devices consist of a flat, angled plate, or spherical dish, that is placed perpendicular to the incoming feed stream. Baffle inlet devices are the simplest type of inlet device, making them a low-cost option. However, baffle inlet devices do not perform well when inlet nozzle velocity is high [79], which is the case for this system.

3.4.3.2 Half-open Pipes Inlet Devices

Half-open inlet pipes are a popular, simple and low-cost type of inlet device. This type of inlet device consists of a pipe from which its bottom half is removed. The liquid phase falls down to the bulk, and the gaseous phase flows up and around the pipe. Half-open inlet pipes are not suited for applications with high inlet nozzle velocity is high [79].

3.4.3.3 Cyclonic Inlet Devices

Cyclonic inlets also known as centrifugal inlets, are a type of inlet device that create a cyclonic flow pattern in the feed stream, further promoting the difference in momentum between the gaseous and liquid phases. The performance of a cyclonic inlet device is rate sensitive, i.e., they are not recommended for application in a system with varying flow rates [83].

3.4.3.4 Vane-type Inlet Devices

Vane-type inlet devices are similar to baffle inlet devices. Multiple baffles are utilized to form a vane-type structure through which the mixture flows. Change in momentum through the vanes induces the separation of gas and liquid. Vane-type inlet devices perform well under high inlet velocities [79]. Variation in load is not deemed problematic, as the gravity settling section is assumed to handle any discrepancies. A widely used vane-type inlet device design is the Shell Schoepentoeter [79, 84]. The Shell Schoepentoeter (illustrated in Figure 3.24), is known for its simplicity, reliability, and low maintenance requirements. It is particularly effective in handling high gas-liquid flow rates, and in situations where the gas and liquid phases have relatively large density differences. The Shell Schoepentoeter [84] is deemed suitable for this system, and selected as the inlet device of the separator tanks. It is recommended to purchase the wire-mesh pads as off-the-shelf components, and will not be discussed in more detail. Induced pressure drop is considered negligible, as vane-type elements typically have very low pressure drop [85]. It is assumed that the inlet device does not have a significant impact on the separation performance, as it is outweighed by the gravity settling section and mist extractor.

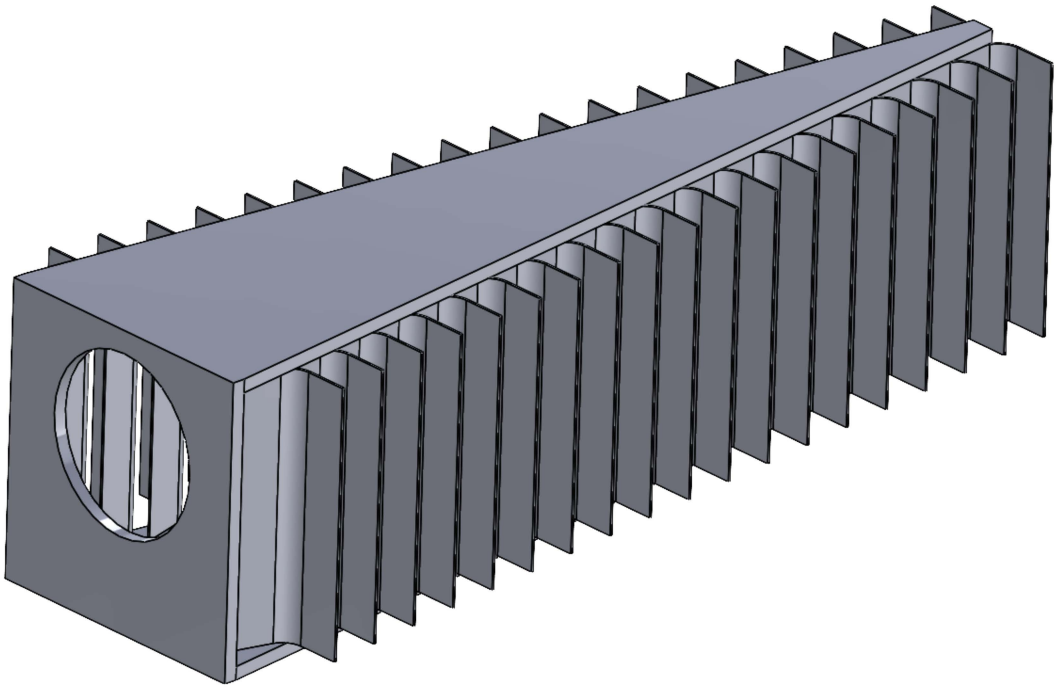

Figure 3.24: Illustration of the Shell Schoepentoeter [84] vane-type inlet device. Gas-liquid flow enters through the inlet hole displayed on the left. Flow travels through the Schoepentoeter, and exits through the vanes created by a large amount of baffles. The vanes induce a change in momentum and result in the separation of gas and liquid product.

3.4.4 Mist extractor

A mist extractor, also known as a demister, or mist eliminator, is employed in separators to increase separation performance. The most common mist extractors are that of the impingement-type [83].

Impingement-type mist extractors function by increasing droplet size through the utilization of high surface area coalescing elements. As the gas passes through the coalescing elements it undergoes multiple changes in direction. When the inertia of the entrapped droplets is too high to follow the streamline of the gas the droplet instead collides with, and impinges on, the coalescing element. Since directional changes also increase pressure drop, it can thus be assumed that the efficiency of impingement-type mist extractors is positively correlated to the pressure drop. The liquid droplets are drained into the liquid section of the separator when sufficient liquid has been collected. The most common types of mist extractors include:

1. Wire-mesh mist extractors are most common due to their good performance, low cost, and low pressure drop [86]. These units consist of a knitted pad of metal or plastic wires. Wire and pad thickness vary from 0.15 to 3.8 mm, and 100 to 300 mm, respectively [70]. A high void volume within the coalescing element allows for operation with low pressure drop. It is important that the liquid is unwetting of the wire material, as this enables impinged droplets to travel down across the wire and coalesce [79]. Liquid typically coalesces at the bottom of the pad. As the droplets grow in size the gravitational force on them increases. When the accumulated droplet becomes large enough to overcome surface tension and drag force induced by the gas flow the droplet falls to the liquid surface. Horizontal pad orientation is preferred due to the reduced distance coalesced droplets have to travel through the pad, thus reducing the risk of re-entrainment. Care must be taken that the capillary spacing within the wire-mesh pad is small enough to enable the coalescing mechanism, yet sufficiently large to prevent plugging. The pressure drop across a wire-mesh pad is typically less than 250 Pa, and thus considered negligible [70, 85]. Droplet cut-off diameter in a typical wire-mesh is approximately 5 μm [70, 85].

2. Vane-type mist extractors consist of parallel, corrugated metal or polymer baffles perpendicular to the gas steam. Typical baffle spacing ranges from 5 to 75 mm [83]. The corrugations force a change in flow streamlines, resulting in the impingement of droplets. Costs are two, to three times that of a wire-mesh mist extractor, and its pressure drop is lower [85]. The droplet cut-off diameter of vane-type mist extractors can be as low as 5 μm [70]. In contrast to wire-mesh extractors the surface of the vanes is typically wetted, allowing droplets striking the surface to be absorbed into a liquid film [79]. A vertical orientation of the coalescing elements is preferred, as this allows for convenient liquid drainage. The coalescing elements are highly resistant to plugging, due to their geometry. The efficiency of vane-type mist extractors is a function of droplet size, vane geometry, and flow speed [70]. The latter of which implies that vane-type mist extractors do not perform well under variable load.

3. Microfiber mist extractors consist of layers of small diameter fibres, typically less than 20 μm, packed closely together. The working principle of microfiber and wire-mesh mist extractors are similar at high gas flow speeds. At low gas flow speed, the main method of mass transfer in microfiber mist extractors becomes Brownian diffusion [83]. The surface-to-volume ratio of microfiber mist extractors can be up to 150 times that of a wire-mesh mist extractor, allowing them to achieve high separation rates [83]. In turn, microfiber mist extractors have a high cost and pressure drop, and are more susceptible to flooding.

4. Cyclonic mist extractors, also known as centrifugal mist extractors, use centrifugal force to separate liquid droplets from the gas stream. The gas is forced to spin around a central core, causing the liquid droplets to be thrown outward and collected on the walls of the separator tank. Cyclonic mist extractors can achieve high performance and are least susceptible to plugging [83]. However, cyclonic mist extractors have a high cost and pressure drop, and do not perform well when the flow rate is variable [83].

An overview of the performance of the aforementioned mist extractors is presented in table 3.4. The final selection of mist extractor is that of the wire-mesh type. Variable load performance is

Mist extractor type	Wire-mesh	Vane	Microfiber	Cyclonic
Variable load performance	Very high	Low	High	Very low
Cut-off droplet diameter	5 μm	5 μm	< 3 μm	< 3 μm
Plugging Resistance	Low	High	Very low	Very high
Pressure drop	Low	Lowest	High	Very high
Durability	Medium	Very high	Low	Low
Capacity	High	Highest	Low	High
Cost	Lowest	Low	Very high	Very high

Table 3.4: Overview of mist extractor types covered in this work, and their performance based on given criteria [70, 83, 79, 85].

essential in the XINTC system, which eliminates vane-type and cyclonic mist extractors. The choice between wire-mesh and microfiber mist extractors comes down to cost efficiency. As the efficiency of wire-mesh mist extractors is deemed sufficient; the steep price increase towards microfiber mist extractors is deemed unnecessary.

The restricted headroom challenges the preference for horizontal orientation of a wire-mesh pad. The maximum diameter of the separator is 400 mm. A horizontal orientation of the feed inlet, as well as the gas outlet should be implemented to reduce head space. The wire-mesh pads have a minimum thickness of 100 mm [70]. Even if the thickness of the wire-mesh pad is reduced, there is insufficient spacing to account for the gas outlet, as well as a potential rise in liquid level. Instead, the implementation of a vertically oriented wire-mesh pad is evaluated. Literature suggests that for an air and water mixture, re-entrainment does not significantly occur at flow speeds below 6 m/s [70]. In the XINTC system, the gas velocity in the separators is an order of magnitude smaller. When compared to an air and water mixture, the difference between gas and liquid density in the oxygen and hydrogen separators are similar and larger, respectively. However, this deviation is relatively small and thus deemed unproblematic. It is concluded that vertically, and horizontally oriented wire-mesh pads perform similarly in this system. A vertically oriented wire-mesh pad of 100 mm thickness is suggested. For future works, it is recommended to evaluate the performance of wire-mesh pad thinner than the minimum thickness of 100 mm suggested in literature, as gas flow speeds are very low in this system. Reducing wire-mesh thickness should reduce the cost of both the wire-mesh pad and the separator itself through length reduction. It is recommended to purchase the wire-mesh pads as an off-the-shelf component, and will not be discussed in more detail.

3.4.5 Vortex Breakers

A vortex breaker should be positioned at each liquid outlet of the separators. Vortices at a liquid outlet in the separator can result in gas entrainment in the liquid stream. Any internal gas carryover poses a significant safety risk, as the liquid outlet of both separators is mixed before reentering the module half-cells. Vortex breakers shield against this gas entrainment by disrupting the formation, and persistence of vortices. Vortex breakers come in many different designs, of which most are made up of baffles around or above the liquid outlet [83]. The design and performance evaluation of vortex breakers in the separators is recommended for future works, and is not further covered in this work.

3.4.6 Sensors

The separators act as the central accumulation point of both liquid electrolyte and gas products, making them excellent monitoring stations. The implementation of sensors in the separators provides an opportunity to measure and analyze the characteristics of the two phases, thus assessing

system performance. To ensure optimal system performance and safety the following sensors should be implemented in the separators:

- A pressure sensor to monitor the static pressure. A maximum allowable overpressure of 500 mbar is assumed for the separators, in accordance with the PED [24]. Pressure sensors ensure that the internal pressure does not exceed the structural limit of the separators. Changes in pressure should be monitored, as a sudden drop or rise in pressure could indicate the formation of a leak or blockage, respectively.
- A temperature sensor to monitor the temperature of the liquid phase ensures that the maximum allowable temperature is not exceeded; protecting the system from overheating and polymer deterioration. Monitoring the temperature also helps to detect excessive system cooling, which reduces system efficiency according to Equation (2.1). A rapid increase, or decrease in bulk liquid temperature could indicate a malfunction of the cooling circuit.
- A conductivity sensor to enable monitoring of water consumption during production. The electrical conductivity of the liquid electrolyte is a function of the mass fraction of KOH [87]. The consumption of water alters the concentration of KOH, and thus the electrical conductivity. Data from the conductivity sensor should be used to determine the amount of feed water that should be added to maintain stable system operation.
- A gas-purity sensor to monitor the gas crossover between the two separators. Gas crossover forms a serious safety hazard, therefore it is mandatory to ensure that the level of impurity within each separator is well below the maximum allowable safety limit.
- Various liquid-level sensors are deployed to prevent the flooding, or draining of the separators. Flooding of the separator results in liquid carryover to downstream processes. The corrosive nature of the electrolyte poses a significant risk of chemical damage to any downstream equipment, that is not chemically resistant to KOH. Draining of the separator poses a serious safety hazard, due to the mixing of the liquid streams before reentering the AEL modules. To ensure these scenarios are never presented the following liquid-level sensors should be implemented:
  - LA(H): high-level pre-alarm to warn for an alarming increase in the liquid level.
  - LA(L): low-level pre-alarm to warn for an alarming decrease in the liquid level.
  - LZA(HH): high-level trip to engage full system shutdown if the liquid level rises too high.
  - LZA(LL): low-level trip to engage full system shutdown if the liquid level drops too low.

3.4.7 Separator Sizing

The diameter of a horizontal separator does not have a significant impact on separation performance. To ensure safe operation it is important that the liquid level remains well above the liquid output channels. The diameter should also be sufficiently large to house all necessary sensors. Based on the sizing of standard large diameter uPVC pipes an inner diameter of $D_{\text{sep}} = 0.4$ m is recommended. The maximum length of the separators is limited by the section length of 2 meters. The length of the separator is dependent on the length of the Schoepentoeter inlet device, the gravity settling section length, and the thickness of the wire-mesh pad. The possibility of utilizing different length hydrogen and oxygen separators should be considered whenever the purity of the hydrogen product is of greater importance than the purity of the oxygen product. In this case, the wire-mesh pad within the oxygen separator can also be removed. The removal of the wire-mesh pad frees up approximately 200 mm in the length of the separator; accounting for both pad thickness and pad-to-outlet spacing, assumed to be 100 mm. For a system where: the inlet devices are 200

mm in length; 100 mm of horizontal length is required for the liquid inlets and outlets pipes; and only the hydrogen separator contains a mist extractor, the total available length of the gravity settling sections of both separators becomes 1.4 m. It is recommended to implement a hydrogen separator of which $L_{H_2}^{set} = 0.8$ m, and an oxygen separator of which $L_{O_2}^{set} = 0.6$ m. Resulting in a total length for the hydrogen and oxygen separators of $L_{H_2}^{sep} = 1.2$ m, and $L_{O_2}^{sep} = 0.8$ m, respectively. Assuming a liquid fraction of $\varphi_L = 0.5$, the total liquid volume in the hydrogen and oxygen separators is then $V_{EL}^{H_2} = 75$ L, and $V_{EL}^{O_2} = 50$ L, respectively. Based on the work of Mera [58], the liquid volume of the separators only significantly affects the temperature response time of the system. The difference in temperature response time between the hydrogen and oxygen separators is not deemed problematic, due to the liquid electrolyte streams begin mixed.
The hydrogen separator is expected to separate liquid droplets down to 5 μm in diameter, as is the limit of the wire-mesh mist extractor. The gas-liquid feed is likely to behave as a spray with a mean droplet diameter of 500 μm [71, 79]. Assuming the variance in droplet diameter follows a normal distribution, the efficiency of the hydrogen separator proposed is over 99.8%. As the oxygen separator contains no mist-extractor, it is expected to separate droplets down to 25 μm in diameter (in accordance with Figure 3.23), resulting in an efficiency of over 99.7%.
The structural strength of the separators is evaluated through a stress analysis performed in SolidWorks 2022 [88]. In accordance with the PED [24], the separators should be capable of withstanding an overpressure of 0.5 bar. The tensile strength of uPVC is 41.4 - 52.7 MPa [23]. The stress analysis is performed at 0.5 bar overpressure, a separator length of 1.2 m, and a wall thickness of 10 mm. It is shown that the maximum von Mises stress that occurs within the model is 26.5 MPa. The von Mises stress is a measure of combined normal and shear stresses in a material [89]. Conventional uPVC piping of 400 mm inner diameter typically has more than 10 mm wall thickness. Since the von Mises stress reduces when the wall thickness is increased, it can be concluded that the separators proposed in this work are suited to withstand an overpressure of 0.5 bar.

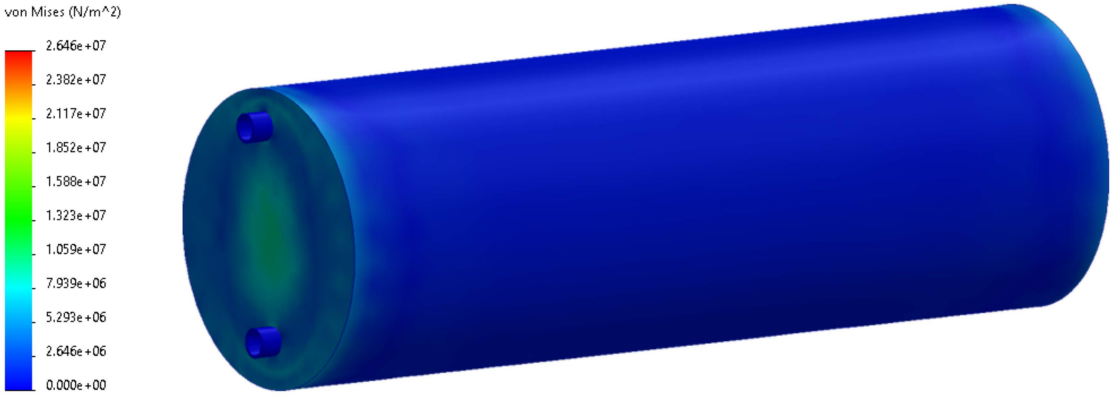

Figure 3.25: Separator stress analysis performed in SolidWorks 2022 [88]. An overpressure of 0.5 bar is introduced within a separator of length 1.2 m, inner diameter 0.4 m, and wall thickness of 10 mm. Maximum von Mises stress measured is 26.5 MPa, which is well below the tensile strength of uPVC (42-53 MPa [23]).

3.4.8 Heat Transfer

The effect of section airflow on separator heat transfer is evaluated in this section. The overall heat transfer coefficients of the hydrogen and oxygen separators $U_{H_2}^{sep}$ and $U_{O_2}^{sep}$, respectively, are determined through a thermal resistance model analysis. Figure 3.26 shows an overview of the

resistance model approximating the two-phase-containing separators. In this section, $A_{\mathrm{o}}^{\mathrm{sep}}$ and $A_{\mathrm{i}}^{\mathrm{sep}}$ represent the separator external and internal area, respectively. $D_{\mathrm{o}}^{\mathrm{sep}}$ and $D_{\mathrm{i}}^{\mathrm{sep}}$ represent external and internal tank diameter, respectively. $h_{\mathrm{air}}^{\mathrm{sep}}$, $h_{\mathrm{EL}}^{\mathrm{sep}}$ and $h_{\mathrm{g}}^{\mathrm{sep}}$ represent the separator air-side, inner-side electrolyte, and inner-side gas heat transfer coefficient respectively. k_{PVC} denotes the conductivity of uPVC, and is equal to $k_{\mathrm{PVC}} = 0.2$ [23].

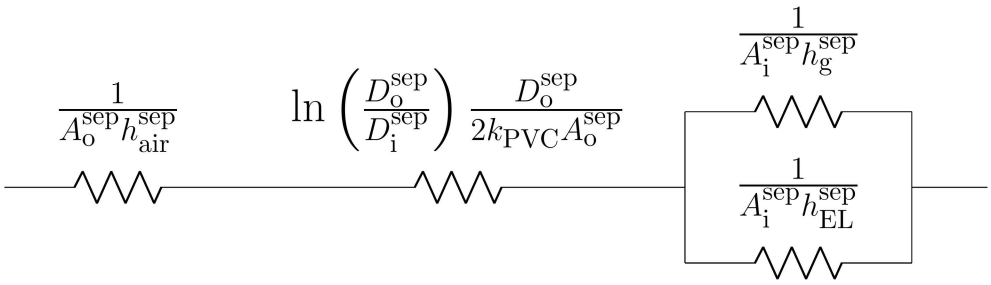

Figure 3.26: Resistance model overview of heat transfer between separator tank and section airflow. The leftmost resistor represents the air-side heat transfer coefficient. The middle resistor represents the conductive resistance of the separator tank material. The rightmost side parallel network represents the inside heat transfer coefficient, containing gas and liquid flow.

3.4.8.1 Air-side Heat Transfer Coefficient

The air-side heat transfer coefficient $h_{\mathrm{air}}^{\mathrm{sep}}$ is determined through a similar method as applied to the modules (section 3.1.3.2).

Natural convection
The methods to determine the convective heat transfer are covered in Appendix B. The Rayleigh number is evaluated to determine the average Nusselt number for natural convection across the separators $\overline{Nu}_{\mathrm{nat}}^{\mathrm{sep}}$. It is concluded that that the natural convection subjecting the separators, is always in the laminar regime ($Ra < 10^9$). As a result $\overline{Nu}_{\mathrm{nat}}^{\mathrm{sep}}$ is calculated using Equation (B.6a).

Forced Convection
To determine the average air-side Nusselt number for forced convection across a separator $\overline{Nu}_{\mathrm{forc}}^{\mathrm{sep}}$, the Reynolds number is evaluated. To determine Re, it is necessary to calculate the average air velocity around a separator $\overline{v}_{\mathrm{air}}^{\mathrm{sep}}$. As the volumetric flow rate of air $\dot{V}_{\mathrm{air}}$, is known, $\overline{v}_{\mathrm{air}}^{\mathrm{sep}}$ is assumed to be:

$$\overline{v}_{\mathrm{air}}^{\mathrm{sep}} = \dot{V}_{\mathrm{air}}/(W_{\mathrm{sec}}L_{\mathrm{sec}} - \frac{1}{2}D_{\mathrm{sep}}[L_{\mathrm{H_2}}^{\mathrm{sep}} + L_{\mathrm{O_2}}^{\mathrm{sep}}]) \tag{3.90}$$

A factor $\frac{1}{2}$ is introduced to account for the average area across a single separator. With the value of $\overline{v}_{\mathrm{air}}^{\mathrm{sep}}$ known it is possible to determine Re. The value of $\overline{Nu}_{\mathrm{forc}}^{\mathrm{sep}}$ is calculated using Equation (B.12).

Dominant Mode of Convection
As described in Appendix B.3, the dominant mode of convection is determined by evaluating the value of Gr/Re^2. Table B.1 describes the criteria for the forced, mixed, and natural convection regions. Figure 3.27 shows the relation between $\dot{V}_{\mathrm{air}}$ and Gr/Re^2, at various temperature ranges ΔT. Arbitrary cut-off values of $Gr/Re^2 = 2$ and $Gr/Re^2 = 0.3$, have been selected for the natural and forced regions, respectively. In this case ΔT represents the difference in operating temperature and ambient temperature. It is concluded that forced convection is the dominant mode of convective heat transfer for all operating conditions ($Gr/Re^2 \ll 1$).

3.4.8.2 Overall Heat Transfer of Separator Tanks

The expressions for total heat transfer coefficients are based on the thermal resistance model presented in Figure 3.26. Taking into account the gas volume fraction φ_g, the expression reads:

$$\frac{1}{U_{sep}A_o^{sep}} = \frac{1}{h_{air}^{sep}A_o^{sep}} + \ln\left(\frac{D_o^{sep}}{D_i^{sep}}\right)\frac{D_o^{sep}}{2k_{PVC}A_o^{sep}} + \frac{1}{A\left[\varphi_g h_g^{sep} + (1-\varphi_g)h_{EL}^{sep}\right]} \tag{3.91}$$

Filling in Equation (3.91), for both the oxygen and hydrogen separators yields expressions for $U_{H_2}^{sep}$, and $U_{O_2}^{sep}$. The expression of total heat flow from both separators follows:

$$\dot{Q}_{sep} = \Delta T D_o^{sep}(L_{H_2}^{sep}U_{H_2}^{sep} + L_{O_2}^{sep}U_{O_2}^{sep}) \tag{3.92}$$

Figure 3.28 shows the total value of $\dot{Q}_{sep}$, as a function of the volumetric flow rate of air $\dot{V}_{air}$, at a temperature difference of $\Delta T = 20$ °C. It is observed that the disturbances at $\dot{V}_{air} \approx 1400$ m^3/h, and $\dot{V}_{air} \approx 3800$ m^3/h, are in accordance with the change convective flow region, as shown in Figure 3.27. It is concluded that the separators relieve little of the total cooling load of the radiators.

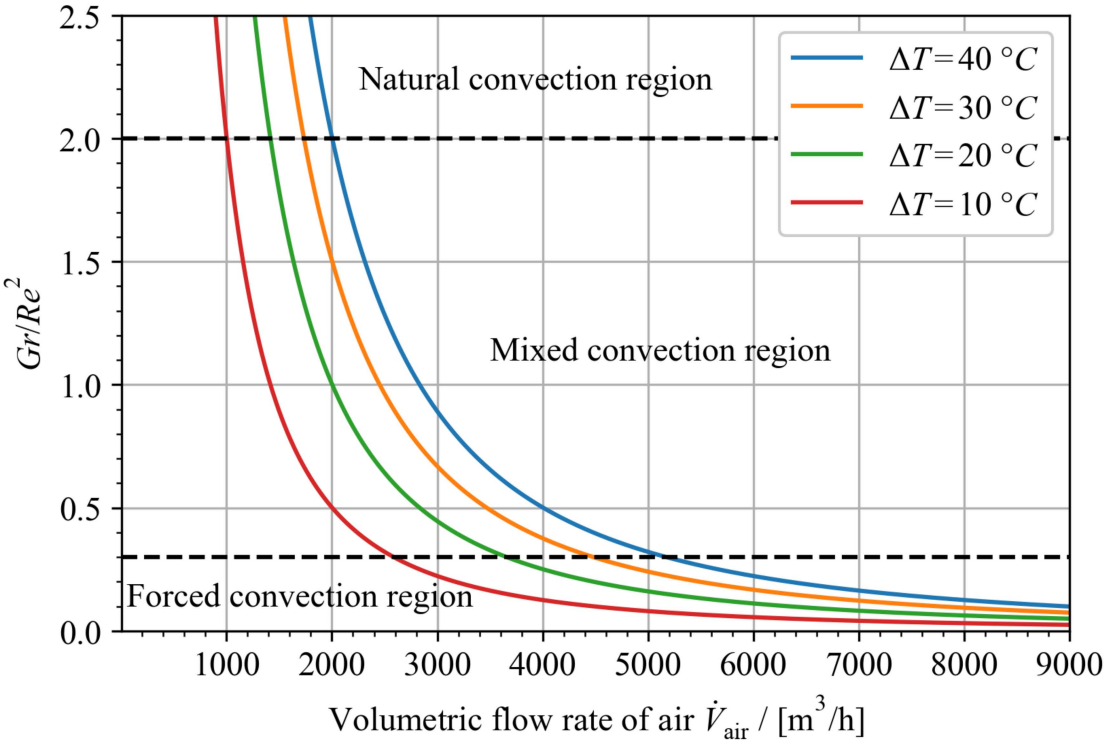

Figure 3.27: Mode of convection selection criterion Gr/Re^2, as a function of air volumetric flow rate $\dot{V}_{air}$, at various temperature ranges ΔT. Cut-off values for each respective convection region are denoted by the black striped lines.

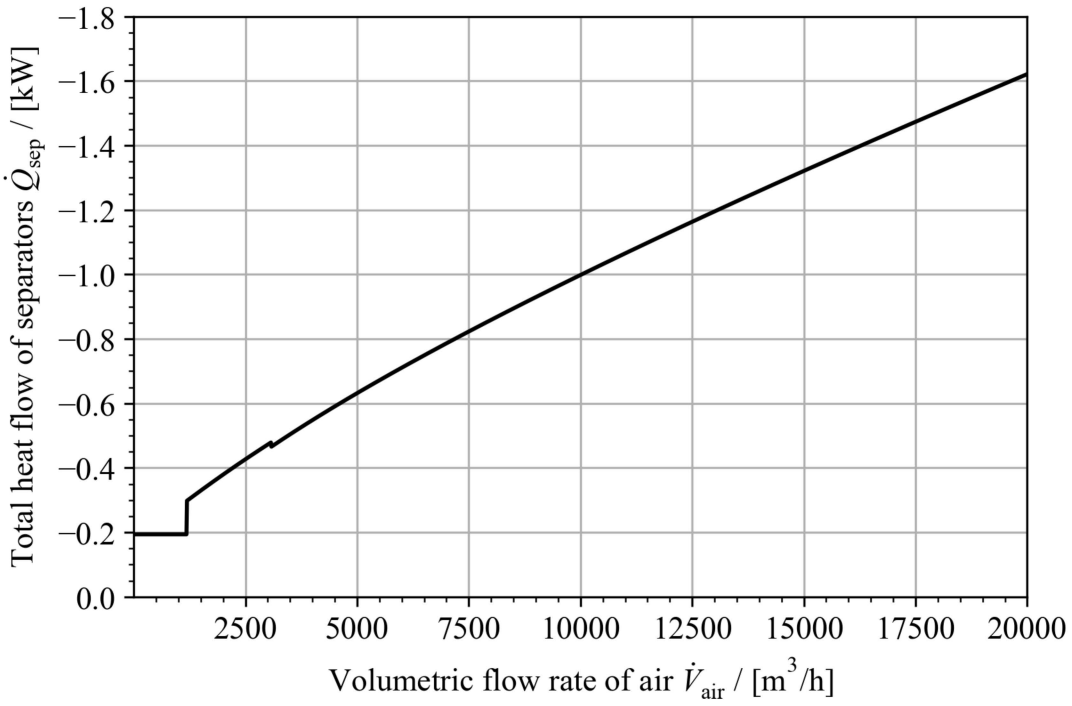

Figure 3.28: Total heat flow of separators $\dot{Q}_{\text{sep}}$, as a function of volumetric flow rate of air $\dot{V}_{\text{air}}$, at $\Delta T = 20$ °C. Disturbances shown at $\dot{V}_{\text{air}} \approx 1400$ m^3/h, and $\dot{V}_{\text{air}} \approx 3800$ m^3/h, in accordance with the change convective flow region; shown in Figure 3.27.

Chapter 4

System Analysis

Various statements regarding the properties and performance of the system components have been made throughout the previous chapter. In this chapter, the components will be assessed as part of their respective networks. First, the system airflow as a result of the ventilation requirement will be determined. After which, the heat network of the system will be evaluated. Finally, the effect of the components on the hydrodynamic network of the system will be evaluated.

4.1 Ventilation

Ensuring safety is of utmost importance when working with hydrogen. Hydrogen has a large range of flammable concentrations in air (4-74 vol%) [90]. Adequate ventilation helps to disperse any leaked or accumulated hydrogen gas, reducing the risk of ignition and subsequent accidents. Maintaining hydrogen concentrations within the container below 4% is crucial to ensure safe operation.

4.1.1 Required Airflow Rate for Safe Operation

It is suggested to set an upper limit of hydrogen concentration in air of 1%. Due to the potential for hydrogen accumulation in regions with low airflow, another safety factor 3 to the total ventilation capacity is suggested. A detailed analysis of the behaviour of the airflow within the container is recommended for future work. The volumetric flow rate of hydrogen production follows from Equation (3.4a). Figure 4.1 shows the relation between the volumetric flow rate of air required for sufficient ventilation, as a function of cell current. To account for the temperature dependant change in physical properties of air various ambient temperatures T_{amb}, are considered. The suggested airflow rate for safe operation is based on the extreme case $T_{\text{amb}} = 35$ °C, where it is concluded that the airflow within the section should be at least $\dot{V}_{\text{air}} > 11000$ m^3/h.

4.1.2 Fan Integration

The section fans should be positioned at the outer wall of the container, and at the face of each radiator. This way the cool air that enters the system directly encounters the radiators. A forced draft setup (fans positioned before radiators), is preferred over an induced draft setup (radiator positioned before fans), due to spacial limitations and the position of the separators. With a forced draft setup the airflow can be easily guided towards the top of the section, where the outlet should be positioned. It is crucial that the air is directed from the radiator through the section to ensure sufficient ventilation. The length and height of the radiator face are 750 mm, and 500 mm, respectively. To maximize both airflow rate and airflow distribution, it is recommended to utilize 250 mm fans. A total of six 250 mm fans can be positioned at the face of each radiator, resulting in a total of 12 fans per section. It is recommended to utilize constant volume fans,

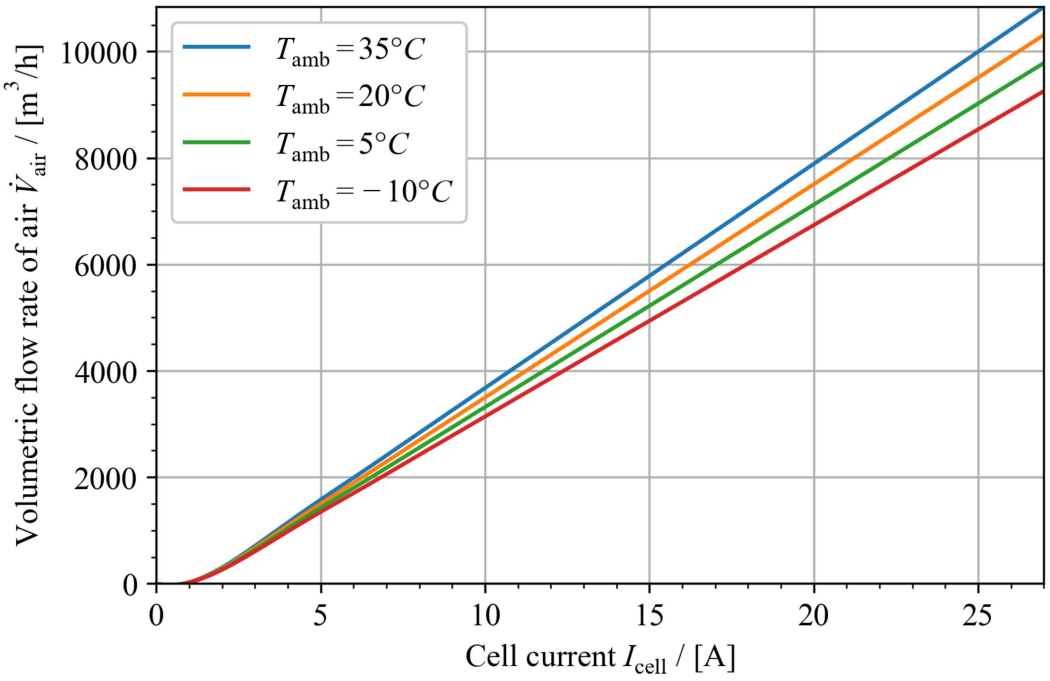

Figure 4.1: Volumetric flow rate required for ventilation safety requirement as a function of cell current, at various ambient temperatures T_{amb}.

as the large number of fans recommended already introduces a large degree of system control. Although variable volume fans would further improve system control they are not deemed worth their increased cost. Instead, it is recommended to implement a variable volume liquid pump at the tube-side of the radiators to assert system temperature control. Based on the ventilation requirement it can be concluded that the volumetric displacement of the fans should be 1000 m^3/h each. The total airflow rate of the section thus becomes $\dot{V}_{air} = 12000$ m^3/h. Note that the safety requirement of system ventilation varies with I_{cell}. The airflow rate should be adjusted to the section production rate accordingly. It is recommended that at least two outer fans of each radiator are left on to ensure a well-distributed airflow. This results in a total of 8 fans that can be turned on and off to respond to production capacity. It is recommended to adjust the number of active fans in increments of 2, i.e., one for each radiator; keeping the system balanced. It is concluded that the system airflow can be adjusted to I_{cell} accordingly; in increments of 2000 m^3/h, between 4000-12000 m^3/h. The values for I_{cell} associated with said values of $\dot{V}_{air}$, are presented in table 4.1. Note that the values for I_{cell} denote the maximum cell current at said airflow velocities. E.g., for $I_{cell} = 25.0$ A$\wedge\dot{V}_{air} = 10000$ m^3/h the ventilation requirement is respected, but for any cell current $I_{cell} \geq 25.1$ A, the airflow velocity should move to the next bracket, i.e., $\dot{V}_{air} = 12000$ m^3/h.

Number of fans		0	4	6	8	10	12
$\dot{V}_{air}$	/ [m^3/h]	0	4000	6000	8000	10000	12000
I_{cell}	/ [A]	0	10.8	15.4	20.1	25.0	27.0

Table 4.1: Values for the maximum cell current I_{cell}, corresponding to the recommended intervals of airflow rate $\dot{V}_{air}$. Data interpreted from Figures 4.1.

.

4.2 Heat Network

Throughout this work, the heat flow of the main system components has been presented as a function of airflow rate. With the value of $\dot{V}_{\text{air}}$ determined in the previous section it is possible to assess the heat balance within the section.

4.2.1 Critical Temperature

It has been shown in the previous chapter that the radiator cooling performance significantly outweighs the cooling introduced by other system components. It is suggested to consider heat flows other than that of the radiators negligible. The heat balance within the section thus depends on the heat generation of all modules $\dot{Q}^{\text{sec}}_{\text{mod}}$, and the cooling capacity of the radiators $\dot{Q}^{\text{sec}}_{\text{rad}}$. It has been determined in section 3.1.3.1, that $\dot{Q}^{\text{sec}}_{\text{mod}}$ can be expressed as a function of solely I_{cell}. In section 3.2.2 it has been shown that $\dot{Q}^{\text{sec}}_{\text{rad}}$ is a function of $\dot{V}_{\text{air}}$, the tube-side liquid velocity v_{tube}, and ΔT the difference in system and environmental temperature, T_{sys} and T_{amb}. It is important to note that there are three possible conditions regarding the heat balance of the system:

$$\begin{aligned} &\text{I.} && |\dot{Q}^{\text{sec}}_{\text{rad}}| < \dot{Q}^{\text{sec}}_{\text{mod}} && \text{system heats up} \\ &\text{II.} && |\dot{Q}^{\text{sec}}_{\text{rad}}| = \dot{Q}^{\text{sec}}_{\text{mod}} && \text{heat is balanced} \\ &\text{III.} && |\dot{Q}^{\text{sec}}_{\text{rad}}| > \dot{Q}^{\text{sec}}_{\text{mod}} && \text{system cools down} \end{aligned}$$

Ideally, the system is balanced and operates according to condition II. The system should be adjusted to approach condition II whenever it is not met. The environmental temperature at which the heat network is balanced, and thus condition II is met; is defined as the critical ambient temperature T_{crit}:

$$T_{\text{crit}} \equiv T_{\text{sys}} - \frac{\dot{Q}^{\text{sec}}_{\text{mod}}}{(\dot{Q}^{\text{sec}}_{\text{rad}}/\Delta T)} \tag{4.1}$$

T_{crit} is related to the aforementioned conditions through:

$$\begin{aligned} &\text{I.} && |\dot{Q}^{\text{sec}}_{\text{rad}}| < \dot{Q}^{\text{sec}}_{\text{mod}} \ \wedge \ T_{\text{amb}} > T_{\text{crit}} \\ &\text{II.} && |\dot{Q}^{\text{sec}}_{\text{rad}}| = \dot{Q}^{\text{sec}}_{\text{mod}} \ \wedge \ T_{\text{amb}} = T_{\text{crit}} \\ &\text{III.} && |\dot{Q}^{\text{sec}}_{\text{rad}}| > \dot{Q}^{\text{sec}}_{\text{mod}} \ \wedge \ T_{\text{amb}} < T_{\text{crit}} \end{aligned}$$

Figure 4.2 shows a decision tree recommended for the heat network system, where ΔT_{sys} denoted the change in system temperature. The value of ΔT_{sys} should be determined through the temperature sensors present in the separators. Whenever condition II is not met it should be checked whether condition I is presented, as overheating poses a greater risk to the system than T_{sys} running too low. If condition I is met it is recommended to approach condition II by increasing $\dot{V}_{\text{air}}$ or v_{tube}, or decreasing I_{cell}; in order of priority. Increasing $\dot{V}_{\text{air}}$ should be considered first, as air-side pressure drop is insignificant at all operational values of $\dot{V}_{\text{air}}$ (concluded in section 3.2.3.1). Tube-side pressure drop is much more prominent, and v_{tube} should thus be second in order. Decreasing I_{cell} should only be considered when both $\dot{V}_{\text{air}}$ and v_{tube} are maximized, as it negatively affects hydrogen production rate. If this scenario presents itself the relation shown in Figure 4.3 should be consulted to determine a suitable cell current based on ambient temperature. Figure 4.3 shows T_{crit} as a function of I_{cell}, for $T_{\text{sys}} = 40$ °C, and maximum air-side and tube-side flow ($\dot{V}_{\text{air}} = 12000$ m^3/h, and $v_{\text{tube}} = 2$ m/s, respectively). When I_{cell} is 0, and cannot be further reduced a full system shutdown should be engaged. It is observed that the system is capable of operating at maximum capacity for a difference in ambient and system temperatures of temperature $\Delta T \geq 15$ °C.
When condition III is presented care must be taken to ensure T_{sys} does not become too low; hindering system performance. It is recommended to approach condition II by increasing I_{cell},

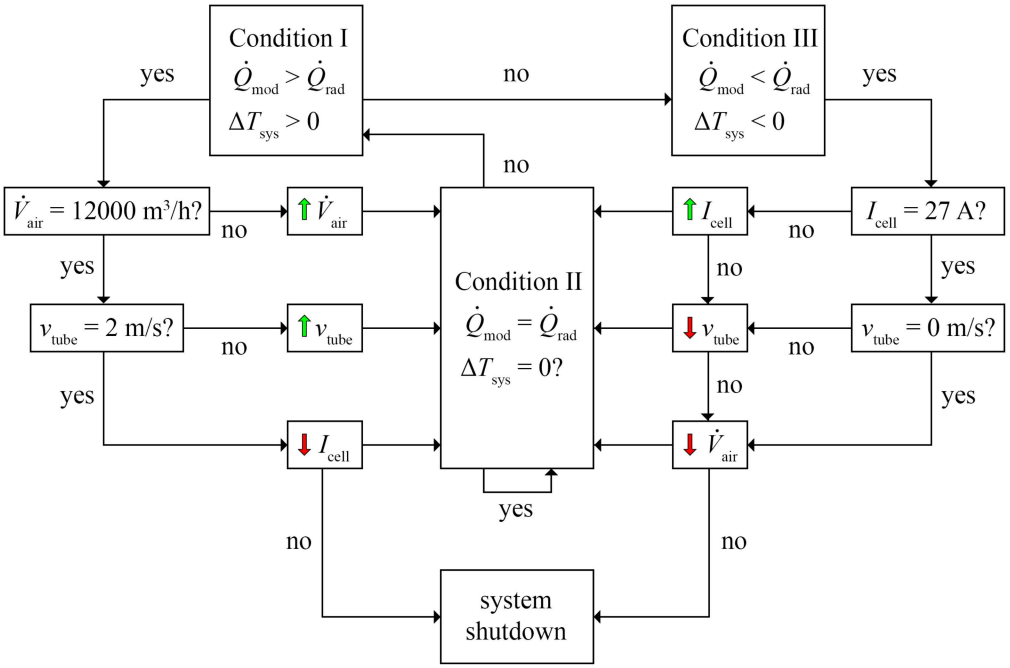

Figure 4.2: Decision tree for the heat network system. With: radiator cooling capacity and section heat generation, $\dot{Q}^{\text{sec}}_{\text{rad}}$ and $\dot{Q}^{\text{sec}}_{\text{mod}}$ respectively; change in system temperatureΔT_{sys}; airflow rate $\dot{V}_{\text{air}}$; tube-side liquid flow velocity v_{tube}; and cell current I_{cell}. Green and red arrows indicate an increase and decrease in corresponding variables, respectively.

or decreasing v_{tube} or $\dot{V}_{\text{air}}$; in order of priority. Increasing I_{cell} should be considered first, as it increases the hydrogen production rate. If I_{cell} cannot be increased, v_{tube} should be decreased based on the same logic mentioned above. It should be noted that $\dot{V}_{\text{air}}$ should not be decreased below the corresponding safety requirement presented in table 4.1. A system shutdown should be engaged if $\dot{V}_{\text{air}}$ cannot be further reduced. Figure 4.4 shows T_{crit} as a function of v_{tube}, at various operating conditions.

4.2.2 Waste Heat Recovery

Waste heat recovery options are limited for air-cooled systems. The waste stream of the system is considered a low-grade waste heat stream due to its low temperature ($\sim$ 30 °C) [91]. It is not recommended to utilize the heated airflow directly due to the risk of hydrogen contamination. The cooling capacity of the system is inversely related to the environmental temperature, i.e., the waste gas stream will be hot during summer and cool during winter. When powered by RES, their intermittent nature further complicates waste heat recovery. More waste heat recovery methods become available when a liquid cooling solution is present. Low-temperature heat engines, such as Kalina and organic Rankine cycle (ORC) engines enable heat-to-power conversion. ORC engines are most commonly used for the power conversion of waste heat [91]. However, ORC engines achieve very low thermal efficiency (<5%) at low temperatures, with Kalina engines showing similar performance [92]. Utilization of the waste heat air stream is deemed unfeasible.

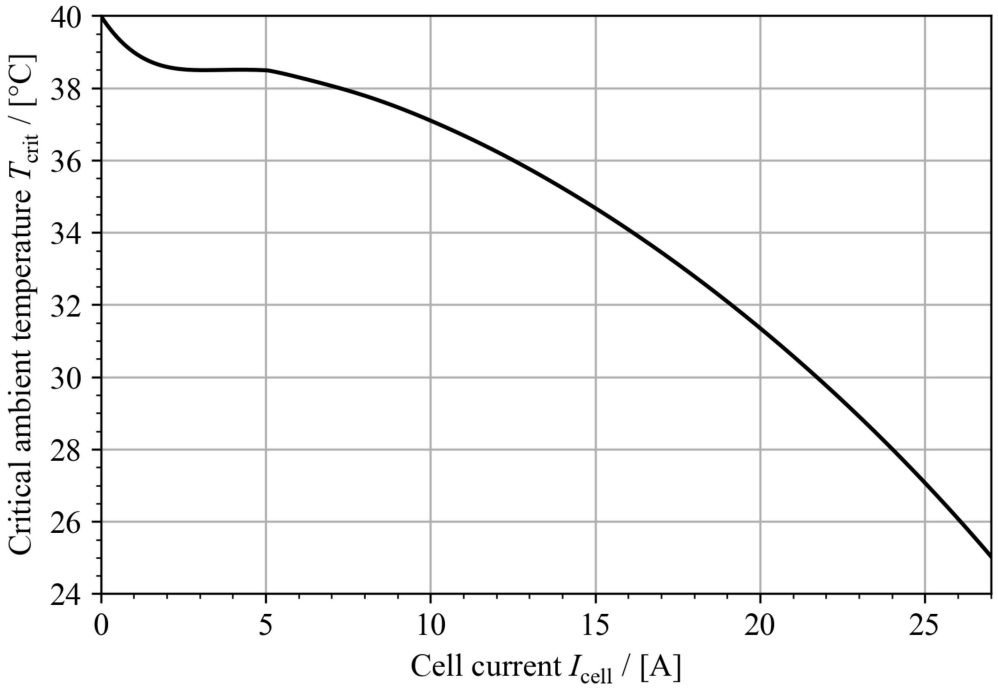

Figure 4.3: Critical ambient temperature T_{crit}, as a function of cell current I_{cell}, for $T_{\text{sys}} = 40$ °C, and maximum air-side and tube-side flow ($\dot{V}_{\text{air}} = 12000$ m^3/h, and $v_{\text{tube}} = 2$ m/s, respectively).

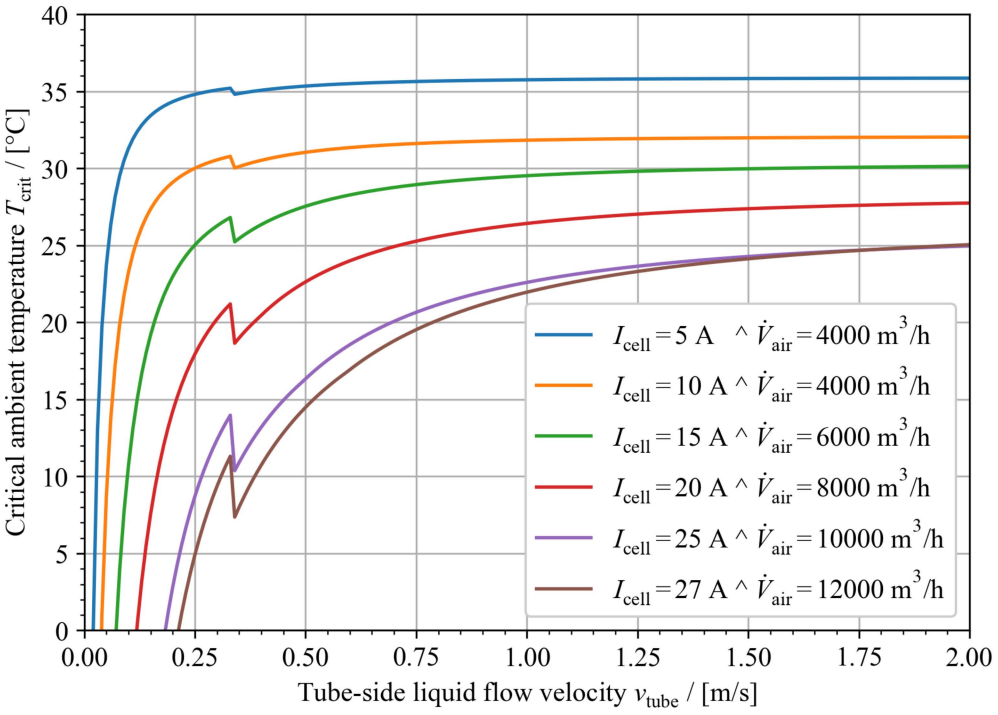

Figure 4.4: Critical ambient temperature T_{crit}, as a function of tube-side liquid flow speed v_{tube}, at an operating temperature of $T_{\text{sys}} = 40$ °C, and various operating conditions.

4.3 Hydrodynamic Network

Throughout this work, the hydrodynamic properties of the main system components have been presented. In this section, the hydrodynamic network of the XINTC section will be discussed. In conformity with the PED, the maximum allowable overpressure within the system is 0.5 bar. Figure 4.5 shows an illustration of the flow channels within the section. There are three flow loops within the system. First, the electrolyzer flow loop. Second and third, the isolated flow loops of the radiator and separator pairs. These flow loops will be evaluated in this section. Information regarding hydrodynamic losses is discussed in Appendix C. Note that due to the low fluid flow velocities inside of the separators, its pressure drop is considered negligible.

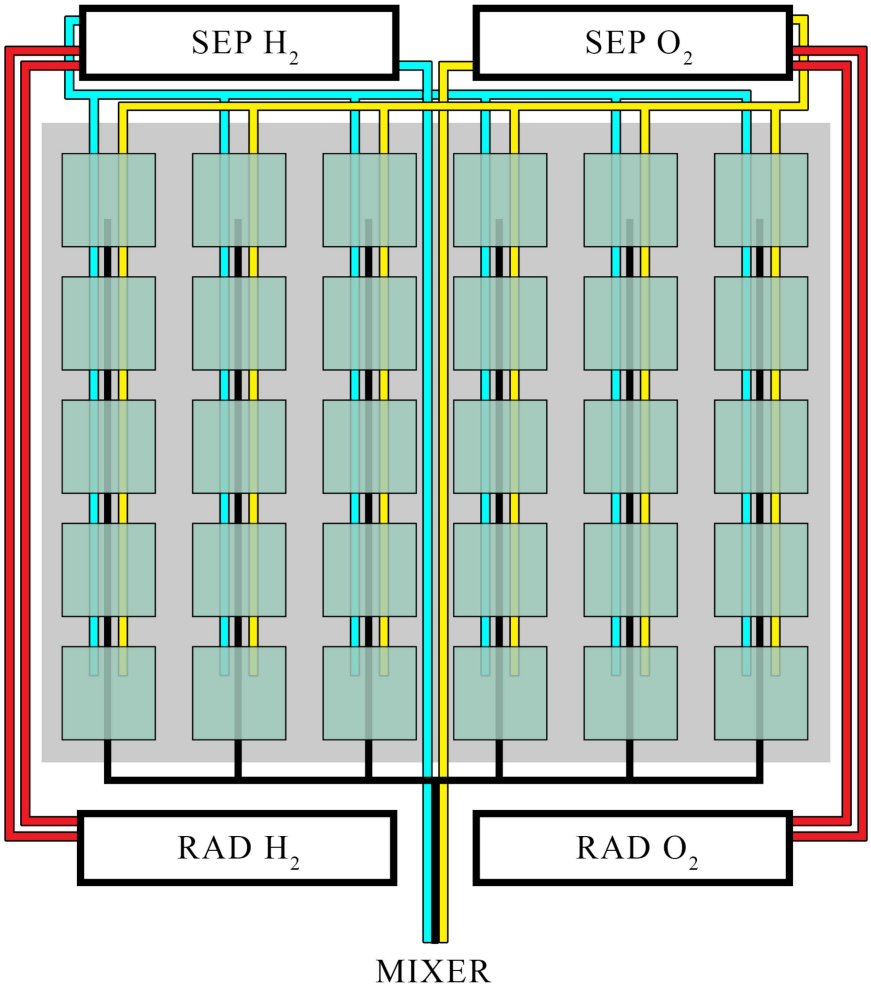

Figure 4.5: Illustration of the flow network within the XINTC section. Black lines represent electrolyte flow from the mixer to module half-cells via the flow panels. Cyan lines represent flows originating from the hydrogen half-cells. Yellow lines represent flows originating from the oxygen half-cells. Red lines represent the electrolyte flow loops between the radiators (RAD H_2 and RAD O_2) and separators (SEP H_2 and SEP O_2).

4.3.1 The Electrolyzer Flow Loop

The flow electrolyzer flow loop contains the mixer, a dividing manifold, the flow panels, the modules, a combining manifold, and the separators. The liquid flow rates within this flow loop follow from the set value of electrolyte volumetric flow rate in the modules $\dot{V}_{\mathrm{EL}}^{\mathrm{mod}}$, Equation (3.1). Leaving the separator tank, the flow encounters a 90° turn, before travelling through a downcomer towards the mixer. Flow contraction losses are negligible [69]. The flow velocity in the liquid downcomer –and thus the pressure drop– depends on the channel diameter. It is recommended to utilize drawn PVC tubing for all channels within the flow loops. When considering a turn-to-channel diameter of 2, a turn loss coefficient of $K_{90} = 0.3$ follows from table C.2. The wall friction loss K_{fr}, are determined through the methods described by Churchill [72], and is covered in Appendix C.2.2. The roughness of the drawn PVC tubing $\epsilon = 1.5$ μm, follows from table C.1. The total pressure drop in the downcomer is then the sum of the frictional and turn losses:

$$\Delta P_{\mathrm{dc}} = (K_{\mathrm{fr}} + K_{90}) \frac{\rho_{\mathrm{EL}} v_{\mathrm{dc}}^2}{2} \tag{4.2}$$

where v_{dc} is the flow velocity in the downcomer. Figure 4.6 shows the pressure drop in the liquid downcomer ΔP_{dc}, of the electrolyte flow loop (including a 90° turn), as a function of channel diameter. It is observed that a downcomer diameter of $D_{\mathrm{dc}} = 5$ cm offers manageable pressure drop ($\Delta P_{\mathrm{dc}} = 5.7$ mbar), and is therefore recommended. This diameter is also recommended for the other channels in the electrolyzer flow loop. The mixer is assumed to be a Y-junction to collect the flows from both separators, followed by a 180° turn. The joining loss coefficient for Y-junction with a branch angle of 90°, is sourced from the work of Miller [69], and equals $K_{13} = 0.2$. Note that it is assumed that the Y-junction has equal branch diameters. The loss coefficient of a 180° turn with a turn-to-diameter ratio of 2, follows from table C.2, and equals $K_{180} = 0.4$. The total pressure drop in the mixer is then:

$$\Delta P_{\mathrm{mix}} = (K_{13} + K_{180}) \frac{\rho_{\mathrm{EL}} v_{\mathrm{mix}}^2}{2} = 26.3 \text{ mbar} \tag{4.3}$$

where v_{mix} is the flow velocity in the mixer. Since it is assumed that the branch diameters of the Y-junction are equal, the velocity within the mixer is equal to:

$$v_{\mathrm{mix}} = 2 \cdot v_{\mathrm{dc}} \tag{4.4}$$

After the mixer, the flow travels towards a manifold that divides the flow across the flow panels. This manifold differs from the ones covered in Appendix C.2.5, because the feed flow is perpendicular to that of the manifold and located at its centre. Figure 4.7 shows an illustration of said manifold. The manifold diameter is assumed to be equal to the diameter of the downcomer ($D_{\mathrm{mani}} = 5$ cm). The flow velocity is then also equal to that inside the mixer. The loss coefficient at the inlet is assumed to be equal to the loss coefficient of a dividing T-junction, and its value $K_{\mathrm{in}} = 1.1$ follows from the work of Miller [69]. The inlet pressure drop is then:

$$\Delta P_{\mathrm{in}} = K_{\mathrm{in}} \frac{\rho_{\mathrm{EL}} v_{\mathrm{mix}}^2}{2} = 48.2 \text{ mbar} \tag{4.5}$$

The manifold pressure drop is determined with a method similar to that of the flow panels, covered in section 3.3.3, and will not be discussed in detail. The wall friction losses are again determined through the methods described by Churchill [72]. The reduction in flow velocity as a result of the flow division over the branches is accounted for in the friction loss calculation. Table 4.2 shows the value of the total pressure drop in the division manifold, where the branch number n is counted from left to right. It is not possible to determine the normalized pressure drop, and thus the flow distribution, due to a lack of knowledge on the pressure drop within the electrolyzer modules. It is important that when this information is available, the flow distribution is analyzed to ensure

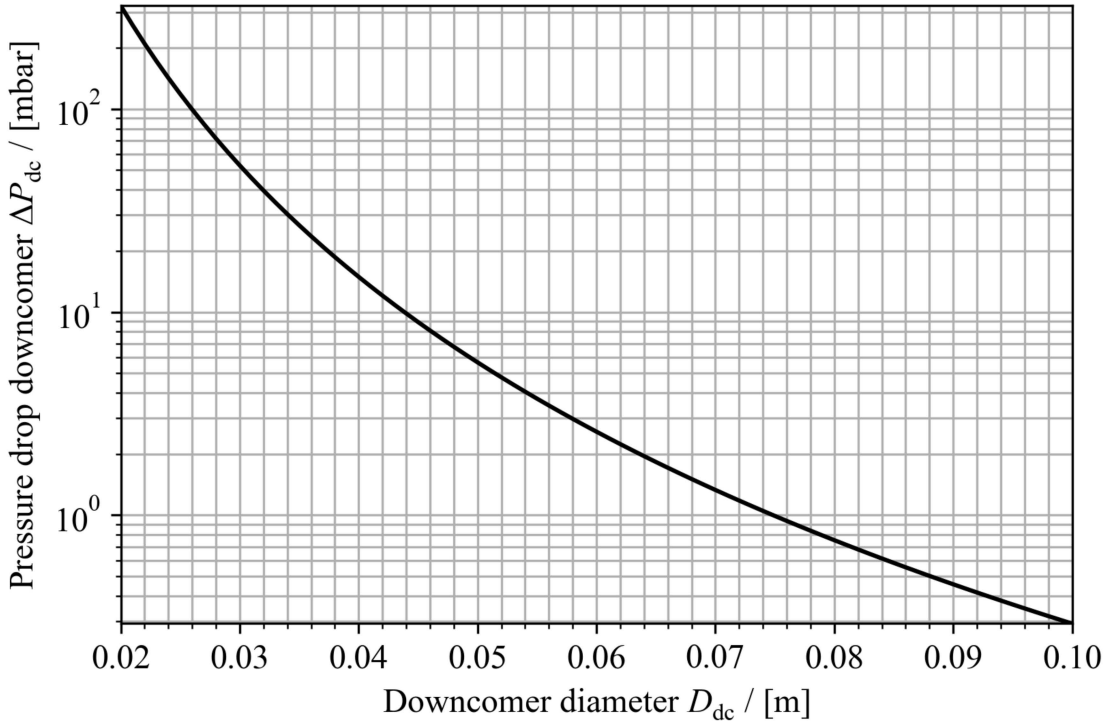

Figure 4.6: Pressure drop in the liquid downcomer ΔP_{dc} of the electrolyte flow loop, including a 90° turn, as a function of the downcomer diameter D_{dc}.

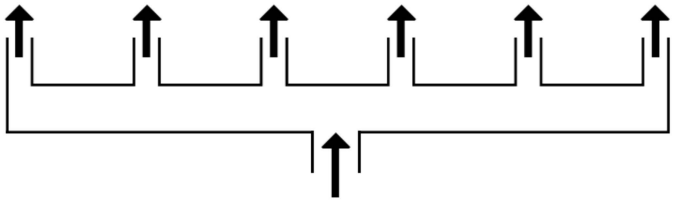

Figure 4.7: Illustration of the manifold responsible for the flow division across the flow panels. Feed flow enters perpendicular to that of the manifold.

proper flow distribution across the flow panels. As the flow rate within the flow panels is correlated to the flow rate within the modules, it is crucial to ensure the flow rate within the module cells does not exceed the limit set by the gas-crossover rate. A flow division pressure drop of $\Delta P_{\mathrm{div}} = 13.2$ mbar, is assumed to be a conservative estimate. The total pressure drop across the inlet manifold is then the sum of the inlet loss, and the dividing losses:

$$\Delta P_{\mathrm{mani}}^{\mathrm{in}} = \Delta P_{\mathrm{div}} + \Delta P_{\mathrm{in}} = 61.4 \text{ mbar} \tag{4.6}$$

The pressure drop along the flow panels is determined in section 3.3.3, and assumed to be $\Delta P_{\mathrm{FP}} = 3.7$ mbar. After the flow panels, the flow is collected in another manifold. The pressure drop along the branches of this manifold ΔP_{join}, is summarized in table 4.3. The branch number n, is counted from the first branch at the manifold outlet, and the manifold diameter is assumed to be $D_{\mathrm{mani}} = 5$ cm. Effects of two-phase flow phenomena are considered negligible, as a result of the findings in section 3.3.3.1. The maximum value of $\Delta P_{\mathrm{join}} = 3.4$ mbar is considered a conservative estimate

Table 4.2: Values of pressure drop components within the manifold responsible for the flow division across the flow panels. Branch flow velocity v_{12} is a result of the module flow rates, Equation (3.1). Total pressure drop is the sum of the division pressure drop ΔP_{div}, and the frictional pressure drop ΔP_{fr}. The volumetric flow rate fraction $\dot{V}_2/\dot{V}_1$, is based on v_{12} and manifold flow velocity v_{13}. Value of loss coefficients K, follow from Figure C.2, and are based on the volumetric flow rate fraction.

n	v_{12}/ [m/s]	v_{13}/ [m/s]	$\dot{V}_2/\dot{V}_1$,	K_{12}	K_{13}	ΔP_{div}/ [mbar]	**Friction** ΔP_{fr}/ [mbar]	**Total** ΔP_{div}/ [mbar]
1	1.178	0.424	1	1.3	0.3	12.57	0.59	13.2
2	1.178	0.848	0.5	0.9	0	8.45	0.53	8.98
3	1.178	1.272	0.33	0.85	0	7.98	0.36	8.34
4	1.178	1.272	0.33	0.85	0	7.98	0.36	8.34
5	1.178	0.848	0.5	0.9	0	8.45	0.53	8.98
6	1.178	0.424	1	1.3	0.3	12.57	0.59	13.2

Table 4.3: Values of pressure drop components within the manifold responsible for the flow collection from the flow panels. Branch flow velocity v_{12} is a result of the module flow rates, Equation (3.1). The total pressure drop is equal to the combining pressure drop ΔP_{join}. The volumetric flow rate fraction $\dot{V}_2/\dot{V}_3$, is based on v_{12} and manifold flow velocity v_{13}. Value of loss coefficients K, follow from Figure C.2, and are based on the volumetric flow rate fraction.

n	v_{23}/ [m/s]	v_{13}/ [m/s]	$\dot{V}_2/\dot{V}_3$,	K_{12}	K_{13}	ΔP_{join}/ [mbar]
1	0.589	1.272	0.17	-0.35	0.3	3.42
2	0.589	1.06	0.2	-0.3	0.25	2.16
3	0.589	0.848	0.25	-0.1	0.3	2.19
4	0.589	0.636	0.33	0.1	0.35	2.15
5	0.589	0.424	0.5	0.4	0.5	2.51
6	0.589	0.212	1	0.5	1.1	2.47

for the joining losses. Accounting for the varying flow velocity within the manifold, the pressure drop due to frictional losses within the combining manifold following the flow panels is $\Delta P_{\text{fr}} = 1.0$ mbar. Losses due to the sudden expansion of the branch flow are calculated with Equation (C.11), and are $\Delta P_{\text{exp}} = 1.0$ mbar. The resulting pressure drop along the combining manifold $\Delta P^{\text{out}}_{\text{mani}}$, is then:

$$\Delta P^{\text{out}}_{\text{mani}} = \Delta P_{\text{join}} + \Delta P_{\text{fr}} + \Delta P_{\text{exp}} = 5.4 \text{ mbar} \tag{4.7}$$

After the combining manifold, the flow encounters two 90° turns before returning to the separators. Frictional losses are considered negligible, as the channel length from the combining manifold to the separators is small. The turn loss coefficient is again assumed to be $K_{90} = 0.3$. The resulting pressure drop is then:

$$\Delta P_{\text{turns}} = 2 \cdot K_{90} \frac{\rho_{\text{EL}} v^2_{\text{dc}}}{2} = 6.6 \text{ mbar} \tag{4.8}$$

The pressure drop along the Schoepentoeter inlet device is considered negligible. The sudden expansion losses are also considered negligible, as the liquid flow enters in the gaseous fraction of the separators. The total pressure drop along the electrolyzer flow loop is then:

$$\Delta P = \Delta P_{\text{dc}} + \Delta P_{\text{mix}} + \Delta P^{\text{in}}_{\text{mani}} + \Delta P_{\text{FP}} + \Delta P^{\text{out}}_{\text{mani}} + \Delta P_{\text{turns}} = 109 \text{ mbar} \tag{4.9}$$

Note that this does not include the pressure drop along the electrolyzer modules. It is speculated that the pressure drop along the modules is insignificant, due to the low flow velocity inside of

the electrolyzer half-cells. A rough estimation of the pressure drop within the module half-cells, based on the cell architecture and electrolyte flow rates, suggests that the pressure drop within the modules is less than 5 mbar. It is concluded that the pressure drop within the electrolyte flow loop is well below the 500 mbar limit set by the PED [24].

4.3.2 The Radiator Flow Loop

The flow inside the radiator flow loops travels from the separator to the radiator and back. The flow travels through a downcomer towards the radiator, and through an upcomer towards the separator. Both the up- and downcomer contain two 90° turns, for which the turn loss coefficient is again assumed to be $K_{90} = 0.3$. The electrolyte flow rate follows from the tube-side flow velocity in the radiator:

$$\dot{V}_{\text{rad}} = n_{\text{tube}} \cdot v_{\text{tube}} \frac{\pi (D_{\text{i}}^{\text{rad}})^2}{4} \tag{4.10}$$

The flow velocity within the up- and downcomer v_{dc} is than a function of $\dot{V}_{\text{rad}}$, and the up- and downcomer diameter D_{dc}:

$$v_{\text{dc}} = \frac{4\dot{V}_{\text{rad}}}{\pi D_{\text{dc}}^2} \tag{4.11}$$

The total pressure drop within the radiator flow loops is the sum of the pressure drop components introduced by the turn losses, the wall friction losses, the radiator, and the sudden expansion losses encountered when the flow reenters the separator. In accordance with the methods described in Appendix C, the pressure drop in the up- and downcomer, excluding the radiator, is:

$$\Delta P_{\text{dc}} = (K_{\text{fr}} + 4 \cdot K_{90} + K_{\text{exp}}) \frac{\rho_{\text{EL}} v_{\text{dc}}^2}{2} \tag{4.12}$$

where a factor 4 is introduced to account for a total of four tube turns. Figure 4.8 shows ΔP_{dc} as a function of D_{dc}. It is observed that for $D_{\text{dc}} = 5$ cm, the pressure drop is manageable ($\Delta P_{\text{dc}} = 16.5$ mbar). It is therefore recommended the up- and downcomer diameter is 5 cm. In section 3.2.3.2, it has been determined that the pressure drop in the radiator is 234 mbar, at maximum tube-side flow velocity. It is observed that the pressure drop within the radiator flow loop is dominated by the radiator pressure drop. When operating at maximum capacity ($v_{\text{tube}} = 2$ m/s), the total pressure drop in the radiator flow loop is:

$$\Delta P = \Delta P_{\text{rad}} + \Delta P_{\text{dc}} = 251 \text{ mbar} \tag{4.13}$$

It is concluded that the pressure drop within the radiator flow loops is greater than that of the electrolyzer flow loops, and is well below the 500 mbar limit set by the PED [24].

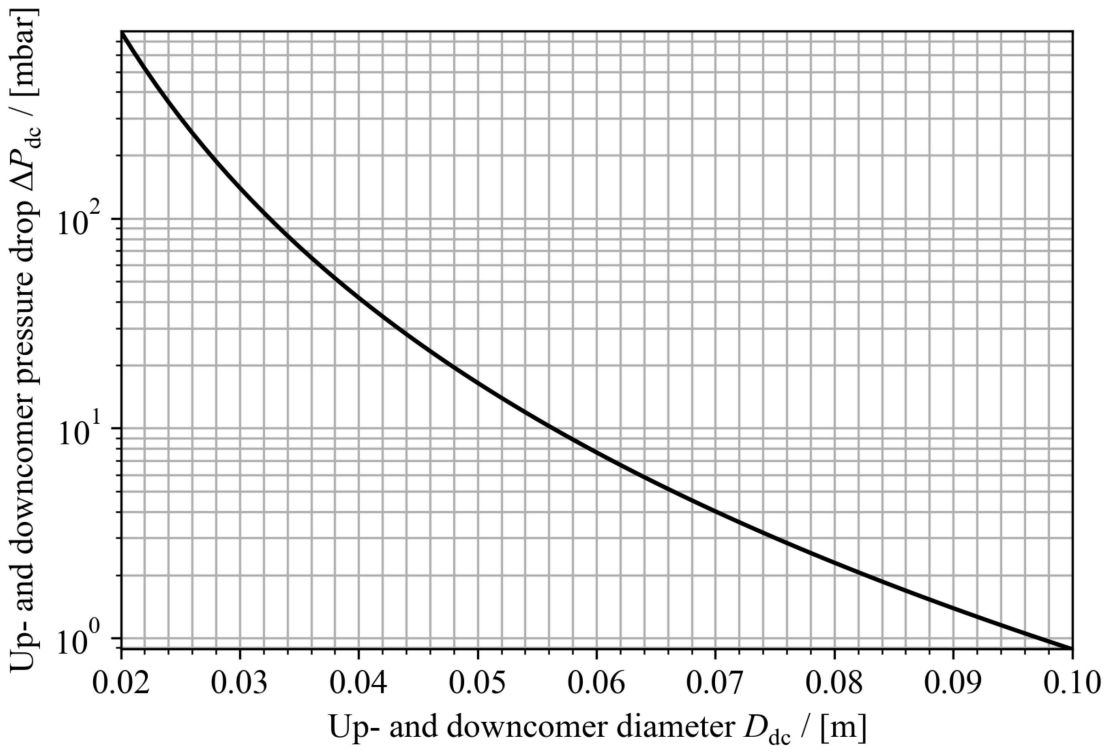

Figure 4.8: Pressure drop in the up- and downcomers ΔP_{dc} of the radiator flow loop, as a function of the up- and downcomer diameter D_{dc}. Total pressure drop is the sum of the pressure drop components of the turn losses, the wall friction losses, and the sudden expansion losses encountered when the flow reenters the separator.

Chapter 5

Conclusion and Recommendations

5.1 Conclusion

The adverse effects of the fossil fuel dominated global energy market is currently a widely debated subject. As a result, renewable energy sources, such as wind and solar, are rapidly gaining popularity in the industrial and consumer markets. The intermittent nature of the most prominent renewable energy sources introduces a disconnect between the supply and demand of energy. Utilizing hydrogen as an energy storage medium shows great promise for both centralized and decentralized energy storage. According to the Net Zero Emissions by 2050 scenario, hydrogen production through water electrolysis is expected to increase significantly in the upcoming decades.

In anticipation of the emerging hydrogen market, a containerized alkaline water electrolysis system has been designed in this work. Alkaline electrolysis was deemed the most suitable type of electrolysis, due to its durability and independence of rare earth metals. The proposed system was developed in conjunction with the Dutch company XINTC, and targets the middle sector of the upcoming hydrogen market (150 kW - 50 MW). A modular system design approach was adopted, emphasizing high system modularity and the economy of numbers. The implementation of modular system design brings significant benefits to emerging markets, namely: cost reductions, decreased time-to-market, high quality control, and flexibility in system expansion or reduction. Although absent in literature, the availability of modular electrolyzer systems in the consumer market proves that there is demand for such systems. The proposed system has three degrees of modularity. First, the containerized system itself is a module. Second, the hydrogen production in each container is distributed across multiple modular sections. Last, the large number of alkaline electrolyzer modules that are installed in each section.

This thesis focused on the design of the hydrogen-producing modular sections of the XINTC system. Each section contains heat exchangers, two gas-liquid separators, multiple flow panels and many alkaline electrolyzer modules. With the already developed alkaline electrolyzer module at its core, the general design, sizing, material selection, heat transfer, and hydrodynamics of the section components have been researched and evaluated. The system has been designed in conformity with the vision of XINTC: containerized, decentralized, and plug-and-play. The containerized approach introduces spatial limitations to the system. The decentralized and plug-and-play nature of the system requires the utilization of an air-cooled heat exchanger. The system operates at atmospheric pressure, resulting in significant capital expenditure reductions. The absence of pressure-induced stresses allows for the utilization of low-cost materials, namely plastics. Due to their high chemical resistance, plastics are well suited to be used in conjunction with alkaline water electrolysis systems.

5.1.1 Electrolyzer Modules

The XINTC alkaline electrolyzer modules offer a nominal capacity of 5.0-6.5 kW. The design of the electrolyzer modules was finalized by XINTC before writing this work, which deems the design, sizing and material selection unnecessary. The electrolyte flow rate within the modules was shown to be limited by the membrane gas-crossover rate. Pressure drop within the modules has been approximated to be less than 5 mbar. At maximum capacity, the total heat generation of all modules in each section has been shown to be $\dot{Q}^{\text{sec}}_{\text{mod}} = 55$ kW.

5.1.2 Heat Exchangers

An air-cooled heat exchanger design has been proposed. The corrosive nature of the alkaline electrolyte necessitates the utilization of chemically resistant materials, typically stainless steel. A plate-finned tube heat exchanger was deemed most suitable for the XINTC system. In this heat exchanger design, plate-fins are press-fitted to the heat exchanger tubes. As the plate-fins do not come in direct contact with the electrolyte, they can be manufactured from aluminium; offering greater heat transfer performance than stainless steel. The heat exchanger load has been divided over two identical radiators, resulting in a significant reduction in tube-side pressure drop, and greater system temperature control. To bypass the module gas-crossover limit, it has been recommended to isolate the electrolyte flow loops of the radiators from that of the electrolyzers. Changes in the material properties of both air and electrolyte, due to variations in temperature, have been shown to have little impact on the overall cooling capacity of the radiators, which was shown to be dominated by the difference in ambient and system temperature. At maximum capacity ($v_{\text{tube}} = 2$ m/s, and $\dot{V}_{\text{air}} = 12000$ m^3/h), the cooling capacity per unit temperature difference of the proposed radiator pair was determined to be $\dot{Q}^{\text{sec}}_{\text{rad}} = 3.7$ kW/K. The maximum pressure drop across each radiator has been shown to be $\Delta P_{\text{rad}} = 234$ mbar, with a well-distributed tube flow velocity. The air-side pressure drop along the radiator has been shown to be insignificant.

5.1.3 Flow Panels

The novel concept of flow panels was covered in this work. No concrete information regarding this concept was found in literature. The large panels with embedded flow channels contain all fluid flows that originate from, and flow towards, the electrolyzer modules. Due to the many modules and their in- and outputs, the flow panel concept offers reduced installation and maintenance complexity. A general design has been proposed, and CNC-machining was determined to be the most suitable manufacturing method. The flow panels should span the width and height of a single module column, due to offering the greatest advantage in the economy of numbers. A detailed material selection analysis was performed, utilizing the ANSYS eduPack software. It was concluded that the flow panels should be manufactured from uPVC. Permeance of hydrogen through the uPVC material was determined to be insignificant, and also not further considered for other uPVC components. A conservative estimate for the pressure drop across the flow panels $\Delta P_{\text{FP}} = 3.7$ mbar, was presented, and the effects of two-phase flow phenomena have been shown to be insignificant.

5.1.4 Gas-liquid Separators

Two simple horizontal gas-liquid separators manufactured from uPVC have been presented. Gravity settling was shown to provide sufficient separator performance. A particle dynamic analysis was conducted, showing that the sizing of the separators depends on their length-to-diameter ratio. An inlet device and mist extractor are suggested to increase separator performance. A vane-type inlet device in the form of a Shell Schoepentoeter, and a wire-mesh pad mist extractor were deemed most suitable. Implementing a wire-mesh pad in the oxygen separator was argued to be unnecessary. A separator diameter of $D_{\text{sep}} = 0.4$ m was proposed, resulting in a total length for the hydrogen and

oxygen separators of $L^{\text{sep}}_{\text{H}_2} = 1.2$ m, and $L^{\text{sep}}_{\text{O}_2} = 0.8$ m, respectively. The hydrogen separator was determined to have a separation efficiency of over 99.8%, and is capable of separating droplets down to 5 μm in diameter. The oxygen separator has been determined to have a separation efficiency of over 99.7%, and is capable of separating droplets down to 25 μm in diameter. A strength analysis utilizing the SolidWorks 2022 software, demonstrates that the uPVC separators are capable of withstanding an overpressure of 500 mbar, in accordance with the Pressure Equipment Directive. The impact of the separators on the heat network of the system has been shown to be insignificant.

5.1.5 System Analysis

The airflow rate required for safe operation was estimated. As a result, the implementation of 12 constant volume fans was recommended, totalling a volumetric airflow rate of 12000 m^3/h. To accompany this, the implementation of variable liquid pumps in the radiator flow loops was suggested, to increase system temperature control. A thermal system analysis was performed, and a temperature control decision tree presented. It was shown that the proposed radiator pair dominates the overall cooling capacity of the section. Upon evaluation, the design of the radiator pair is well suited to counteract the heat generation of the electrolyzer modules. The proposed system was demonstrated to be capable of operating at maximum capacity for a difference in ambient and system temperatures of $\Delta T \geq 15$ °C. Waste heat recovery was argued to be unfeasible.

A hydrodynamic system analysis was performed, wherein both the radiator and electrolyzer flow loops were evaluated. It was concluded that the pressure drop within the system is dominated by that of the radiator flow loops. The highest expected pressure drop in the system was demonstrated to be 250 mbar, which is well below the 500 mbar limit set by the Pressure Equipment Directive.

5.2 Recommendations

During this work, multiple recommendations for future work have been mentioned. These include:

- Determining whether reducing the wire-mesh mist extractor pad thickness to less than 100 mm, results in a significant decrease in separation efficiency. If this is proven to be false, a reduction in both pad and separator size can result in cost reductions.
- Design and sizing of the vortex breakers to be utilized in the separators, as it is crucial that no vortices are formed at the liquid outlets of the separators.
- A CFD analysis of the behaviour of the ventilation airflow within the container, and the potential for hydrogen buildup.
- Evaluating the thermal behaviour of the alkaline electrolyzer modules. More specifically, determining the conductive and convective internal heat transfer coefficient.
- Evaluating the hydrodynamic behaviour of the alkaline electrolyzer modules, and its effects on the flow distribution across the modules in the electrolyzer flow loop.
- Determining the conductive heat transfer coefficient of the flow panels. This allows the thermal behaviour of the flow panels to be modelled.
- Validating the findings of this work experimentally. This includes, but is not limited to: the radiator and separator performance, the heat generation of the electrolyzer modules, the thermal system balance, and hydrodynamic system balance.

Appendix A

Electrolyte Properties

The properties of the KOH electrolyte are determined based on empirical models. The values corresponding to the empirical constants are provided in table A.1. All relations are functions of the electrolyte temperature T [°C], and the KOH mass fraction Y. The density ρ_{EL} [kg/m^3], is based on Gilliam's model [87]:

$$\rho_{\mathrm{EL}} = (K_1 T^2 + K_2 T + K_3)\,\exp(K_4 Y) \tag{A.1}$$

The dynamic viscosity μ_{EL} [Pa·s], is based on Guo's model [93]:

$$\mu_{\mathrm{EL}} = \exp(K_1 + K_1 T + K_3 T^2 + K_4 \frac{\rho_{\mathrm{EL}} \cdot Y}{M_{\mathrm{KOH}}}) \tag{A.2}$$

with M_{KOH} [kg/mol] the molar mass of KOH. Both the specific heat $c_{\mathrm{p}}^{\mathrm{EL}}$ [Jkg^{-1}K^{-1}], and thermal conductivity k_{EL} [Wm^{-1}K^{-1}], are based on the model proposed by Zatsev [94]:

$$c_{\mathrm{p}}^{\mathrm{EL}} = K_1 + K_2\,\ln(T/100) + (K_3 + K_4 Y + 8T)Y \tag{A.3}$$

$$k_{\mathrm{EL}} = (K_1 + K_2 T + K_3 T^2 + K_4 C)(1 - K_4 Y) \tag{A.4}$$

Model used	unit	K_1	K_2	K_3	K_4
Gilliam et al. [95, 87]	ρ_{EL}	$-3.25 \cdot 10^{-3}$	0.111	$1.00171 \cdot 10^3$	0.86
Guo [95, 93]	μ_{EL}	0.43	$-2.51 \cdot 10^{-2}$	10^{-4}	0.13
Zatsev [95, 94]	$c_{\mathrm{p}}^{\mathrm{EL}}$	$4.236 \cdot 10^3$	1.075	$-4.8321 \cdot 10^3$	8
Zatsev [95, 94]	k_{EL}	0.5545	$2.460 \cdot 10^{-3}$	$1.184 \cdot 10^{-5}$	0.128

Table A.1: Values of the empirical constants used to determine properties of KOH, based on the models proposed.

Appendix B

Heat Convection

Convection or convective heat transfer is the transfer of heat from a surface to a moving fluid. There are two main types of convective heat transfer: natural convection and forced convection. Natural convection is a type of heat transfer that occurs due to the buoyancy-induced motion of fluids, caused by differences in temperature and density. Forced convection is a type of heat transfer that occurs when a fluid is forced to flow over a surface by an external means such as a pump, fan, or compressor. The heat flow for convective heat transfer $\dot{Q}$ [W], is given by:

$$\dot{Q} = h_{\mathrm{c}} A \Delta T \tag{B.1}$$

with $\mathrm{h_c}$ [$\mathrm{Wm^{-2}K^{-1}}$] the convective heat transfer coefficient and A [$\mathrm{m^2}$], the area of heat transfer. To calculate the heat flow it is necessary to determine h_{c}, through its relation to the Nusselt number Nu. The Nusselt number describes the ratio of convective to conductive heat transfer:

$$Nu \equiv \frac{h_{\mathrm{c}} L_{\mathrm{c}}}{k} \tag{B.2}$$

where L_{c} [m], denotes the characteristic length of the surface and k [$\mathrm{Wm^{-1}K^{-1}}$], the thermal conductivity of the fluid. Methods to determine the value of the Nusselt number across various surfaces for both natural and forced convection will be covered in this Appendix.

B.1 Natural Convection

In the case of natural convection, Nu is a function of the Prandlt number Pr, and the Rayleigh number Ra. The Prandtl number is a dimensionless material property that describes the ratio of momentum diffusivity to thermal diffusivity:

$$Pr \equiv \frac{\nu}{\alpha} \tag{B.3}$$

with ν [$\mathrm{m^2/s}$] the kinematic viscosity, and α [$\mathrm{m^2/s}$] the thermal diffusivity. The dimensionless Rayleigh number Ra, describes the timescale ratio of diffusive thermal transport to convective thermal transport. Ra is defined as the product of the Prandlt number and the dimensionless Grashof number Gr, which describes the ratio between buoyant and viscous forces.

$$Gr \equiv \frac{\beta \Delta T g L_{\mathrm{c}}^3}{\nu^2} \tag{B.4}$$

$$Ra \equiv PrGr = \frac{\beta \Delta T g L_{\mathrm{c}}^3}{\nu \alpha} \tag{B.5}$$

with β [$\mathrm{K^{-1}}$] the thermal expansion coefficient, g [$\mathrm{m/s^2}$] the gravitational acceleration constant. The flow will be considered laminar below the critical value of $Ra < 10^9$, and turbulent above.

B.1.1 Natural Convection Around a Horizontal Cylinder

The average Nusselt number for natural flow around a cylinder is given a relation provided by the Churchill [96]:

$$\overline{Nu}_{\mathrm{D}} = 0.36 \frac{0.518 Ra_{\mathrm{D}}^{1/4}}{[1 + (0.559/Pr)^{9/19}]^{4/9}} \qquad 10^{-6} < Ra_{\mathrm{D}} < 10^{9} \tag{B.6a}$$

$$= \left\{ 0.06 + 0.387 \left[\frac{Ra_{\mathrm{D}}}{[1 + (0.559/Pr)^{9/16}]^{16/9}} \right]^{1/6} \right\}^2 \qquad 10^{9} \leq Ra_{\mathrm{D}} \tag{B.6b}$$

B.1.2 Natural Convection Along a Vertical Plate

To determine the average Nusselt number of flow on a flat plate; the usage of a Prandtl number function Ψ is suggested by Chruchill and Usagi [97]. They define Ψ as:

$$\Psi \equiv \left[1 + \left(\frac{0.492}{Pr}^{9/16} \right) \right]^{-16/9} \tag{B.7}$$

The average Nusselt number for natural flow around a flat plate of height L is then given by [97, 98]:

$$\overline{Nu}_{\mathrm{L}} = 0.68 + 0.670 (Ra_{\mathrm{L}} \Psi)^{1/4} \qquad Ra_{\mathrm{L}} \leq 10^{9} \tag{B.8a}$$

$$= 0.68 + 0.670 (Ra_{\mathrm{L}} \Psi)^{1/4} (1 + 1.6 \cdot 10^{-8} Ra_{\mathrm{L}} \Phi)^{1/12} \qquad 10^{9} < Ra_{\mathrm{L}} \leq 10^{12} \tag{B.8b}$$

B.2 Forced Convection

In the case of forced convection, Nu is a function of the Prandtl number and the Reynolds number. The dimensionless Reynolds number Re, is defined as the ratio of inertial to viscous forces:

$$Re \equiv \frac{v L_{\mathrm{c}}}{\nu} = \frac{\rho v L_{\mathrm{c}}}{\mu} \tag{B.9}$$

where v [m/s] represents flow velocity and μ [Pa·s] the dynamic viscosity. Similar to the Rayleigh number for natural convection; the flow will be considered laminar below the critical value of $Re < 2500$. However, an in-between region is also considered. This region is referred to as the transitional regime. The flow is considered fully developed turbulent when $Re > 10^4$.

B.2.1 Forced Convection in Tubes and Ducts

The Nusselt number of flow in tubes and ducts can be determined by [62]:

$$Nu_{\mathrm{D}} = 1.86 (Re_{\mathrm{D}} Pr)^{0.33} \left(\frac{\mu}{\mu_{\mathrm{w}}} \right) \qquad Re_{\mathrm{D}} < 2500 \tag{B.10a}$$

$$= \min \left[1.86 (Re_{\mathrm{D}} Pr)^{0.33} \left(\frac{\mu}{\mu_{\mathrm{w}}} \right), C Re_{\mathrm{D}}^{0.8} Pr^{0.33} \left(\frac{\mu}{\mu_{\mathrm{w}}} \right) \right] \qquad 2500 < Re_{\mathrm{D}} < 10^4 \tag{B.10b}$$

$$= C Re_{\mathrm{D}}^{0.8} Pr^{0.33} \left(\frac{\mu}{\mu_{\mathrm{w}}} \right) \qquad 10^4 < Re_{\mathrm{D}} \tag{B.10c}$$

where $C = 0.021$ for gases
$= 0.023$ for nonviscous liquids
$= 0.021$ for viscous liquids

For Reynolds numbers between 2500 and 10^4 the flow is considered to be in the transition region between laminar and fully developed turbulent flow. Within the transition region, Nusselt numbers cannot be predicted with certainty due to instabilities. The minimum value for Nu in the laminar and fully developed turbulent flow region offers a conservative estimate. It is best to avoid the transition region entirely [62]. The minimum flow speed necessary for the flow to be in the fully developed turbulent regime is derived from the definition of Re:

$$v_{\min} = \frac{\mu}{\rho L_{\mathrm{c}}} \cdot 10^4 \tag{B.11}$$

B.2.2 Forced Convection Across a Cylinder

An expression for the average Nusselt number across a cylinder is provided by Mills et al. [60]:

$$\overline{Nu}_{\mathrm{D}} = 0.3 + \frac{0.62 Re_{\mathrm{D}}^{1/2} Pr^{1/3}}{[1 + (0.4/Pr)^{2/3}]^{1/4}} \qquad Re_{\mathrm{D}} < 10^4 \tag{B.12a}$$

$$= 0.3 + \frac{0.62 Re_{\mathrm{D}}^{1/2} Pr^{1/3}}{[1 + (0.4/Pr)^{2/3}]^{1/4}} \left[1 + \left(\frac{Re_{\mathrm{D}}}{2.82 \cdot 10^5}\right)^{1/2}\right] \qquad 2 \cdot 10^4 < Re_{\mathrm{D}} < 4 \cdot 10^5 \tag{B.12b}$$

$$= 0.3 + \frac{0.62 Re_{\mathrm{D}}^{1/2} Pr^{1/3}}{[1 + (0.4/Pr)^{2/3}]^{1/4}} \left[1 + \left(\frac{Re_{\mathrm{D}}}{2.82 \cdot 10^5}\right)^{5/8}\right]^{4/5} \qquad 4 \cdot 10^5 < Re_{\mathrm{D}} < 5 \cdot 10^6 \tag{B.12c}$$

B.2.3 Forced Convection Along a Flat Plate

An expression for the average Nusselt number along a flat plate is provided by Whitaker [99, 60]:

$$\overline{Nu}_{\mathrm{L}} = 0.664 Re_{\mathrm{L}}^{1/2} Pr^{1/3} \qquad Re_{\mathrm{L}} < 5 \cdot 10^5 \tag{B.13a}$$

$$= 0.664 Re_{\mathrm{tr}}^{1/2} Pr^{1/3} + 0.036 Re_{\mathrm{L}}^{0.8} Pr^{0.43} \left[1 - \left(\frac{Re_{\mathrm{tr}}}{Re_{\mathrm{L}}}\right)^{0.8}\right] \qquad 5 \cdot 10^5 < Re_{\mathrm{L}} \tag{B.13b}$$

where $Re_{\mathrm{tr}} = 5 \cdot 10^5$, is the value of the Reynolds number at which the transition of laminar to turbulent flow occurs.

B.3 Mixed Forced and Natural Flows

Mills et al. [60] suggest the usage of a product defined as Gr/Re^2, to determine the dominant mode of convection. Table B.1 shows the criteria to determine the dominant mode of convection. Note that the Prandlt number is a material property. For air at room temperature and atmospheric pressure $Pr_{\mathrm{air}} = 0.71$. In the case forced or natural convection is dominant it should be assumed that the contribution of the other can be neglected. If mixed convection is the dominant phenomenon, both forced and natural convection should be considered. When dealing with mixed convection $\overline{Nu}$ can be estimated through the components of natural convection $\overline{Nu}_{\mathrm{n}}$, and forced convection $\overline{Nu}_{\mathrm{f}}$. In the case of a mixed convection mode over plates, cylinders, and spheres, the following correlations are recommended by Churchill [100]:

$$\overline{Nu} = \overline{Nu}_0 + \sqrt[3]{(\overline{Nu}_f - \overline{Nu}_0)^3 + (\overline{Nu}_n - \overline{Nu}_0)^3} \qquad \text{assisting bouyancy} \tag{B.14a}$$

$$= \overline{Nu}_0 + \sqrt[4]{(\overline{Nu}_f - \overline{Nu}_0)^4 + (\overline{Nu}_n - \overline{Nu}_0)^4} \qquad \text{transverse bouyancy} \tag{B.14b}$$

where $\overline{Nu}_0 = 0$ for plates
$= 0.3$ for cylinders
$= 2$ for spheres

Mod of convection	$Pr \leq 1$	$Pr \to \infty$
Forced convection	$(Gr/Re^2) \ll 1$	$(Gr/Pr^{1/3}Re^2) \ll 1$
Mixed convection	$(Gr/Re^2) \simeq 1$	$(Gr/Pr^{1/3}Re^2) \simeq 1$
Natural convection	$(Gr/Re^2) \gg 1$	$(Gr/Pr^{1/3}Re^2) \gg 1$

Table B.1: External flows mixed convection criteria [60].

B.4 Tube Banks

The procedure in this section is suggested by the work of Mills et al. [60]. A cross-flow over tube banks of n_{row} rows is considered. Figure B.1 shows the mentioned geometric parameters within said an aligned tube bank configuration. The average Nusselt number for the tube bank can be calculated using:

$$\overline{Nu} = \frac{1 + \Phi(n_{\text{row}} - 1)}{n_{\text{row}}} \overline{Nu}^1 \qquad n_{\text{row}} < 10 \tag{B.15a}$$

$$= \Phi \overline{Nu}^1 \qquad n_{\text{row}} \geq 10 \tag{B.15b}$$

with $\overline{Nu}^1$ the average Nusselt number of a standalone tube, and Φ the arrangement factor. For an aligned tube configuration, Φ follows from:

$$\Phi = 1 + \frac{0.7 S_{\text{L}}/S_{\text{T}} - 0.3}{\psi^{1.5}(S_{\text{L}}/S_{\text{T}} + 0.7)^2} \tag{B.16}$$

where the factor ψ is:

$$\psi = 1 - \frac{\pi}{4P_{\text{T}}} \qquad P_{\text{L}} \geq 1 \tag{B.17a}$$

$$= 1 - \frac{\pi}{4P_{\text{T}}P_{\text{L}}} \qquad P_{\text{L}} < 1 \tag{B.17b}$$

and P_{T} and P_{L} are the dimensionless transverse and longitudinal pitch respectively.

$$P_{\text{T}} = S_{\text{T}}/D \tag{B.18a}$$

$$P_{\text{L}} = S_{\text{L}}/D \tag{B.18b}$$

for a heart-to-heart transverse and longitudinal tube distance S_{T}, and S_{P}, respectively.

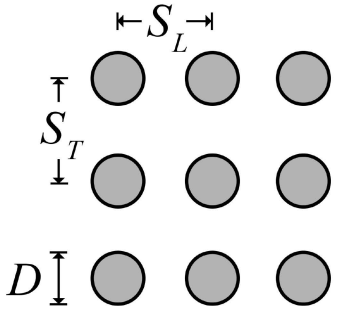

Figure B.1: Reference geometries for an aligned tube bank configuration. D represents the tube diameter, and S_{T} and S_{P} represent the heart-to-heart transverse and longitudinal tube distance.

Appendix C

Hydrodynamics

In this section, it is assumed that the flow is incompressible, Newtonian and mono-phase.

C.1 Hydraulic Diameter

The hydraulic diameter D_h [m], is a concept used in fluid mechanics to characterize the flow properties of a channel or conduit. It represents non-circular and/or non-uniform channels in terms of an equivalent circular pipe. It is used in situations where flow behaviour depends on channel geometry, such as in pressure drop and heat transfer calculation. It is defined as four times the total volume of a channel V, divided by the total surface area A [66]:

$$D_\mathrm{h} \equiv \frac{4V_\mathrm{w}}{A} = \frac{4A_\mathrm{c}L_\mathrm{c}}{A} \tag{C.1}$$

where A_c is the cross section of the channel, and L_c is the characteristic length of the channel. For a channel with a uniform cross-section the expression in Equation (C.1) simplifies to:

$$D_\mathrm{h} = \frac{4A}{l} \tag{C.2}$$

with l the perimeter of the channel. For a circular channel of a uniform cross-section the hydraulic diameter is equal to the diameter of the channel D:

$$D_\mathrm{h} = \frac{4A}{l} = \frac{4\frac{\pi}{4}D^2}{\pi D} = D \tag{C.3}$$

C.2 Pressure Drop

For a fluid flow with velocity v, the general expression for pressure drop in a channel is given by [69]:

$$\Delta P = K\frac{\rho v^2}{2} \tag{C.4}$$

where the loss coefficient K, is a dimensionless property that describes the magnitude of the hydraulic resistance. Various mechanisms that introduce hydraulic losses are discussed in this section. The pressure drop as a result of many of said mechanisms follows the general expression provided in Equation (C.4), with the exception of the gravitational pressure drop.

C.2.1 Gravitational Pressure Drop

The pressure drop due to gravitational effects depends on the difference in altitude Δz of a fluid flow:

$$\Delta P_{\mathrm{g}} = \rho g \Delta z \tag{C.5}$$

C.2.2 Frictional Losses

The pressure drop along a horizontal channel can be expressed as [69, 68]:

$$\Delta P = f_{\mathrm{fr}} \frac{L_{\mathrm{c}}}{D_{\mathrm{H}}} \frac{\rho v^2}{2} \tag{C.6}$$

The friction factor f_{fr}, is a dimensionless quantity that represents the resistance to fluid flow in a channel due to the frictional effects between the fluid and the channel wall. A smooth pipe has a polished inner surface with negligible irregularities. The friction factor in a smooth pipe is solely a function of the Reynolds number. In contrast, a rough pipe has an inner surface containing irregularities resulting in a relatively higher friction factor, and thus pressure drop. The friction factor in a rough pipe is a function of the pipe's roughness ϵ. Table C.1 shows the roughness factors applied in this work. The pipe roughness is a property that should be sourced from literature or pipe manufacturers, as it is dependent on materials, manufacturing methods, and possible finishing processes. In this work, only rough pipes are considered, as they are typically a more economical choice. The expression for f_{fr} depends on the present flow regime. In the transitional flow regime ($2100 < Re < 5000$) there are no reliable correlations available. For laminar flow f_{fr} is solely a function of the Reynolds number, and is described by the Hagen-Poiseuille Equation [70]:

$$f_{\mathrm{fr}} = \frac{16}{Re} \quad Re \leq 2100 \tag{C.7}$$

For turbulent flow in rough pipes the relation Churchill [72, 70] provided is used, as this modified version of the Colebrook formula is explicit in f_{fr}:

$$\frac{1}{\sqrt{f}} = -4\log\left[\frac{0.27\epsilon}{D} + \left(\frac{7}{Re}\right)^{0.9}\right] \quad Re \geq 4000 \tag{C.8}$$

Churchill also provided a single Equation that encompasses all flow regimes, whilst providing reasonable values within the transitional flow regime [70]:

$$f_{\mathrm{fr}} = 2\left[\left(\frac{8}{Re}\right)^{12} + \frac{1}{(A+B)^{3/2}}\right]^{1/12} \tag{C.9}$$

where:

$$A = \left[2.457\ln\left(\frac{1}{(7/Re)^{0.9} + 0.27\epsilon/D}\right)\right]^{16}$$
$$B = \left(\frac{37530}{Re}\right)^{16}$$

Comparing Equation (C.6) to the general pressure drop expression provided in Equation (C.4), allows for the frictional loss coefficient K_{fr} in a horizontal channel to be expressed as a function of f_{fr}:

$$K_{\mathrm{fr}} = f_{\mathrm{fr}} \frac{L_{\mathrm{c}}}{D_{\mathrm{H}}} \tag{C.10}$$

Product type	Drawn tubing	Commercial steel	CNC machined channel
Roughness ϵ / [μm]	1.5 [70, 71]	50 [70, 71]	5 [101]

Table C.1: Roughness for components and materials applied in this work.

C.2.3 Turning Losses

The loss coefficient due to channel turns is denoted by K_{turn}. Miller [69] provides a detailed analytical method to determine K_{turn}. The goal of hydrodynamic analyses is often to determine if the magnitude of hydraulic resistances is within acceptable bounds. It is recommended to utilize the simplified relations provided by Pis'mennyi et al. [61], as they approximate the analytical methods provided by Miller. Whenever the hydrodynamic resistances are determined to be close to, or exceeding acceptable bounds, the work of Miller should be consulted. The method described by Pis'mennyi et al, depends on the turn angle θ, and the ratio between turn radius r_{t} and channel diameter [61]. Table C.2 shows values of K_{turn} for various configurations. Note that the value of K_{turn} takes into account the channel roughness, implying that turns should be excluded from frictional loss calculations [69].

	r_{t}/D					
	1.0	1.5	2.0	3.0	4.0	5.0
$\theta = 90°$	0.41	0.34	0.30	0.24	0.22	0.20
$\theta = 180°$	0.60	0.48	0.40	0.32	0.28	0.26

Table C.2: Simplified method to determine K_{turn}, provided by Pis'mennyi et al. [61]. Value of K_{turn} determined through the turn angle θ, and the turn-to-channel diameter ratio r_{t}/D.

C.2.4 Expansion and Contraction Losses

Losses due to abrupt contraction can be considered negligible, as converting static pressure to velocity pressure is stable. The loss coefficient due to abrupt expansion K_{exp} is given by [69]:

$$K_{\text{exp}} = \left[1 - \left(\frac{A_{\text{in}}}{A_{\text{out}}}\right)\right]^2 \tag{C.11}$$

C.2.5 Manifolds

Manifolds are utilized to combine and divide flows in the system. Figure C.1 shows an illustration of both collecting (a), and dividing (b) manifolds. The ratio of the total cross-sectional area of the manifold branches to the cross-sectional area of the manifold should be less than unity, and preferably less than 0.5. This criterion ensures that the branch flow distribution is optimal [69].

$$\frac{\text{total cross-sectional area of the manifold branches}}{\text{cross-sectional area of the manifold}} < 1 \tag{C.12}$$

It is advantageous to minimize pressure drop within the manifold, as it offers no advantages. This is in contrast with, for example, HEX design where pressure drop and heat transfer are both a function of flow velocity. In this work, manifolds exist for the inlet and outlet of both the radiator and modules. Since flow rates and branch dimensions are dominated by the design of their respective component, other means should be explored to reduce pressure drop within the manifolds. In accordance with Equation (C.4), pressure drop can be reduced by reducing the loss coefficient K, and/or reducing the flow speed v within the manifold. Within the constraints of this work, three options for reducing pressure drop within manifolds are presented.

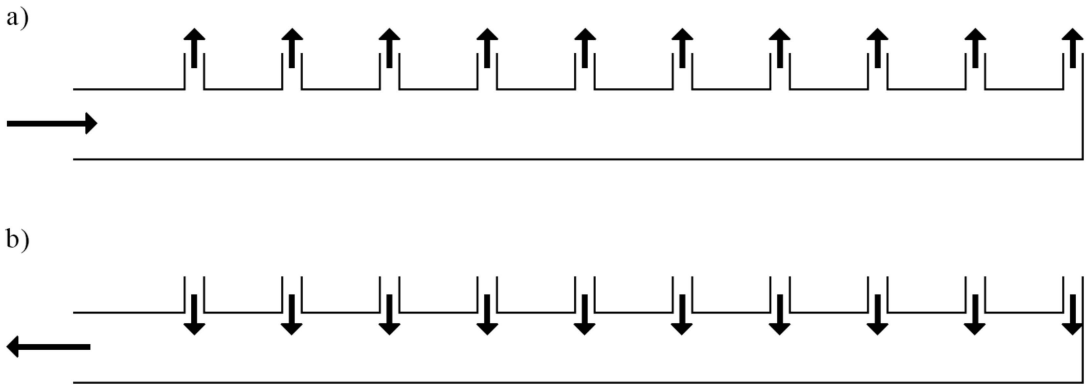

Figure C.1: Schematic representation of dividing (a), and combining (b) manifolds. Flow enters in manifold channel to be distributed across, or collected from the manifold branches.

- Increasing the hydraulic diameter of the divider and collector channels, reducing v.
- Minimizing the angle between the flow paths of the divider and collector to and from the branches; reducing K [69].
- Rounding the corners to and from the manifolds branches; reducing K [69].

The loss coefficient of the manifold is approximately equal to that of isolated combining and dividing junctions if:

- the branch flow rate is $\leq 10\%$ of the total flow rate, and the manifold branches are more than 4 branch diameters apart; or
- the manifold branches are more than 3 manifold diameters apart [69].

Figure C.2a illustrates the flow paths within a combining T-junction, and provides a means of determining values for K, based on the internal flow ratios. Figure C.2b illustrates the flow paths within a dividing T-junction, and provides a means of determining values for K, based on the internal flow ratios.

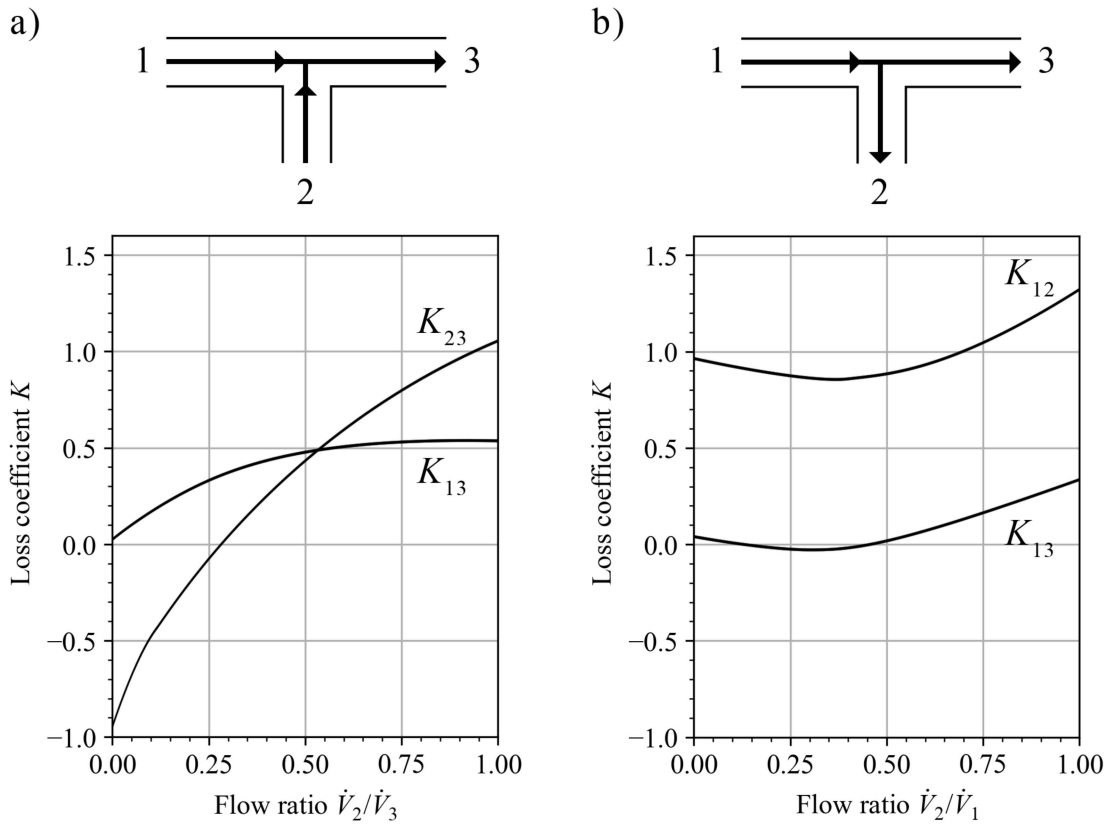

Figure C.2: Flow in combining (a), and dividing (b) T-junctions. Loss coefficients are determined based on values of the volumetric flow ratio; defined as the ratio of the volumetric flow rate of the branch to that of the manifold. K_{13} represents the loss coefficient of the manifold throughflow, and K_{12} and K_{23} represent the loss coeffients of the branch flows. Recreated from [69].

Appendix D

Plastics

Plastics are a category of synthetic materials made from polymers. Polymers are large molecules composed of repeating subunits called monomers. The manufacturing of polymers takes place through a process called polymerization, where monomers chemically bond together to create long chains. Thermoset plastics are plastics for which their polymeric chains form bonds with others during polymerization, also referred to as cross-links. The polymeric cross-links result in a three-dimensional network of polymeric chains that are irreversible, meaning that they cannot be remelted or recycled. When compared to thermoplastics, thermoset polymers offer greater strength retention at increased temperatures. Thermoplastics are polymers that do not form internal cross-links. As a result, thermoplastics can be melted and reshaped multiple times, whilst retaining quality. Thermoplastics their main advantage lies in their manufacturability and recyclability [102]. Plastics, both thermoplastics and thermosets can be generally categorized in two categories:

- Commodity plastics are widely produced and used due to their low cost, ease of processing, and versatility. They are typically used in applications where specific mechanical, thermal, or chemical properties are not critical. Common examples of commodity plastics include polyethylene (PE), polypropylene (PP), polyvinyl chloride (PVC), polystyrene (PS), and polyethylene terephthalate (PET).
- Engineering plastics offer enhanced mechanical, thermal, and chemical properties compared to commodity plastics. They are typically preferred in demanding applications. Engineering plastics can offer high strength, stiffness, impact resistance, heat resistance, and chemical resistance. Common examples of engineering plastics include polycarbonate (PC), acrylonitrile butadiene styrene (ABS), polyamide (PA/Nylon), polyoxymethylene (POM), and polyphenylene oxide (PPO).

D.1 Manufacturing Methods

Many processes are available for the manufacturing of polymer components. In this section, a number of manufacturing processes applicable to components in this work are described. Emphasis is placed on manufacturing processes applicable to the manufacturing of large and complex components, as the flow panels are the only polymer component that is not manufacturable from off-the-shelf components.

D.1.1 Extrusion

Extrusion is a manufacturing process used to create continuous lengths of uniform cross-sectional profiles from various materials. For polymer extrusion, the process involves feeding a solid polymer material, typically in the form of granules or pellets, into a heated barrel of an extruder. The

material is melted and conveyed by a rotating screw. The molten polymer is forced through a die, which determines the shape of the extruded product. As the polymer exits the die, it undergoes cooling and solidification. Extrusion offers versatility in producing a wide range of products, including pipes, tubes, and sheets [103, 104].

D.1.2 Polymer Resin Casting

Polymer resin casting is a manufacturing process used to create solid plastic components by pouring liquid resin into a mould, and allowing it to cure. The resin is initially mixed with additives, such as fillers, pigments, or reinforcing agents. The liquid resin is then poured into a mould, forming its shape [103].

D.1.3 Thermoforming

Thermoforming is a manufacturing process used to shape thermoplastic sheets into various three-dimensional forms. The process involves heating a thermoplastic sheet to its softening point, typically through the use of heat lamps, infrared heaters, or a heated mould. Once the sheet reaches the desired temperature, it is placed over a mould and pressure is applied to force the material to form to shape of the mould [103, 104].

D.1.4 Injection Moulding

Injection moulding is a versatile manufacturing technique where, typically, molten plastic is shaped by injecting it under high pressure into a mould. The material cools and solidifies within the mould, taking on its desired shape [103].

D.1.5 Reaction Injection moulding

Reaction Injection moulding (RIM) is a low-pressure ($0.2 - 1.0$ MPa) manufacturing process that involves the injection of two liquid components, typically a polyol and an isocyanate, into a mould cavity [23]. The mixture undergoes polymerization inside the mould. Similar to polymer resin casting, the relatively low viscosity of the injection components allows for the production of complexly shaped components [23, 104].

D.1.6 CNC-Machining

CNC (Computer Numerical Control) is a manufacturing process that utilizes computerized control systems to automate the operation of machine tools. CNC-machines are capable of precise and complex movements in multiple axes, allowing for the accurate shaping, cutting, and milling of various materials. [23]

Bibliography

[1] Wallace S. Broecker. "Climatic Change: Are We on the Brink of a Pronounced Global Warming?" In: *Science* 189.4201 (1975), pp. 460–463.

[2] Lata Tripathi et al. "Renewable energy: An overview on its contribution in current energy scenario of India". In: *Renewable and Sustainable Energy Reviews* 60 (2016), pp. 226–233.

[3] International Energy Agency. *Net Zero by 2050 - A Roadmap for the Global Energy Sector*. 2021. (accessed: 05.01.2023).

[4] United Nations Framework Convention on Climate Change. *The Paris Agreement*. 2016. URL: `https://unfccc.int/process-and-meetings/the-paris-agreement/the-paris-agreement`. (accessed: 05.01.2023).

[5] REN21. *Renewables 2022 global status report*. 2022. URL: `https://www.ren21.net/wp-content/uploads/2019/05/GSR2022_Full_Report.pdf`. (accessed: 11.11.2022).

[6] Bernard Lee and David E. Gushee. "Electricity storage : the Achilles' heel of renewable energy". In: *Chemical Engineering Progress* 104 (2008).

[7] International Energy Agency. *Global Hydrogen Review 2021*. 2021. (accessed: 05.01.2023).

[8] Patrick Moriarty and Damon Honnery. "Can renewable energy power the future?" In: *Energy Policy* 93 (2016), pp. 3–7.

[9] Barbara Widera. "Renewable hydrogen implementations for combined energy storage, transportation and stationary applications". In: *Thermal Science and Engineering Progress* 16 (2020), p. 100460.

[10] Alexander Buttler and Hartmut Spliethoff. "Current status of water electrolysis for energy storage, grid balancing and sector coupling via power-to-gas and power-to-liquids: A review". In: *Renewable and Sustainable Energy Reviews* 82 (2018), pp. 2440–2454.

[11] Renxing Huang, Lixia Kang, and Yongzhong Liu. "Renewable synthetic methanol system design based on modular production lines". In: *Renewable and Sustainable Energy Reviews* 161 (2022), p. 112379.

[12] Çiçek Bezir Nalan, Öztürk Murat, and Özek Nuri. "Renewable energy market conditions and barriers in Turkey". In: *Renewable and Sustainable Energy Reviews* 13.6 (2009), pp. 1428–1436.

[13] Cory Budischak et al. "Cost-minimized combinations of wind power, solar power and electrochemical storage, powering the grid up to 99.9% of the time". In: *Journal of Power Sources* 225 (2013), pp. 60–74.

[14] Alberto Boretti. "Hydrogen internal combustion engines to 2030". In: *International Journal of Hydrogen Energy* 45.43 (2020), pp. 23692–23703.

[15] Kristin Seyboth et al. "Recognising the potential for renewable energy heating and cooling". In: *Energy Policy* 36.7 (2008), pp. 2460–2463.

[16] Peng Yen Liew et al. “Total Site Heat Integration planning and design for industrial, urban and renewable systems”. In: *Renewable and Sustainable Energy Reviews* 68 (2017), pp. 964–985.

[17] Wolf-Peter Schill and Alexander Zerrahn. “Flexible electricity use for heating in markets with renewable energy”. In: *Applied Energy* 266 (2020), p. 114571.

[18] Henok Ayele Behabtu et al. “A Review of Energy Storage Technologies’ Application Potentials in Renewable Energy Sources Grid Integration”. In: *Sustainability* 12.24 (2020).

[19] Robert McConnell Krishnan Rajeshwar and Stuart Licht. *Solar Hydrogen Generation Toward a Renewable Energy Future*. Springer, 2008.

[20] XINTC. *XINTC*.

[21] Marianne Gilbert. “Chapter 1 - Plastics Materials: Introduction and Historical Development”. In: *Brydson’s Plastics Materials (Eighth Edition)*. Ed. by Marianne Gilbert. Eighth Edition. Butterworth-Heinemann, 2017, pp. 1–18.

[22] D.G. Baird and D.I. Collias. *Polymer Processing: Principles and Design*. Wiley, 2014.

[23] Ansys. *Granta EduPack 2022 R1*. Software. Version 22.1.2. Version 2022. 2022.

[24] *Directive 2014/68/EU of the European Parliament and of the Council of 15 May 2014 on the harmonisation of the laws of the Member States relating to the making available on the market of pressure equipment (recast) Text with EEA relevance*.

[25] Alfredo Ursua, Luis M. Gandia, and Pablo Sanchis. “Hydrogen Production From Water Electrolysis: Current Status and Future Trends”. In: *Proceedings of the IEEE* 100.2 (2012), pp. 410–426.

[26] Maximilian Schalenbach et al. “Acidic or Alkaline? Towards a New Perspective on the Efficiency of Water Electrolysis”. In: *Journal of The Electrochemical Society* 163.11 (Aug. 2016), F3197.

[27] Ramchandra Bhandari, Clemens A. Trudewind, and Petra Zapp. “Life cycle assessment of hydrogen production via electrolysis – a review”. In: *Journal of Cleaner Production* 85 (2014). Special Volume: Making Progress Towards More Sustainable Societies through Lean and Green Initiatives, pp. 151–163.

[28] Nel ASA. *Water electrolysers / hydrogen generators*. URL: `https://nelhydrogen.com/water-electrolysers-hydrogen-generators/`.

[29] Silvestros Oikonomidis. “Modeling gas crossover in alkaline water electrolysers”. 2022.

[30] Tom Smolinka, Martin Günther, and Jürgen Garche. “Stand und Entwicklungspotenzial der Wasserelektrolyse zur Herstellung von Wasserstoff aus regenerativen Energien”. In: *Fraunhofer ISE* (2011).

[31] Marcelo Carmo et al. “A comprehensive review on PEM water electrolysis”. In: *International Journal of Hydrogen Energy* 38.12 (2013), pp. 4901–4934.

[32] Johanna Ivy. *Summary of electrolytic hydrogen production: milestone completion report*. Tech. rep. National Renewable Energy Lab., Golden, CO (US), 2004.

[33] Frano Barbir. “PEM electrolysis for production of hydrogen from renewable energy sources”. In: *Solar energy* 78.5 (2005), pp. 661–669.

[34] Annabelle Brisse, Josef Schefold, and Mohsine Zahid. “High temperature water electrolysis in solid oxide cells”. In: *International Journal of Hydrogen Energy* 33.20 (2008), pp. 5375–5382.

[35] J Sigurvinsson et al. “Can high temperature steam electrolysis function with geothermal heat?” In: *International Journal of Hydrogen Energy* 32.9 (2007), pp. 1174–1182.

[36] Jun-Yong Park, Deok-Young Sohn, and Yun-Ho Choi. "A numerical study on the flow characteristics and flow uniformity of vanadium redox flow battery flow frame". In: *Applied Sciences* 10.23 (2020), p. 8427.

[37] Ao Tang, Jie Bao, and Maria Skyllas-Kazacos. "Studies on pressure losses and flow rate optimization in vanadium redox flow battery". In: *Journal of Power Sources* 248 (2014), pp. 154–162.

[38] Martin Harrer and Herbert Bucsich. *Frame of a Cell of a Redox Flow Battery*. Aug. 2014.

[39] Carliss Y. Baldwin and Kim B. Clark. *Design Rules: The Power of Modularity*. The MIT Press, Mar. 2000.

[40] Ali Kharrazi. *Resilience*. Ed. by Brian Fath. Second Edition. Oxford: Elsevier, 2019, pp. 414–418.

[41] Mark Levin. *Modular System Design and Evaluation*. Nov. 2014.

[42] Michael Baldea et al. "Modular manufacturing processes: Status, challenges, and opportunities". In: *AIChE Journal* 63.10 (2017), pp. 4262–4272.

[43] Vitor Gazzaneo et al. "A techno-economic analysis framework for intensified modular systems". In: *Journal of Advanced Manufacturing and Processing* 4.3 (2022), e10115.

[44] S. Lier; M. Grünewald. "Net Present Value Analysis of Modular Chemical Production Plants". In: *Chemical Engineering and Technology 2011-mar 09 vol. 34 iss. 5* 34 (5 Mar. 2011).

[45] Atharv Bhosekar and Marianthi Ierapetritou. "Modular Design Optimization using Machine Learning-based Flexibility Analysis". In: *Journal of Process Control* 90 (2020), pp. 18–34.

[46] Kyle Oyama et al. "Linking Modularity to System Assembly: Initial Findings and Implications". In: *Systems Research Forum* 04 (Mar. 2010).

[47] Peter D. Gentile. "Theory of Modularity, a Hypothesis". In: *Procedia Computer Science* 20 (2013). Complex Adaptive Systems, pp. 203–209.

[48] Victor Nian and Sheng Zhong. "Economic feasibility of flexible energy productions by small modular reactors from the perspective of integrated planning". In: *Progress in Nuclear Energy* 118 (2020), p. 103106.

[49] H. Hidayatullah, S. Susyadi, and M. Hadid Subki. "Design and technology development for small modular reactors – Safety expectations, prospects and impediments of their deployment". In: *Progress in Nuclear Energy* 79 (2015), pp. 127–135.

[50] B. Mignacca and G. Locatelli. "Economics and finance of Small Modular Reactors: A systematic review and research agenda". In: *Renewable and Sustainable Energy Reviews* 118 (2020), p. 109519.

[51] D. Michaelson and J. Jiang. "Review of integration of small modular reactors in renewable energy microgrids". In: *Renewable and Sustainable Energy Reviews* 152 (2021), p. 111638.

[52] Joel Martinez-Frias, Ai-Quoc Pham, and Salvador M. Aceves. "A natural gas-assisted steam electrolyzer for high-efficiency production of hydrogen". In: *International Journal of Hydrogen Energy* 28.5 (2003), pp. 483–490.

[53] Foster Lubbe et al. "Golden hydrogen". In: *Current Opinion in Green and Sustainable Chemistry* 39 (2023), p. 100732.

[54] Sunfire. *SUNFIRE-HYLINK*. Brochure. 2018.

[55] Sunfire. *SUNFIRE-HYLINK*. Brochure. 2022.

[56] Sunfire. *SUNFIRE-HYLINK*. Brochure. 2022.

[57] Enapter. *AEM Electrolyser EL 4.0*. URL: `https://handbook.enapter.com/electrolyser/el40/downloads/Enapter_Datasheet_EL40_EN.pdf`.

[58] Kristian Mera. “Thermal modeling of an alkaline electrolyser under variable load”. 2022.

[59] Silvestros Oikonomidis et al. “Transient modelling of a multi-cell alkaline electrolyzer for gas crossover and safe system operation”. In: *International Journal of Hydrogen Energy* (2023).

[60] A.F. Mills and Carlos F.M. Coimbra. *Basic Heat and Mass Transfer*. Temporal Publishing, 2015.

[61] Ignacio Carvajal et al. *Handbook for Transversely Finned Tube Heat Exchanger Design*. May 2016.

[62] Ray K. Towler Gavin; Sinnott. *Chemical Engineering Design - Principles, Practice and Economics of Plant and Process Design*. 2nd Edition. Elsevier, 2013.

[63] Chi-Chuan Wang and Kuan-Yu Chi. “Heat transfer and friction characteristics of plain fin-and-tube heat exchangers, part I: New experimental data”. In: *International Journal of Heat and Mass Transfer* 43 (Aug. 2000), pp. 2681–2691.

[64] Chi-Chuan Wang, Kuan-Yu Chi, and Chun-Jung Chang. “Heat transfer and friction characteristics of plain fin-and-tube heat exchangers, part II: Correlation”. In: *International Journal of Heat and Mass Transfer* 43.15 (2000), pp. 2693–2700.

[65] John H Lienhard IV and John H Lienhard V. *A HEAT TRANSFER TEXT BOOK THIRD EDITION*. 2006.

[66] W.M. Kays and A.L. London. *Compact heat exchangers*. Krieger Pub. Co., 1984.

[67] Ramesh K. Shah and Dušan P. Sekulić. John Wiley & Sons, 2003.

[68] David R Dowling Pijush K. Kundu Ira M. Cohen. *Fluid Mechanics*. 6th ed. Academic Press, 2015.

[69] D.S. Miller. *Internal Flow Systems*. BHRA Fluid Engineering series. BHRA (Information Services), 1990.

[70] Robert Perry Don Green. *Perry’s Chemical Engineers’ Handbook*. 8th ed. Chemical Engineers Handbook. McGraw-Hill Professional, 2007.

[71] Gas Processors Association. *Gas Processors Suppliers Association - GPSA Engineering Data Book*. 12th Ed.

[72] Stuart W. Churchill. “Friction factor equations spans all fluid-flow regimes”. In: *Chemical Engineering Journal* 84 (1977), pp. 91–92.

[73] J.A. Brydson. *32 - Material Selection*. Ed. by J.A. Brydson. Seventh Edition. Oxford: Butterworth-Heinemann, 1999, pp. 890–897.

[74] Roger Rothon and Christopher DeArmitt. “Chapter 8 - Fillers (Including Fiber Reinforcements)”. In: *Brydson’s Plastics Materials (Eighth Edition)*. Ed. by Marianne Gilbert. Eighth Edition. Butterworth-Heinemann, 2017, pp. 169–204.

[75] Marianne Gilbert. *Chapter 4 - Relation of Structure to Thermal and Mechanical Properties*. Ed. by Marianne Gilbert. Eighth Edition. Butterworth-Heinemann, 2017, pp. 59–73.

[76] J. Brandrup, E.H. Immergut, and E.A. Grulke. *Polymer Handbook*. Wiley, 1999.

[77] John D. Schwarzkopf Efstathios E. Michaelides Clayton T. Crowe. *Multiphase Flow Handbook*. 2nd ed. MECHANICAL and AEROSPACE ENGINEERING. CRC Press, 2017.

[78] WH McAdams, WK Woods, and LC Heroman Jr. “Vaporization inside horizontal tubes—II benzene-oil mixtures”. In: *Transactions of the American Society of Mechanical Engineers* 64.3 (1942), pp. 193–199.

[79] J M Campbell. *Gas conditioning and processing. Vol. 2*. 1979.

[80] R. Turton and O. Levenspiel. “A short note on the drag correlation for spheres”. In: *Powder Technology* 47.1 (1986), pp. 83–86.

[81] D. G. KARAMANEV. “EQUATIONS FOR CALCULATION OF THE TERMINAL VELOCITY AND DRAG COEFFICIENT OF SOLID SPHERES AND GAS BUBBLES”. In: *Chemical Engineering Communications 1996-may vol. 147 iss. 1* 147 (1 May 1996).

[82] Inc. Wolfram Research. *WolframAlpha: computational intelligence*.

[83] M. Stewart and K. Arnold. *Gas-Liquid And Liquid-Liquid Separators*. Catalogued Knovel cf. Elsevier Science, 2008.

[84] Shell USA Inc. and Hugo Polderman. “Gas/liquid separator”. Patent US20050060970A1. 2005.

[85] P Fabian et al. “Demystifying the selection of mist eliminators”. In: *Chemical Engineering (New York); (United States)* (1993).

[86] Utami Ledyana, Apriliana Dwijayanti, and Karl Kolmetz. “DEMISTER PAD SELECTION, SIZING AND TROUBLESHOOTING, Kolmetz Handbook of Process Equipment Design”. In: (Nov. 2020).

[87] R.J. Gilliam et al. “A review of specific conductivities of potassium hydroxide solutions for various concentrations and temperatures”. In: *International Journal of Hydrogen Energy* 32.3 (2007). Fuel Cells, pp. 359–364.

[88] *SolidWorks 2022*. Computer software. Dassault Systèmes SolidWorks Corporation. 2022.

[89] R.C. Hibbeler. *Mechanics of Materials, SI Edition*. Pearson Education, 2017.

[90] F. Tabkhi et al. “A mathematical framework for modelling and evaluating natural gas pipeline networks under hydrogen injection”. In: *International Journal of Hydrogen Energy* 33.21 (2008), pp. 6222–6231.

[91] D.M. van de Bor, C.A. Infante Ferreira, and Anton A. Kiss. “Low grade waste heat recovery using heat pumps and power cycles”. In: *Energy* 89 (2015), pp. 864–873.

[92] Dongxiang Wang et al. “Efficiency and optimal performance evaluation of organic Rankine cycle for low grade waste heat power generation”. In: *Energy* 50 (2013), pp. 343–352.

[93] Ya-jie GUO et al. “Density and viscosity of aqueous solution of K2CrO4/KOH mixed electrolytes”. In: *Transactions of Nonferrous Metals Society of China* 20 (2010), s32–s36.

[94] Ivan Dmitrievich Zatsev and G. G. Aseev. *Properties of Aqueous Solutions of Electrolytes*. 1992.

[95] Damien Le Bideau et al. “Review of necessary thermophysical properties and their sensivities with temperature and electrolyte mass fractions for alkaline water electrolysis multiphysics modelling”. In: *International Journal of Hydrogen Energy* 44.10 (2019), pp. 4553–4569.

[96] Stuart W. Churchill and Humbert H.S. Chu. “Correlating equations for laminar and turbulent free convection from a horizontal cylinder”. In: *International Journal of Heat and Mass Transfer* 18.9 (1975), pp. 1049–1053.

[97] S. W. Churchill and R. Usagi. “A general expression for the correlation of rates of transfer and other phenomena”. In: *AIChE Journal* 18.6 (1972), pp. 1121–1128.

[98] Stuart W. Churchill and Humbert H.S. Chu. “Correlating equations for laminar and turbulent free convection from a vertical plate”. In: *International Journal of Heat and Mass Transfer* 18.11 (1975), pp. 1323–1329.

[99] Stephen Whitaker. “Forced convection heat transfer correlations for flow in pipes, past flat plates, single cylinders, single spheres, and for flow in packed beds and tube bundles”. In: *AIChE Journal* 18 (Mar. 1972), pp. 361–371.

[100] Stuart W. Churchill. *Combined Free and Forced Convection Around Immersed Bodies*. New York, Apr. 2015.

[101] Michael F. Ashby, Hugh Shercliff, and David Cebon. *Materials: Engineering, Science, Processing and Design*. 3rd. Oxford, UK: Butterworth-Heinemann, 2019.

[102] Steve Edmondson and Marianne Gilbert. "Chapter 2 - The Chemical Nature of Plastics Polymerization". In: *Brydson's Plastics Materials (Eighth Edition)*. Ed. by Marianne Gilbert. Eighth Edition. Butterworth-Heinemann, 2017, pp. 19–37.

[103] Harold Belofsky. *Plastics Product Design and Process Engineering*. Spe Books. Hanser Gardner Publications, 1995.

[104] P. F. Mastro. *Process Overviews, Advantages and Constraints*. John Wiley and Sons, Ltd, 2016. Chap. 4, pp. 65–92.